

ผลของการเจือแมงกานีสและคอปเปอร์ต่อสมบัติทางไฟฟ้าและทางแม่เหล็ก
ของเซรามิกชนิด $0.75\text{BiFeO}_3-0.25\text{BaTiO}_3$

นางสาวสุจิตรา จันดาร์ักษ์

วิทยานิพนธ์นี้เป็นส่วนหนึ่งของการศึกษาตามหลักสูตรปริญญาวิศวกรรมศาสตรดุษฎีบัณฑิต
สาขาวิชาวิศวกรรมเซรามิก
มหาวิทยาลัยเทคโนโลยีสุรนารี
ปีการศึกษา 2555

**EFFECTS OF MANGANESE AND COPPER DOPING ON
ELECTRICAL AND MAGNETIC PROPERTIES OF
0.75BiFeO₃-0.25BaTiO₃ CERAMICS**

Sujittra Chandarak

**A Thesis Submitted in Partial Fulfillment of the Requirements for the
Degree of Doctor of Philosophy of Engineering in Ceramic Engineering**

Suranaree University of Technology

Academic Year 2012

**EFFECTS OF MANGANESE AND COPPER DOPING ON
ELECTRICAL AND MAGNETIC PROPERTIES OF
0.75BiFeO₃-0.25BaTiO₃ CERAMICS**

Suranaree University of Technology has approved this thesis submitted in partial fulfillment of the requirements for the Degree of Doctor of Philosophy.

Thesis Examining Committee

(Asst. Prof. Dr. Sukasem Kangwantrakool)

Chairperson

(Asst. Prof. Dr. Sutham Srilomsak)

Member (Thesis Advisor)

(Asst. Prof. Dr. Rattikorn Yimnirun)

Member

(Dr. Saroj Rujirawat)

Member

(Assoc. Prof. Dr. Sutin Kuharuangrong)

Member

(Assoc. Prof. Dr. Charussri Lorprayoon)

Member

(Prof. Dr. Sukit Limpijumnong)

Vice Rector for Academic Affairs

(Assoc. Prof. Flt. Lt. Dr. Kontom Chamniprasart)

Dean of Institute of Engineering

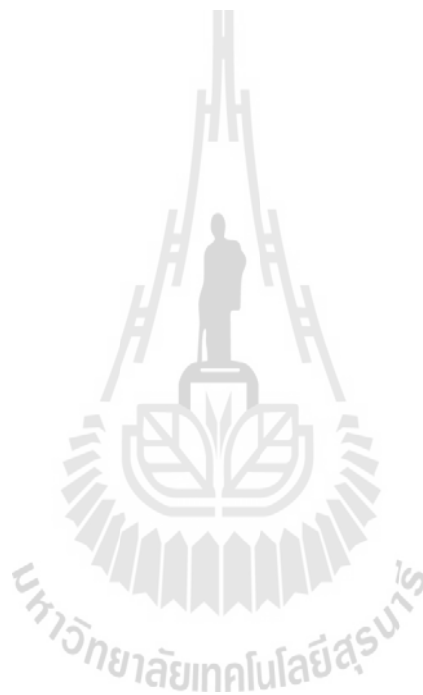
สุจิตรา จันดารักษ์ : ผลของการเจือเมงกานีสและคอปเปอร์ต่อสมบัติทางไฟฟ้าและทางแม่เหล็กของเซรามิกชนิด $0.75\text{BiFeO}_3\text{-}0.25\text{BaTiO}_3$ (EFFECTS OF MANGANES AND COPPER DOPING ON ELECTRICAL AND MAGNETIC PROPERTIES OF $0.75\text{BiFeO}_3\text{-}0.25\text{BaTiO}_3$ CERAMICS) อาจารย์ที่ปรึกษา : ผู้ช่วยศาสตราจารย์ ดร. สุธรรม ศรีหล่มสัก, 155 หน้า.

วิทยานิพนธ์ฉบับนี้ได้ทำการศึกษาถึงผลของการเจือคอปเปอร์และเมงกานีสต่อสมบัติทางไฟฟ้าและทางแม่เหล็กของเซรามิกชนิด $0.75\text{BiFeO}_3\text{-}0.25\text{BaTiO}_3$ โดยการเจือคอปเปอร์และเมงกานีสในงานวิจัยนี้ เตรียมโดยการคำนวณให้สัดส่วนองค์ประกอบของคอปเปอร์และเมงกานีสเข้าไปแทนที่ในตำแหน่งของอะตอมเหล็กและไทเทเนียมในโครงสร้างของบิสมาทเฟอร์ไรต์-แบเรียมไทเทเนต โดยมีปริมาณของสารที่เจืออยู่ในช่วง 1-5 เปอร์เซ็นต์โดยโมล ในการเตรียมสารทุกสัดส่วนองค์ประกอบถูกเตรียมโดยใช้วิธีการผสมออกไซด์แบบดั้งเดิมด้วยวิธีการสับบด จากนั้นทำให้อยู่ในรูปแบบของเซรามิกโดยผ่านกระบวนการทางเซรามิกด้วยการแคลไซน์และการเผาผนึกจากการตรวจสอบลักษณะการเกิดเฟสด้วยเทคนิคการเลี้ยวเบนของรังสีเอกซ์ พบว่า สามารถเตรียมเซรามิกที่มีความบริสุทธิ์ และมีความหนาแน่นสัมพัทธ์อยู่ในช่วง 90-98 เปอร์เซ็นต์ จากการวัดสมบัติทางไดอิเล็กทริกด้วยเครื่อง LCR meter พบว่า การเจือด้วยคอปเปอร์และเมงกานีสนั้นสามารถลดการเปลี่ยนแปลงสมบัติทางไดอิเล็กทริกตามความถี่ของเซรามิกบิสมาทเฟอร์ไรต์-แบเรียมไทเทเนตได้ โดยค่าคงที่ทางไดอิเล็กทริกอยู่ในช่วง 320-480 ส่วนค่าความสูญเสียทางไดอิเล็กทริกอยู่ในช่วง 0.05-0.15 สามารถพบได้ในเซรามิกที่เจือด้วยเมงกานีส การตรวจสอบสมบัติเฟอร์โรอิเล็กทริกด้วยวงจรวัด Sawyer-Tower พบว่า วงวนฮิสเทอรีซิสสามารถวัดได้ในเฉพาะเซรามิกที่เจือด้วยเมงกานีสที่สัดส่วนองค์ประกอบ 2 เปอร์เซ็นต์โดยโมล โดยค่าโพลาริเซชันคงค้างอยู่ในช่วง 7.65-7.72 ไมโครคูลอมบ์ต่อตารางเซนติเมตร เมื่อทำการวัดสมบัติแม่เหล็กด้วยเครื่อง Vibrating Sample Magnetometer พบว่า ความเป็นเฟอร์โรแมกเนติกที่มีค่าแม่เหล็กคงค้างมากกว่า 0.15 หน่วยอิเล็กโตแมกเนติกต่อกรัม สามารถพบได้ในทุกสัดส่วนองค์ประกอบที่มีการเจือด้วยคอปเปอร์ ซึ่งที่สัดส่วนองค์ประกอบ 4 เปอร์เซ็นต์โดยโมลของคอปเปอร์ มีค่าแม่เหล็กคงค้างที่สูงที่สุด โดยมีค่าเท่ากับ 0.4 หน่วยอิเล็กโตแมกเนติกต่อกรัม

สมบัติแมกเนโตอิเล็กทริกซึ่งบ่งบอกถึงศักยภาพของวัสดุที่สามารถนำไปประยุกต์ใช้งานในหัวอ่านในเทคโนโลยีฮาร์ดดิสก์ไครฟ์ถูกทำการศึกษาในงานวิจัยนี้ ซึ่งจากผลการตรวจสอบพบว่า เซรามิกบิสมาทเฟอร์ไรต์-แบเรียมไทเทเนตที่มีการเจือด้วยเมงกานีสในปริมาณ 2 เปอร์เซ็นต์โดยโมลและผ่านการเผาผนึกที่อุณหภูมิ 1025 องศาเซลเซียส มีค่าสัมประสิทธิ์แมกเนโตอิเล็กทริกที่ดี

ที่สุด และถูกพิจารณาให้เป็นสัดส่วนองค์ประกอบที่เหมาะสมในการนำไปพัฒนาต่อยอดสำหรับการพัฒนาไปเป็นหัวอ่านในเทคโนโลยีฮาร์ดดิสก์ไดรฟ์ในอนาคต

ท้ายที่สุดการหาเลขออกซิเดชันและตำแหน่งของคอปเปอร์และแมงกานีสในโครงสร้างบิสมีทเฟอร์ไรต์-แบเรียมไทเทเนต ด้วยเทคนิคการดูดกลืนรังสีเอกซ์ พบว่า เลขออกซิเดชันของคอปเปอร์และแมงกานีสมีค่าดังนี้ เลขออกซิเดชันของคอปเปอร์เป็น 3 หรือ มีการรวมกันของคอปเปอร์ที่มีเลขออกซิเดชันเท่ากับ 3 และปริมาณเพียงเล็กน้อยของคอปเปอร์ที่มีเลขออกซิเดชันเท่ากับ 2 และแมงกานีสมีเลขออกซิเดชันเท่ากับ 4 และปริมาณเพียงเล็กน้อยของแมงกานีสที่มีเลขออกซิเดชันเท่ากับ 3



สาขาวิชาวิศวกรรมเซรามิก

ปีการศึกษา 2555

ลายมือชื่อนักศึกษา_____

ลายมือชื่ออาจารย์ที่ปรึกษา_____

ลายมือชื่ออาจารย์ที่ปรึกษาร่วม_____

SUJITTRA CHANDARAK : EFFECTS OF MANGANESE AND COPPER
DOPING ON ELECTRICAL AND MAGNETIC PROPERTIES OF
0.75BiFeO₃-0.25BaTiO₃ CERAMICS. THESIS ADVISOR : ASST. PROF.
SUTHAM SRILOMSAK, Ph.D., 155 PP.

MULTIFFERROIC MATERIALS, PHASE FORMATION, ELECTRICAL
PROPERTY, MAGNETIC PROPERTY, LOCAL STRUCTURE

In this thesis, effects of Cu and Mn doping on electrical and magnetic properties of 0.75BiFeO₃-0.25BaTiO₃ ceramics have been investigated. All the compositions used in this study were prepared based on the B-site substitution (Fe and Ti) with the Cu and Mn contents variation of 1-5 mol%. The traditional mixed oxides with vibro-milling method and typical ceramic processing with calcination and sintering processes were employed to prepare all the samples. The effect of sintering condition on the phase formation was examined by X-ray diffraction. It was found that the ceramics with high purity and relative density in the range of 90-98% could be obtained. Through the measurement by LCR meter, it was revealed that all Cu and Mn doped 0.75BF-0.25BT ceramics exhibited weaker frequency dependent dielectric properties than undoped 0.75BF-0.25BT ceramic. The value of dielectric constant was in the range of 320-480, while the dielectric loss in the range of 0.05-0.15 could be found only in Mn doped 0.75BF-0.25BT samples. The ferroelectric investigation by using a modified Sawyer-Tower circuit could be measured in only 2 mol%Mn doped 0.75BF-0.25BT with remanent polarization in the range of 7.65-7.72 $\mu\text{C}/\text{cm}^2$. The Vibrating Sample Magnetometer was used to investigate magnetic properties and found that all Cu doped 0.75BF-0.25BT samples showed M_r value more than 0.15

emu/g with the highest value of M_r (0.4 emu/g) observed in 4 mol%Cu.

The magnetoelectric property used to identify the potential of materials for possible application in the read head of the hard disk drive technology was also investigated. Good magnetoelectric coefficient could be observed in 2 mol%Mn doped 0.75BF-0.25BT sample sintered at 1025°C, which is thus considered as the optimized composition from this work to be developed in the future read-head of the hard disk drive technology.

Finally, the X-ray Absorption Spectroscopy investigation of the position and valency of Cu and Mn in 0.75BF-0.25BT revealed that the oxidation state of Cu and Mn was Cu^{3+} or a combination of Cu^{3+} and very small amount of Cu^{2+} and of Mn^{4+} and very small amount Mn^{3+} , respectively. Moreover, it was also found that Cu and Mn substituted for both Fe and Ti sites.

School of Ceramic Engineering

Academic Year 2012

Student's Signature_____

Advisor's Signature_____

Co-Advisor's Signature_____

ACKNOWLEDGEMENT

First, I am very thankful to the Synchrotron Light Research Institute (Public Organization) for PhD scholarship and to Suranaree University of Technology for additional support. I am also thankful to my thesis advisors, Asst. Prof. Dr. Sutham Srilomsak and Asst. Prof. Dr. Rattikorn Yimnirun for their invaluable help and constant encouragement throughout the course of this research. I am most grateful for their teaching and advice, not only the research methodologies but also many other methodologies in life. I would not have achieved this far and this thesis would not have been completed without all the support that I have always received from them.

In addition, I am grateful for another support from Assoc. Prof. Dr. Shashank Priya, Virginia Polytechnic Institute and State University, USA. This thesis would not have been finished greatly if there is no kind suggestion from all committees and kind help from Asst. Prof. Dr. Pongsakorn Jantaratana, Kasetsart University, Thailand, for magnetoelectric measurements and others person, Dr. Muangjai Unruan, Mr. Jaru Jutimusik and Mr. Athipong Bootchanont in my research group.

Finally, I most gratefully acknowledge my parents for all their supports throughout the period of this research.

Sujitra Chandarak

TABLE OF CONTENTS

	Page
ABSTRACT (THAI).....	I
ABSTRACT (ENGLISH).....	III
ACKNOWLEDGEMENT.....	V
TABLE OF CONTENTS.....	VI
LIST OF TABLES.....	XII
LIST OF FIGURES.....	XIII
SYMBOLS AND ABBREVIATIONS.....	XXIII
CHAPTER	
I INTRODUCTION.....	1
1.1 Overview.....	1
1.2 Research objectives.....	3
1.3 Scopes.....	4
II LITERATURE REVIEWS.....	5
2.1 Read head technology.....	5

TABLE OF CONTENTS (Continued)

	Page
2.2 Multiferroic materials and magnetoelectric effect.....	6
2.2.1 Order parameter and coupling.....	6
2.2.2 Origin of multiferroic.....	10
2.2.3 Multiferroic and magnetoelectric materials.....	11
2.3 Ferroelectrics.....	13
2.4 Ferromagnetism.....	17
2.5 Perovskite structure.....	25
2.6 Bismuth ferrite-Barium titanate system.....	27
2.7 Dielectric properties.....	30
2.8 X-Ray Absorption Spectroscopy (XAS).....	36
2.8.1 Theory.....	36
2.8.2 Detail of XAS spectra features.....	37
1. XANES.....	37
2. EXAFS.....	38
2.9 Literature reviews.....	39

TABLE OF CONTENTS (Continued)

	Page
3.5.3 Magnetic properties.....	67
3.5.4 X-ray Absorption Spectroscopy at SLRI, Thailand....	68
IV RESULTS AND DISCUSSION.....	70
4.1 Differential Thermal Analysis (DTA).....	70
4.2 Phase formation by X-ray diffraction (XRD).....	71
4.2.1 Calcined powders.....	71
4.2.2 Sintered ceramics.....	73
4.3 Density.....	76
4.3.1 Particle size distribution and packing density of green body.....	76
4.3.2 Relative density.....	80
4.4 Firing shrinkage.....	83
4.5 Microstructure by Scanning Electron Microscope (SEM).....	84
4.6 Physical appearance.....	89
4.7 Electrical properties.....	91

TABLE OF CONTENTS (Continued)

	Page
4.7.1 Dielectric properties.....	91
1. Effect of sintering temperature.....	93
1.1 Cu-doped samples.....	93
1.2 Mn-doped samples.....	95
2. Effect of composition.....	100
4.7.2 Ferroelectric properties.....	102
4.8 Magnetic properties.....	105
4.9 Magnetoelectric coupling.....	109
4.10 X-ray Absorption Spectroscopy (XAS).....	113
4.10.1 Fe K-edge.....	113
4.10.2 Ti K-edge.....	114
4.10.3 Cu K-edge.....	115
4.10.4 Mn K-edge.....	116
4.10.5 Ba L ₃ - and Bi M ₅ -edges.....	116
4.11 Simulation results.....	118

TABLE OF CONTENTS (Continued)

	Page
4.11.1 Fe K-edge.....	118
4.11.2 Ti K-edge.....	119
V CONCLUSIONS AND SUGGESTIONS.....	120
5.1 Conclusions.....	120
5.2 Suggestions.....	121
REFERENCES.....	123
APPENDICES	
APPENDIX A. FIRING SHRINKAGE.....	132
APPENDIX B. PUBLICATIONS.....	135
BIOGRAPHY.....	155

LIST OF TABLES

Table	Page
2.1	The effective ionic radii of B-site cations related to this work.....26
3.1	Specifications of the starting materials.....50
3.2	Calculated lattice parameters and unit cell volume of calcined powders.....60
3.3	The edge, edge-energy, crystal and standard of all elements.....68
3.4	Gas type and Gas pressure.....69
4.1	Packing density of all compositions measured after pressed.....76
4.2	Particle size distribution parameters.....77
4.3	Relative density of all high density samples.....82
4.4	Average grain sizes of all samples sintered at 1025°C.....89
4.5	Dielectric properties of all ceramic samples measured at 1 kHz.....102
4.6	Ferroelectric properties of high density samples.....105
4.7	Magnetic properties of all samples.....109
4.8	Ferroelectric, magnetic and dielectric value of all high density samples.....112

LIST OF FIGURES

Figure	Page
2.1 Schematic of the ferroic orders, conjugated fields and corresponding symmetry operations.....	7
2.2 The relationship between ferromagnetic (FM), ferroelectric (FE), multiferroic (MF) and magnetoelectric (ME) materials.....	8
2.3 Schematic of the different types of coupling.....	9
2.4 Atomic and magnetic structure of BiFeO ₃ . The polarization is pointing along the [111] direction. The magnetic plane is perpendicular to the polarization direction.....	12
2.5 Perovskite BaTiO ₃ unit cell showing ion positions.....	13
2.6 (a) Front view of the cubic BaTiO ₃ structure. This structure can be compared with the structure shown in Figure 2.5 (b) below 120°C, a tetragonal modification of the structure occurs. The net result is an upward shift of cations and a downward shift of anions.....	14
2.7 The tetragonal unit cell shown in Figure 2.6(b) is equivalent to an electric	

LIST OF FIGURES (Continued)

Figure	Page
dipole (with magnitude equal to charge times distance of separation).....	14
2.8 The plot of polarization (P) versus applied electrical field strength (E), a paraelectric material exhibits only a modest level of polarization with applied fields. In contrast, a ferroelectric material exhibits spontaneous polarization in which domains of similarly oriented unit cells grow under increasing fields of similar orientation.....	16
2.9 A ferroelectric hysteresis loop is the result of an alternating electric field. Saturation polarization (P_s) is the result of maximum domain growth. Upon actual field removal, some remanent polarization (P_r) remains. A coercive field (E_c) is required to reach zero polarization.....	17
2.10 Comparison of diamagnetism and paramagnetism on a plot of induction (B) versus magnetic-field strength (H).....	18
2.11 B-H hysteresis loop of ferromagnetic materials.....	19
2.12 Diagram of the magnetic field generated around electron current loop.....	21
2.13 The electron structure of the 3d orbital for transition metals.....	21

LIST OF FIGURES (Continued)

Figure	Page
2.14 Alignment of magnetic moments for pure bcc iron.....	22
2.15 The domain structure of an unmagnetized iron crystal.....	23
2.16 The sharp rise in B during initial magnetization is due to domain growth.....	24
2.17 The domain, or Bloch, wall is a narrow region in which atomic moments change orientation by 180°	24
2.18 The domain microstructures of a ferromagnetic hysteresis loop.....	25
2.19 Illustration of perovskite structure.....	26
2.20 The rounded P-E hysteresis loop of pure BiFeO ₃ ceramic.....	28
2.21 The role of the dielectric in a capacitor.....	33
2.22 Phasor diagram for a perfect capacitor.....	35
2.23 Phasor diagram for a real capacitor.....	35
2.24 XAS-spectrum for the L _{III} edge of Uranium in the substance Calciumuranat (CaUO ₄).....	37
2.25 XRD patterns for 0.7BiFeO ₃ -0.3BaTiO ₃ -x wt.% MnO ₂ solid solution system.....	41

LIST OF FIGURES (Continued)

Figure	Page
2.26	Ferroelectric P–E hysteresis loops for 0.7BiFeO ₃ –0.3BaTiO ₃ –x wt.% MnO ₂ solid solution system.....41
2.27	Ferromagnetic M–H hysteresis loops for 0.7BiFeO ₃ –0.3BaTiO ₃ –x wt.% MnO ₂ solid solution system.....42
2.28	XRD patterns of 0.7Bi(Ga _x Fe _{1-x})O ₃ –0.3BaTiO ₃ ceramics with different Ga contents.....43
2.29	Ferromagnetic M–H hysteresis loops of 0.7Bi(Ga _x Fe _{1-x})O ₃ –0.3BaTiO ₃ ceramics with different Ga contents (room temperature). (a) x = 0, (b) x = 0.025, (c) x = 0.05 and (d) x = 0.1.....43
2.30	Ferroelectric P–E loops of 0.7Bi(Ga _x Fe _{1-x})O ₃ –0.3BaTiO ₃ ceramics with different Ga contents. (a) x = 0; (b) x = 0.025; (c) x = 0.05; (d) x = 0.1.....44
2.31	X-ray diffraction patterns of the BFOC _x –BT ceramics with different Cr contents.....45
2.32	Dielectric constant and loss of the BFOC _x –BT ceramics as a function of frequency with different Cr contents.....45

LIST OF FIGURES (Continued)

Figure	Page
2.33	Ferroelectric P-E hysteresis loops of the $\text{BFOC}_x\text{-BT}$ samples with different Cr contents (a) $x = 0$, (b) $x = 0.05$, (c) $x = 0.1$, and (d) $x = 0.15$46
2.34	Ferromagnetic M- H hysteresis loops of the $\text{BFOC}_x\text{-BT}$ samples with different Cr contents (a) $x = 0$, (b) $x = 0.05$, (c) $x = 0.1$ and (d) $x = 0.15$46
2.35	Temperature dependence of the dielectric constant of $0.75\text{BiFeO}_3\text{-}0.25\text{BaTiO}_3$ ceramic.....47
3.1	Starting materials.....49
3.2	The vibro-milling machine (McCrone micronizing mill).....52
3.3	Calcination diagram of $\text{Bi}_{0.75}\text{Ba}_{0.25}(\text{Fe,Ti})_{1-x}\text{Cu}_x$ or Mn_xO_3 ($x = 0, 1, 2, 3, 4$ and 5 mol\%).....53
3.4	Stainless steel mold for pressing disk samples (diameter = 10 mm).....54
3.5	Hydraulic presser CARVER hydraulic unit model #3912.....54
3.6	Sintering diagram of $\text{Bi}_{0.75}\text{Ba}_{0.25}(\text{Fe,Ti})_{1-x}\text{Cu}_x$ or Mn_xO_3 ($x = 0, 1, 2, 3, 4$ and 5 mol\%).....55
3.7	CARBOLITE RHF 1500 furnace.....55

LIST OF FIGURES (Continued)

Figure	Page
3.8	Arrangement of samples in alumina crucible, white is alumina cover plate, red is alumina powder and black are samples.....56
3.9	Differential Thermal Analyzer DTA7 instrument by Perkin Elmer.....56
3.10	X-ray diffractometer (Bruker D5005).....57
3.11	HORIBA Laser Scattering Particle Size Distribution Analyzer LA-950V2....58
3.12	SEM instrument, JOEL JSM-6400.....62
3.13	Ion sputtering machine JEOL JCF-1100E.....63
3.14	Dielectric measurements system (GW Instek LCR-821).....64
3.15	Sawyer-Tower circuit used for measuring hysteresis loop ($C_o = 0.1 \mu\text{F}$, $C_s = \text{Sample}$, $C_o \gg C_s$).....66
3.16	TREK Model 20/20C High Voltage Amplifier.....67
3.17	VSM components setup for magnetic measurement (LakeShore 7400 series).....67
4.1	DTA curve of undoped 0.75BF-0.25BT powder.....71
4.2	XRD patterns of $\text{Bi}_{0.75}\text{Ba}_{0.25}(\text{Fe,Ti})_{1-x}\text{Cu}_x$ or Mn_xO_3 with $x = 0, 1, 2, 3, 4$

LIST OF FIGURES (Continued)

Figure	Page
and 5 mol% calcined at 900°C.....	72
4.3 XRD patterns of high density samples (a) undoped, (b) Cu and (c) Mn doped 0.75BF-0.25BT ceramics.....	74
4.4 Particle size distribution of (a) undoped, (b) 3 mol% Cu and (c) 3 mol% Mn doped 0.75BF-0.25BT calcined powders.....	78
4.5 SEM micrographs of (a) undoped, (b) 3 mol% Cu, and (c) 3 mol% Mn doped 0.75BF-0.25BT calcined powders.....	79
4.6 Relative density of (a) $\text{Bi}_{0.75}\text{Ba}_{0.25}(\text{Fe},\text{Ti})_{1-x}\text{Cu}_x$ or Mn_xO_3 ceramics at $x = 0, 1, 2, 3, 4$ and 5 mol% with (a) aqueous PVA 2 drops and (b) aqueous PVA 1 drop per gram of sample powders for pressing process....	81
4.7 Firing shrinkage of $\text{Bi}_{0.75}\text{Ba}_{0.25}(\text{Fe},\text{Ti})_{1-x}\text{Cu}_x\text{O}_3$ ceramics at $x = 0, 1, 2, 3,$ 4 and 5 mol% with 1 drop (0.04 grams) aqueous PVA per gram of sample powders for pressing process.....	83
4.8 Firing shrinkage of $\text{Bi}_{0.75}\text{Ba}_{0.25}(\text{Fe},\text{Ti})_{1-x}\text{Mn}_x\text{O}_3$ ceramics at $x = 0, 1, 2, 3,$ 4 and 5 mol% with with 1 drop (0.04 grams) aqueous PVA per gram of	

LIST OF FIGURES (Continued)

Figure	Page
sample powders for pressing process.....	84
4.9 SEM micrographs of high density samples sintered at 1025°C.....	85
4.10 Photographs of $\text{Bi}_{0.75}\text{Ba}_{0.25}(\text{Fe},\text{Ti})_{1-x}\text{Cu}_x\text{O}_3$ and $\text{Bi}_{0.75}\text{Ba}_{0.25}(\text{Fe},\text{Ti})_{1-x}$ Mn_xO_3 sintered at (a) 925°C, (b) 950°C, (c) 975°C, (d) 1000°C and (e) 1025°C (undoped, 1-5 mol% Cu and Mn doped 0.75BF-0.25BT samples, from left to right) mixed with 1 drop of aqueous PVA).....	90
4.11 Frequency dependent dielectric properties of $\text{Bi}_{0.75}\text{Ba}_{0.25}(\text{Fe},\text{Ti})_{1-x}\text{Cu}_x\text{O}_3$ or $\text{Bi}_{0.75}\text{Ba}_{0.25}(\text{Fe},\text{Ti})_{1-x}\text{Mn}_x\text{O}_3$ samples (a) dielectric constant and (b) dielectric loss (measured at 25°C).....	92
4.12 Dielectric properties (a) dielectric constant and (b) dielectric loss of 5 mol% Cu doped 0.75BF-0.25BT ceramics sintered at various temperatures.....	94
4.13 Dielectric constant of (a) 2 mol%, (b) 3 mol%, (c) 4 mol% and (d) 5 mol% Mn-doped 0.75BF-0.25BT ceramics sintered at various temperatures.....	95

LIST OF FIGURES (Continued)

Figure	Page
4.14 Dielectric loss of (a) 2 mol%, (b) 3 mol%, (c) 4 mol% and (d) 5 mol% Mn doped 0.75BF-0.25BT ceramics sintered at various temperatures.....	98
4.15 Dielectric properties (a) dielectric constant and (b) dielectric loss of high density Cu- and Mn-doped 0.75BF-0.25BT ceramics sintered at 1025°C compared with undoped sample.....	100
4.16 Ferroelectric properties of high density samples (a) Cu and (b) Mn doped 0.75BF-0.25BT ceramic samples compared with undoped ceramic sample.....	104
4.17 M-H hysteresis loops of (a) $\text{Bi}_{0.75}\text{Ba}_{0.25}(\text{Fe},\text{Ti})_{1-x}\text{Cu}_x\text{O}_3$ and (b) $\text{Bi}_{0.75}\text{Ba}_{0.25}(\text{Fe},\text{Ti})_{1-x}\text{Mn}_x\text{O}_3$ with $x = 0, 1, 2, 3, 4$ and 5 mol% (sintered at 1025°C).....	107
4.18 M-H hysteresis loops of the high density (a) Cu and (b) Mn doped 0.75BF-0.25BT samples compared with undoped.....	108
4.19 ME coefficients of undoped and 4 and 5 mol% Cu and 2 and 5 mol% Mn doped 0.75BF-0.25BT samples.....	111

LIST OF FIGURES (Continued)

Figure	Page
4.20 XANES spectra of all samples measured at Fe K-edge.....	113
4.21 XANES spectra of the selected samples measured at Ti K-edge.....	114
4.22 XANES spectra of Cu-doped samples measured at Cu K-edge.....	115
4.23 XANES spectra of Mn-doped samples measured at Mn K-edge.....	116
4.24 Ba L ₃ -edge XANES spectra of undoped and Cu and Mn doped 0.75BF-0.25BT samples.....	117
4.25 Bi M ₅ -edge XANES spectra of undoped and Cu and Mn doped 0.75BF-0.25BT samples.....	117
4.26 XANES spectra of Fe K-edge (a) simulated spectra of rhombohedral BiFeO ₃ and (b) measured spectra.....	118
4.27 XANES spectra of Ti K-edge (a) simulated spectra of rhombohedral BaTiO ₃ and (b) measured spectra.....	119

SYMBOLS AND ABBREVIATIONS

ω	=	Angular frequency
χ_E	=	Electric susceptibility
χ_e	=	Electric susceptibility
χ_M	=	Magnetic susceptibility
$\frac{I_0}{\sqrt{2}}$	=	Root mean square current
$\frac{U_0}{\sqrt{2}}$	=	Root mean square voltage
\bar{P}	=	Power loss
μ_0	=	Permeability of vacuum
μ_B	=	Bohr magneton
μ_r	=	Relative permeability
A	=	Area
AFM	=	Antiferromagnetic
AMR	=	Anisotropic magnetoresistance
B	=	Magnetic induction
bcc	=	Body centered cubic

SYMBOLS AND ABBREVIATIONS (Continued)

BF	=	BiFeO ₃
BFOC _x	=	BiFe _{1-x} Cr _x O ₃
B _r	=	Remanent magnetic induction
B _s	=	Saturation magnetic induction
BT	=	BaTiO ₃
C	=	Capacitance
C ₀	=	Capacitance of an empty parallel plate capacitor / Standard capacitor
CF	=	CoFe ₂ O ₄
C _s	=	Sample capacitor
D	=	Electric displacement vector
d	=	Thickness
DC	=	Direct current
D _L	=	Average grain size
DTA	=	Differential thermal analysis
E	=	Electric field/Electrical field strength

SYMBOLS AND ABBREVIATIONS (Continued)

E_c	=	Electric coercive field
EXAFS	=	Extended X-ray absorption fine structure
fcc	=	Face centered cubic
FE	=	Ferroelectricity
FEs	=	Ferroelectric materials
FM	=	Ferromagnetism
GMR	=	Giant magnetoresistance
H	=	Magnetic field/Magnetic field strength
h	=	Thickness
H_c	=	Magnetic coercive field
H_{dc}	=	Direct current magnetic field
HDD	=	Hard disk drive
HS	=	High spin
I	=	Electrical current
I_0	=	Amplitude of current
I_c	=	Instantaneous current

SYMBOLS AND ABBREVIATIONS (Continued)

L	=	Summation of length of the draw lines
LS	=	Low spin
M	=	Magnetization
M_A	=	Atomic mass of A-site atom per unit cell
M_B	=	Atomic mass of B-site atom per unit cell
MCA	=	Magnetoelectric crystalline anisotropy
ME	=	Magnetoelectric
MF	=	Multiferroic
MFs	=	Multiferroic materials
M_O	=	Atomic mass of oxygen atom per unit cell
MPB	=	Morphotropic phase boundary
MR	=	Magnetoresistance
M_r	=	Remanent magnetization
N_A	=	Avogadro's number
n_A	=	Number of A-site atom per unit cell
n_B	=	Number of B-site atom per unit cell

SYMBOLS AND ABBREVIATIONS (Continued)

NF	=	NiFe ₂ O ₄
N _L	=	Number of the grain intercepts with draw lines
n _O	=	Number of oxygen atom per unit cell
p	=	Dipole moment
P	=	Polarization
P _r	=	Remanent polarization
P _s	=	Spontaneous polarization/Saturation polarization
P _{sample}	=	Polarization of the sample
PT	=	Lead Titanate (PbTiO ₃)
PVA	=	Polyvinyl alcohol
PZT	=	Lead zirconate titanate (Pb(Zr,Ti)O ₃)
Q	=	Charge
q	=	Charge
Q ₀	=	Charge on the standard capacitor
Q _s	=	Charge on the electrode of the sample
Q _T	=	Total charge

SYMBOLS AND ABBREVIATIONS (Continued)

R	=	Resistance
RD	=	Relative density
S	=	Electromagnetic source/Percent of volume shrinkage
SEM	=	Scanning Electron Microscopy
ST	=	SrTiO ₃
T	=	Period of time
t	=	Time
tan δ	=	Dissipation factor/Dielectric loss
T _c	=	Curie temperature
TEM	=	Transmission Electron Microscopy
TMR	=	Tunneling magnetoresistance
T _N	=	Neel temperature
T _s	=	Sintering temperature
U	=	Voltage
U ₀	=	Amplitude of voltage
V	=	Volume/Voltage

SYMBOLS AND ABBREVIATIONS (Continued)

V_1	=	Volume of green body
V_2	=	Volume of sintered ceramic
VSM	=	Vibrating Sample Magnetometer
V_x	=	Voltage across the circuit
V_y	=	Voltage across the standard capacitor
W_1	=	Dried weight
W_2	=	Wet weight
W_3	=	Immersed in fluid weight
x	=	Distance/Composition
XANES	=	X-ray absorption near-edge structure
XAS	=	X-ray absorption spectroscopy
XRD	=	X-ray diffraction
Z	=	Atomic number
α	=	Magnetoelectric coefficient
δ	=	Phase difference of I_c and I
ϵ	=	Strain/Permittivity of the dielectric

SYMBOLS AND ABBREVIATIONS (Continued)

ϵ_0	=	Permittivity of free space
ϵ_r	=	Relative permittivity/Dielectric constant
ρ	=	Bulk density
ρ_w	=	Density of water
ρ_{XRD}	=	Calculated density from XRD result
σ	=	Stress/Charge density
σ_p	=	Polarization charge density
σ_T	=	Total charge density
τ	=	Toroidal moment
$\chi(k)$	=	A sum of contributions corresponding to increasing numbers of scattering events

CHAPTER I

INTRODUCTION

1.1 Overview

Anisotropic magnetoresistive (*AMR*), giant magnetoresistive (*GMR*) and tunneling magnetoresistive (*TMR*) materials have been used in the modern magnetic recording read heads for more than half a century (Williams, 2001; Julliere, 1975). In the hard disk drives, the magnetoresistance (*MR*) head flies at constant height above the magnetic domain that defines the “bits” in the recording medium and senses the spatial variation of the stray magnetic field of the domains by a read signal of a voltage amplitude change, $\Delta V = I \times \Delta R$, resulting from a resistance change ΔR of the *MR* sensor. Thus, the operation of the *MR* sensor requires a constant *DC* test current *I* passing through it in order to detect the change in resistance/amplitude. However, the *MR* reader has many extra structures and layers that ensure the proper biasing and shielding of the sensor, which imposes limitations on recording densities. Much effort has been devoted to find new ways to improve the *MR* magnetic-field sensor technology so as to further increase the recording density (Zhang et al., 2008). The possible new read head is based on the magnetoelectric (*ME*) effect in multiferroic (*MF*) materials. *MFs* are multifunctional materials capable of displaying simultaneously magnetic, electric and piezoproperties.

The *MF* state facilitates the occurrence of the *ME* effect, which is defined as the coupling between the electric and magnetic fields in *MF* materials and can be

used for the conversion between energies stored in these fields. The *ME* effect in *MFs* can therefore be electrically or magnetically induced (Vopsaroiu et al., 2008).

Although there are very few multiferroic materials, they are still considered to study for many applications. Bismuth Ferrite or BiFeO_3 (*BF*), a member of multiferroic (*MF*) materials, has the perovskite structure (ABO_3). *BF* is a representative material that shows both the ferroelectric (T_c : 830°C) and antiferromagnetic (T_N : 370°C) characteristics (Jae-wan et al., 2006; Kiselev et al., 1963; Fischer, 1980). The spontaneous polarization of *BF* single crystals has been reported to be $3.5 \mu\text{C}/\text{cm}^2$ along the $\langle 100 \rangle$ direction and $6.1 \mu\text{C}/\text{cm}^2$ along the $\langle 111 \rangle$ direction (Teague et al., 1970). The crystallographic structure of *BF* is a rhombohedrally distorted perovskite structure (Kubel and Schmid, 1990). However, the preparation of pure *BF* in a bulk form without traces of impurities has been a difficult task. On the other hand, Barium Titanate or BaTiO_3 (*BT*), also a perovskite structure (ABO_3) material, is a well known prototype ferroelectric material with excellent electrical properties (for single crystal, T_c : 121°C , P_s : $26 \mu\text{C}/\text{cm}^2$, and $\epsilon_r = 2000$, and for ceramics, T_c : 130°C , P_s : $14.6 \mu\text{C}/\text{cm}^2$, and $\epsilon_r = 1400\text{-}2100$) (Jaffe et al., 1971; Arlt et al., 1985). It is also capable of stabilizing perovskite phase of other perovskite based materials. Therefore, $\text{BiFeO}_3\text{-BaTiO}_3$ solid solution systems have attracted great attention as a means to increase structural stability (Kumar et al., 1998). Previous investigation has already revealed that the $0.75\text{BF}\text{-}0.25\text{BT}$ is the morphotropic phase boundary (*MPB*) of the *BF-BT* ceramic system with the coexistence of both rhombohedral and cubic phases. Nonetheless, the $0.75\text{BF}\text{-}0.25\text{BT}$ ceramic still exhibits relatively low remanant polarization (P_r) of approximately $12 \mu\text{C}/\text{cm}^2$, with coercive field (E_c) of $22 \text{ kV}/\text{cm}$, and density $< 90\%$ the theoretical

density (when sintered at 925 °C) (Chandarak et al., 2009). In this study, we propose that density, dielectric, ferroelectric and ferromagnetic properties of $0.75BF-0.25BT$ ceramics can be increased by substituting multivalent $3d$ transition atoms (Cu and Mn) at B-site of the $0.75BF-0.25BT$ system. It is also expected that the multiferroic material studied in this work can be developed further to use in the hard disk drive read head.

1.2 Research objectives

The objectives of this study are as follows:

- To investigate the effect of manganese and copper doping on electrical and magnetic properties of $0.75BF-0.25BT$ ceramics prepared by the solid state reaction method.
- To study the relationships between sintering conditions, phase formation, density, dielectric, ferroelectric and ferromagnetic properties of the sintered ceramics in the following aspects:
 - Magnetization should be more than 0.15 emu/g.
 - Density is in range of 90-95 %.
 - Dielectric loss should be in the range of 0.05-0.15 and dielectric constant of more than 200.
 - Dielectric constant and dielectric loss of the doped sample have weaker frequency dependence than that of $0.75BF-0.25BT$.
 - Electrical polarization is more than $15 \mu\text{C}/\text{cm}^2$

- To determine the position and valency of Mn and Cu dopants in the $0.75BF-0.25BT$ ceramics with the X-ray absorption spectroscopy technique at Synchrotron Light Research Institute (Public Organization).

1.3 Scopes

- Investigation of effect of manganese and copper doping on electrical and magnetic properties of $0.75BF-0.25BT$ ceramics in $Bi_{0.75}Ba_{0.25}(Fe,Ti)_{1-x}Mn_xO_3$ and $Bi_{0.75}Ba_{0.25}(Fe,Ti)_{1-x}Cu_xO_3$ ceramic systems.
- Utilization of the X-ray absorption spectroscopy technique at Synchrotron Light Research Institute (Public Organization) to investigate the position and valency of Mn and Cu dopants in $Bi_{0.75}Ba_{0.25}(Fe,Ti)_{1-x}Mn_xO_3$ and $Bi_{0.75}Ba_{0.25}(Fe,Ti)_{1-x}Cu_xO_3$ ceramic systems.

CHAPTER II

LITERATURE REVIEWS

This chapter contains the information of read head technology and the possibility of multiferroic materials to be used as a future read head technology based on magnetoelectric effect. The mechanisms for ferroelectric and magnetic properties of BiFeO₃-BaTiO₃ materials are also outlined. Finally, the X-ray absorption spectroscopy technique is explained on the investigation of oxidation state and local structure in materials.

2.1 Read head technology

Magnetoresistance (*MR*) is widely used in read head application due to increasing of recording density. The typical of read heads in hard disk drive (*HDD*) are *AMR*, *GMR* and *TMR*. They have been mentioned on magnetoresistive effect, which their changing on electrical resistance (ΔR) when the read head passes the recording medium with the different magnetic domain. Voltage changing (ΔV) can be observed by using Eq. 2.1 due to the read head is supplied by a constant current (*I*) source, as direct current (*DC*), then the recording data can be collected and related to ΔV (Zhang et al., 2008).

$$\Delta V = I \cdot \Delta R \tag{2.1}$$

Increasing recording density means smaller bit size. The *MR* sensor stack must get thinner and more sensitivity. However, reducing *MR* sensor also brings a number

of complications regarding the horizontal biasing of the sensing layer, the operation frequency of the head, the signal to noise ratio, and construction of the sensor itself, which is a major challenge for a stack under 20 nm. To solve these problems magnetoelectric effect has been studied for a new read head technology (Vopsaroiu et al., 2008).

2.2 Multiferroic materials and magnetoelectric effect

Multiferroic (*MF*) materials are the materials that exhibit two or more ferroic orders, such as magnetic: ferromagnetic (*FM*), antiferromagnetic (*AFM*) or ferromagnetic; ferroelectric (*FE*); ferroelastic; or ferrotoroidic (Velev et al., 2011), as seen in Figure 2.1.

Single-phase *MFs* can exhibit ME effect and promise for information storage applications. But very few such compounds were found that showed *MF* only at low temperature and the *ME* effect was very weak (Velev et al., 2011).

2.2.1 Order parameter and coupling

FE and *FM* materials can be characterized by their spontaneous polarization (electric or magnetic respectively). However, most materials do interact with applied fields but do not exhibit a spontaneous behavior. An electric field (*E*) produces an electric dipole moment and hence electric polarization (*P*) in the material. In contrast, a magnetic field (*H*) produces magnetization (*M*). Stress (σ) produces strain (ϵ). The electromagnetic source vector (*S*) produces toroidal moment (τ). The relationship between the order parameters and the respective fields is illustrated in Figure 2.1 (Velev et al., 2011).

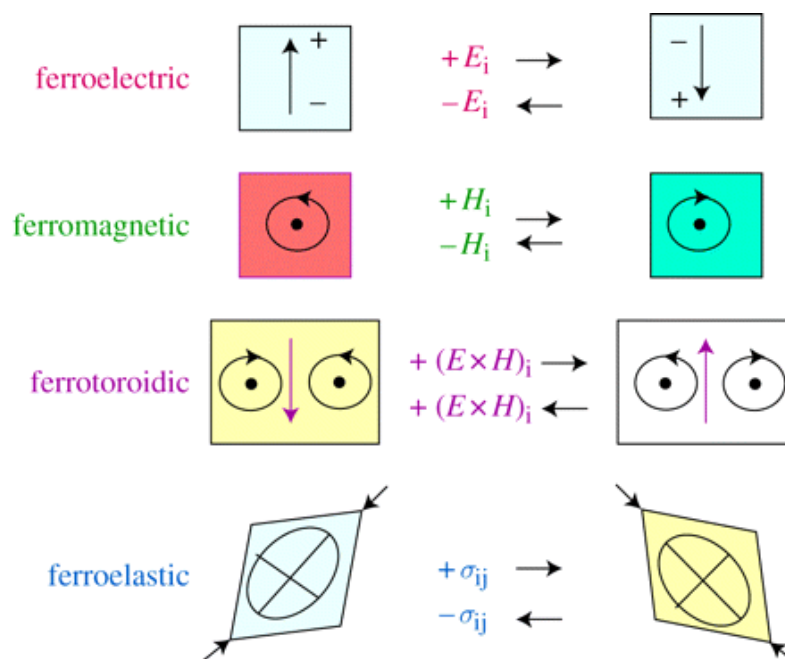


Figure 2.1 Schematic of the ferroic orders, conjugated fields and corresponding symmetry operations (Velev et al., 2011).

Ferromagnetism (ferroelectricity) arises from the spontaneous alignment of atomic magnetic moments (atomic dipole moments), which produces a net magnetization (net polarization). Other ferroic orders exist, such as ferroelastic a spontaneous alignment of microscopic deformations and ferrotoroidic spontaneous toroidal moment. As explained previously, *MFs* are the materials that simultaneously exhibit two or more ferroic orders. The subclass of *MFs* will be concentrated that are simultaneously magnetic and *FE*. The subset of *ME* and *MF* materials is shown in Figure 2.2. The linear coupling is responsible for the piezoelectric, piezomagnetic and *ME* effects. The piezoelectric effect is the ability of a material to induce an electric polarization in response to applied mechanical stress (the inverse piezoelectric effect is inducing strain by applied electric field). Similarly, the piezomagnetic effect is the ability to induce a magnetic polarization in response to applied stress (the inverse

piezomagnetic effect is inducing strain by applied magnetic field). The *ME* effect is the production of electric polarization or conversely magnetization as described previously (Velev et al., 2011).

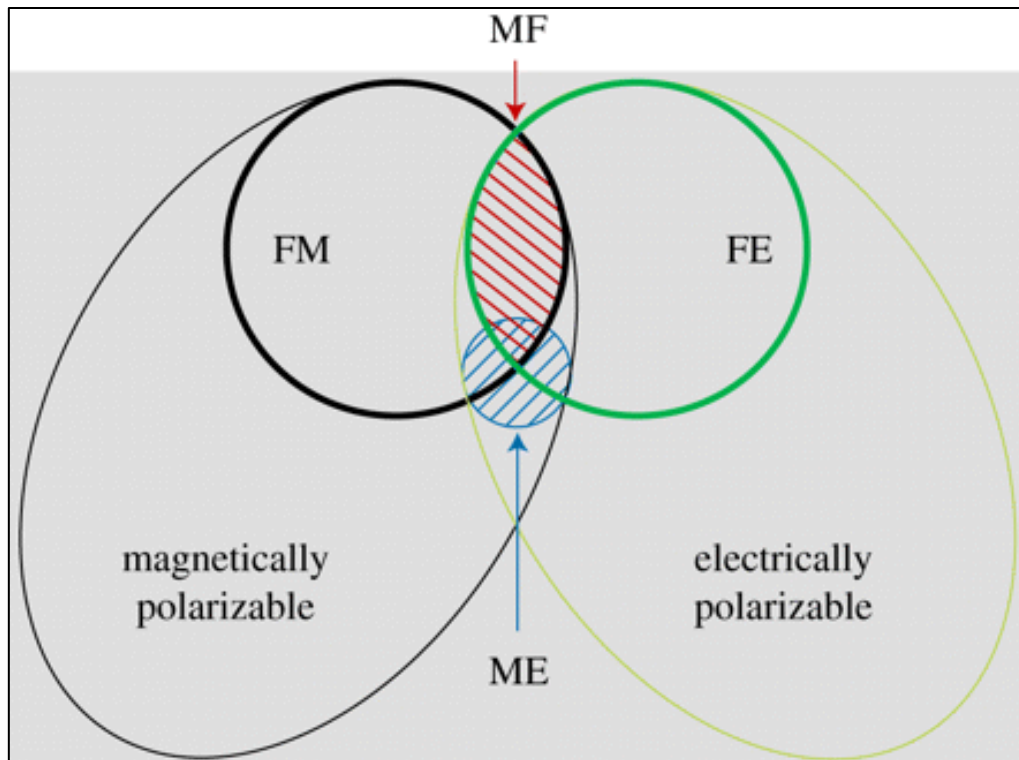


Figure 2.2 The relationship between ferromagnetic (*FM*), ferroelectric (*FE*), multiferroic (*MF*) and magnetoelectric (*ME*) materials (Velev et al., 2011).

The material can be polarized with electric (magnetic) polarization by an applied magnetic (electric) field through the *ME* effect and the bulk *ME* coefficient (susceptibility) is defined by

$$\alpha = \mu_0 \frac{\partial M}{\partial E} = \frac{\partial P}{\partial H} \quad (2.2)$$

in SI units, α is measured in $\text{TmV}^{-1} = \text{sm}^{-1}$

In addition to the intrinsic cross-coupling terms defined by coefficients α , d and q , product couplings can be engineered through a third-order parameter. For example, a common way to engineer ME coupling is through strain. In laminates consisting of piezomagnetic and piezoelectric materials, application of magnetic field causes elastic deformation in a magnetic material, which in turn causes polarization changes in a piezoelectric and vice versa. The resulting ME coefficient of the composite is given by

$$\alpha = \frac{\partial P}{\partial H} = kdq \quad (2.3)$$

where k is a coefficient ($0 \leq |k| \leq 1$) accounting for how well the strain is transferred from one material to the other. The possible couplings between different order parameters are illustrated in Figure 2.3.

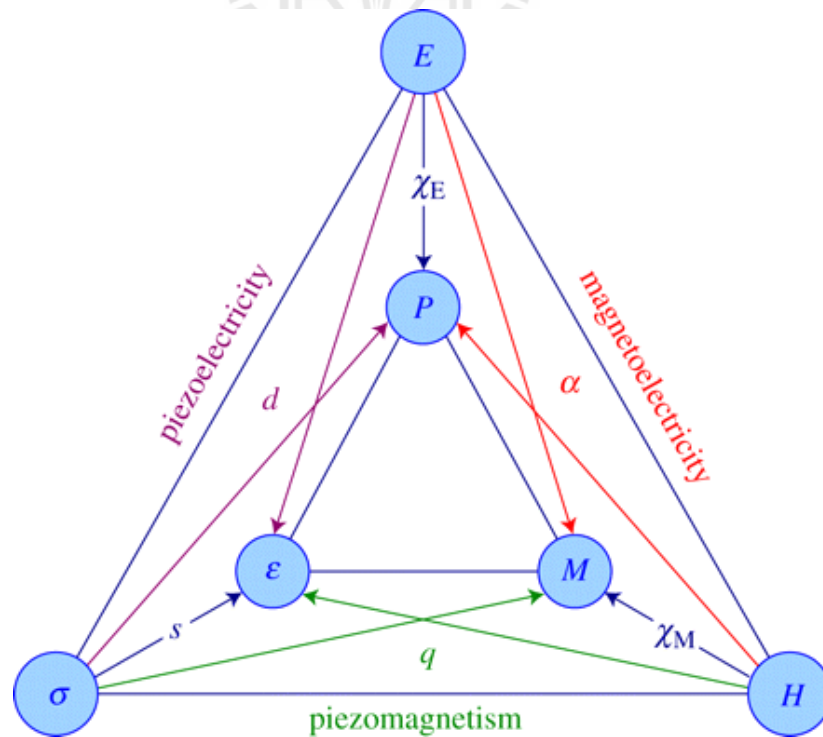


Figure 2.3 Schematic of the different types of coupling (Velev et al., 2011).

2.2.2 Origin of multiferroic

Magnetic and *FE* compounds indicate very little overlap between the two classes of materials. The scanty of *MF* materials could be understood from symmetry argument which materials that can support both magnetic and *FE* order and/or *ME* coupling must have symmetry. Therefore, the number of such materials is very limited because the allowed structures represent a very restricted set of all the possible structures. In addition to symmetry considerations, electronic structure arguments indicate contradicting requirements for ferroelectricity and ferromagnetism to exist in the same material. Two significant conflicting requirements are as follows.

Electrical properties: *FEs* must be insulators because polarization introduces bound charges. If there are free carriers, the charges will be screened and disappearing of the polarization will occur. In other words, ferroelectricity requires filled bands. On the other hand, magnetic materials tend to be metals because ferromagnetism requires partially filled d-bands.

Bonding properties: At least in the conceptually simple perovskite *FEs*, such as BaTiO_3 , the origin of polarization is displacement of the center ion (Ti) with respect to the middle of the oxygen octahedral. This distortion is the result of a balance between an increase in Coulomb repulsion from the neighbouring ions if the ion is moved off-center and the gain in covalent bonding energy when the ion comes closer to one of its neighbours. It seems that the energetics is only favorable when the central ion is in a formally d^0 state. Magnetism produces a partially occupied d^n band, which reduces the bonding contribution (Velez et al., 2011; Khomskii, 2009).

2.2.3 Multiferroic and magnetoelectric materials

The subsistence of the *ME* phenomenon was predicted for Cr₂O₃ and then experimentally observed. The *ME* coefficient was found to be $4 \times 10^{-12} \text{ TmV}^{-1}$, which implies that an applied electric field as large as 10 mV/cm can induce a magnetic moment of only $m \approx 4 \times 10^{-3} \mu_B$ per Cr atom. Such a small value of α can be understood by the fact that, in single-phase materials, the *ME* effect is limited by the geometrical mean of the electric and magnetic susceptibilities

$$\alpha < \varepsilon_0 \mu_0 \chi_E \chi_M \quad (2.4)$$

Eq. 2.4 indicates that the largest *ME* effects can be obtained in *MF* materials that show large value of both susceptibilities. The first *MF* materials were grown by substituting magnetic ions in *FE* perovskite lattices. Some of the important families of *MF* materials are detailed below

Type I: common *MF* materials are those in which the *FE* and magnetic order are produced by different sublattices or parts of the lattice. The *ME* coupling is weak in this type (Velev et al., 2011).

Type II: in these *MFs*, the resulting ferroelectricity is magnetically induced leading to larger *ME* coupling than type I materials. A common feature of this class of *MFs* is a small value of polarization, typically $10^{-4} - 10^{-5} \text{ Cm}^{-2}$ (Velev et al., 2011).

There are other *MF* materials and *ME* coupling mechanisms that have been discovered. Despite this rich phenomenology, bulk single-phase *MF* materials consistently show: weak *ME* coupling, not enough for cross-order parameter control, low Curie and/or Neel temperatures, and little room for improvement.

BiFeO_3 was studied by first principle calculation and found that ionic sublattices of BiFeO_3 in the distorted rhombohedral structure are displaced relative to each other along the polar $[111]$ direction, and the oxygen octahedra are rotated around the same $[111]$ axis, alternately clockwise and counter-clockwise (Figure 2.4). A large spontaneous polarization of $95 \mu\text{C}/\text{cm}^2$ induced by polar displacements as predicted and was found on high-quality single crystals (Velev et al., 2011).

In bulk form of BiFeO_3 as G -type AFM order, the magnetic moment of each Fe cation is antiparallel to that of its nearest neighbours. The calculated magnetocrystalline anisotropy (MCA) predicts that a preferred orientation of the Fe magnetic moments is perpendicular to the polar $[111]$ direction, as shown in Figure 2.4 (Velev et al., 2011).

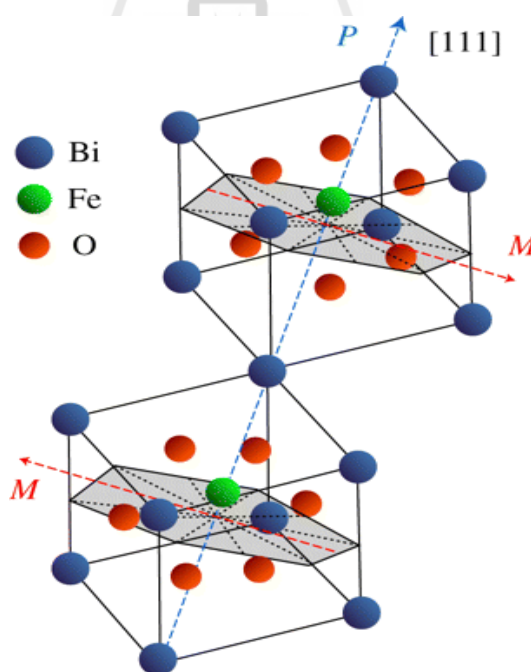


Figure 2.4 Atomic and magnetic structure of BiFeO_3 . The polarization is pointing along the $[111]$ direction. The magnetic plane is perpendicular to the polarization direction (Velev et al., 2011).

2.3 Ferroelectrics

Barium titanate (BaTiO_3) is well known as a representative of ferroelectric material. The crystal structure of BaTiO_3 is the perovskite type, shown in Figure 2.5. For BaTiO_3 , the cubic structure shown in Figure 2.6 is found above 120°C . BaTiO_3 undergoes a phase transformation to a tetragonal structure at temperature below 120°C (Figure 2.6). The transformation temperature (120°C) is called Curie temperature, T_c . BaTiO_3 exhibits typical ferroelectric below T_c (i.e., it can undergo spontaneous polarization) because the tetragonal room-temperature structure of BaTiO_3 (Figure 2.6(b)) is asymmetrical. As a result, the overall center of positive charge for the distribution of cations within the unit cell is separate from the overall center of negative charge for the anion distribution. This structure is equivalent to a permanent electrical dipole in the tetragonal BaTiO_3 unit cell (Figure 2.7). Figure 2.8 shows that, in contrast to a cubic material, the dipole structure of the tetragonal unit cell responds to an applied electric field dramatically (Shackelford, 2005).

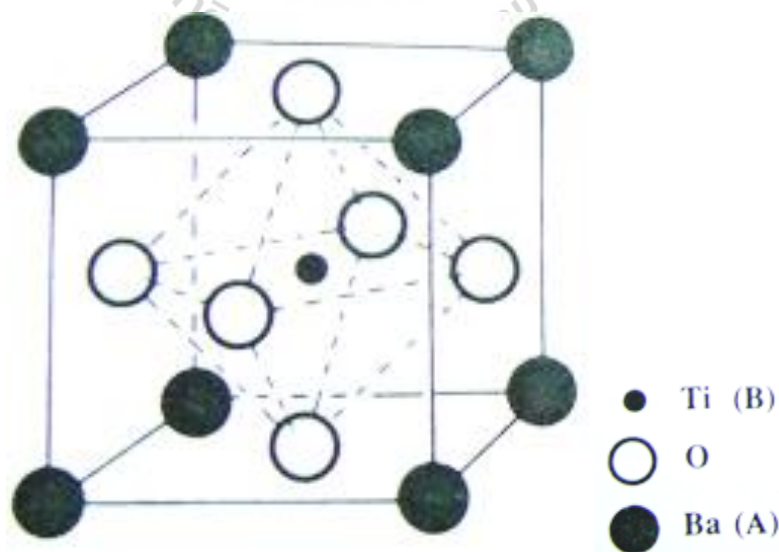


Figure 2.5 Perovskite BaTiO_3 unit cell showing ion positions (Xu, 1991).

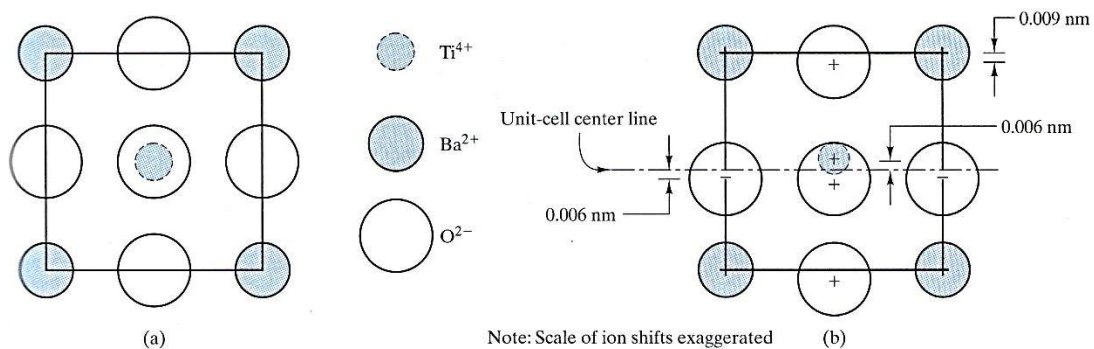


Figure 2.6 (a) Front view of the cubic BaTiO_3 structure. This structure can be compared with the structure shown in Figure 2.5 (b) below 120°C , a tetragonal modification of the structure occurs. The net result is an upward shift of cations and a downward shift of anions (Shackelford, 2005).

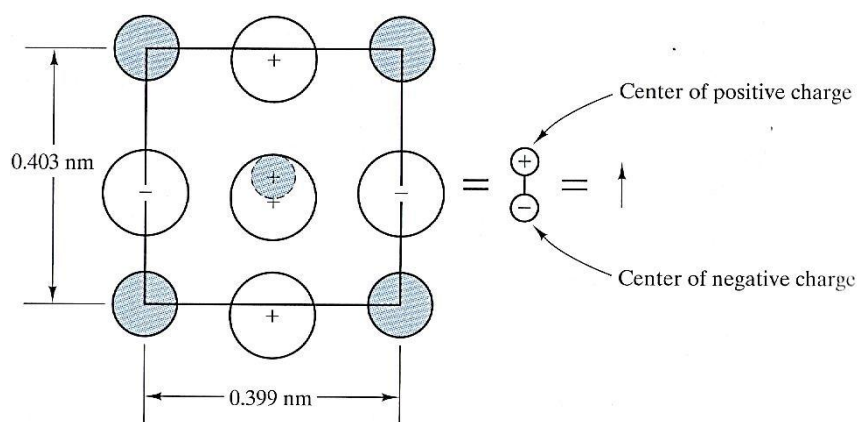


Figure 2.7 The tetragonal unit cell shown in Figure 2.6(b) is equivalent to an electric dipole (with magnitude equal to charge times distance of separation) (Shackelford, 2005).

Without applied electric field the ferroelectric material shows zero polarization due to a random orientation of microscopic-scale domains. Under as applied field, unit-cell dipole orientations roughly parallel to the applied field

direction are favored. In this case, domains with such orientations “grow” at the expense of other, less favorably oriented ones. The specific mechanism of domain wall motion is simply the small shift of ion positions within unit cells, resulting in the net change of orientation of the tetragonal c axis. In contrast, the symmetrical unit-cell material is paraelectric, and only a small polarization is possible as the applied electric field causes a small induced dipole (cations drawn slightly toward the negative electrode, and anions drawn toward the positive electrode) (Shackelford, 2005).

Figure 2.9 summarizes the hysteresis loop that results when the electrical field is repeatedly cycled. Clearly, the plot of polarization versus field does not retrace itself called the hysteresis loop. The saturation polarization, P_s , is the polarization due to maximum domain growth. P_s is extrapolated to zero field ($E=0$) to correct for the induced polarization not due to domain reorientation. The remanent polarization, P_r , is that remaining upon actual field removal. As shown in Figure 2.9, reduction of E to zero does not return the domain structure to equal volumes of opposing polarization. It is necessary to reverse the field to a level E_c (the coercive field) to achieve this result. It is the characteristic hysteresis loop that gives ferroelectricity its name. Ferro-, of course, is a prefix associated with iron-containing materials. But the nature of the P - E curve in Figure 2.9 is remarkably similar to the induction (B)-magnetic field (H) plots for ferromagnetic materials, Figure 2.11 (Shackelford, 2005).

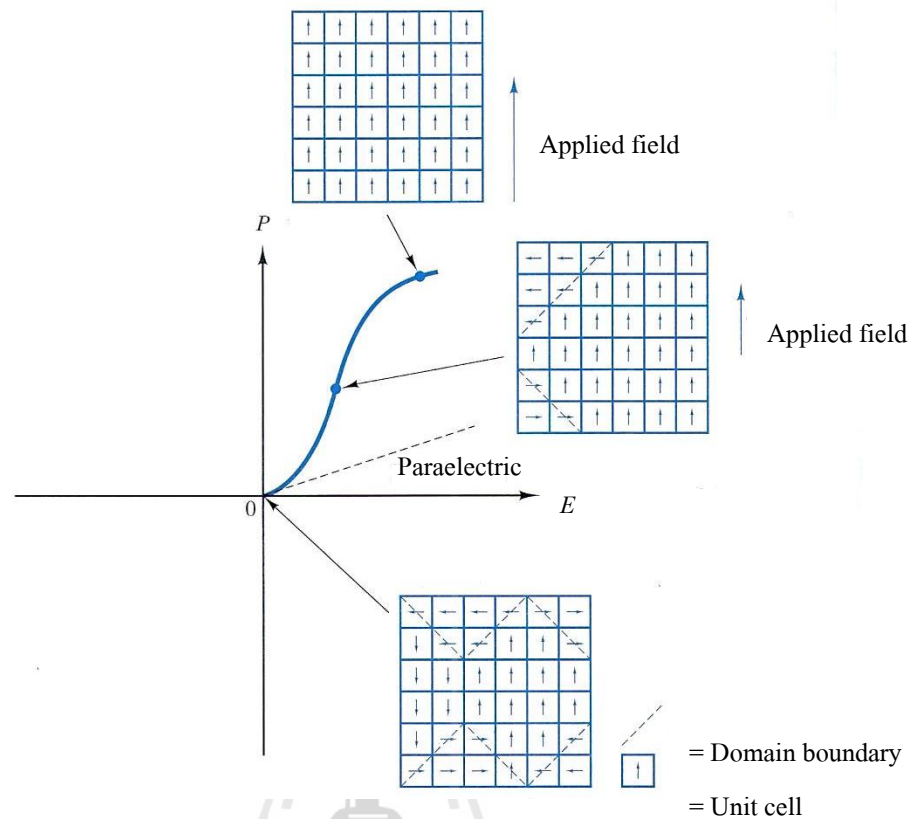


Figure 2.8 The plot of polarization (P) versus applied electrical field strength (E), a paraelectric material exhibits only a modest level of polarization with applied fields. In contrast, a ferroelectric material exhibits spontaneous polarization in which domains of similarly oriented unit cells grow under increasing fields of similar orientation (Shackelford, 2005).

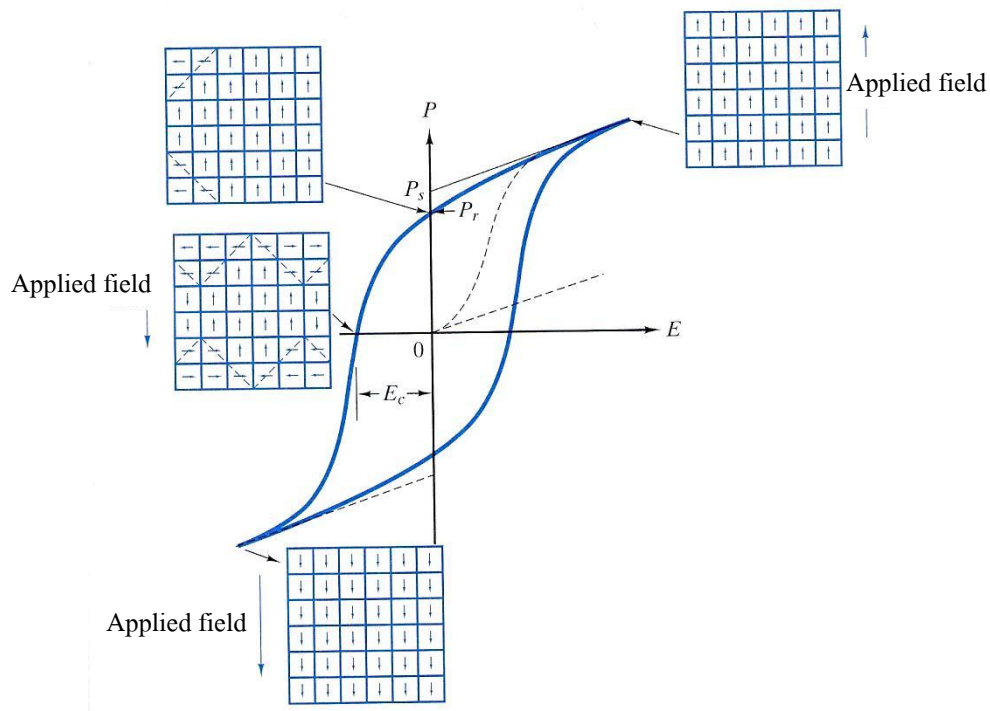


Figure 2.9 A ferroelectric hysteresis loop is the result of an alternating electric field.

Saturation polarization (P_s) is the result of maximum domain growth.

Upon actual field removal, some remanent polarization (P_r) remains. A coercive field (E_c) is required to reach zero polarization (Shackelford, 2005).

2.4 Ferromagnetism

Ferromagnetic materials, the magnetic induction increases dramatically with magnetic field strength. Figure 2.11 illustrates this phenomenon, ferromagnetism, which is in sharp contrast to the simple, linear behavior shown in Figure 2.10. Term of ferromagnetism comes from the early association of the phenomenon with ferrous or iron containing materials. The ferromagnetic behavior can be explained with B - H (the magnetic induction-magnetic field strength) curve as shown in Figure 2.11. The induction, B , is plotted as a function of magnetic field strength, H . The sample was

“demagnetized,” with $B=0$ in the absence of field ($H=0$) at beginning. The initial application of the field generates a slight increase in induction in a manner comparable with that for a paramagnetic material. However, after a modest field increase, a sharp rise in induction will occur. With further increase in field strength, the magnitude of induction levels off at a saturation induction, B_s . The magnetization, M , introduced in Eq. (2.5), is in fact the quantity that saturates (Shackelford, 2005).

$$B = \mu H = \mu_0(H + M) \quad (2.5)$$

where B is the magnetic induction, H is the magnetic field strength, M is the magnetization of the solid and the term $\mu_0 M$ represents the extra magnetic induction field associated with the solid. The magnetization, M , is the volume density of magnetic dipole moments associated with the electronic structure of the solid.

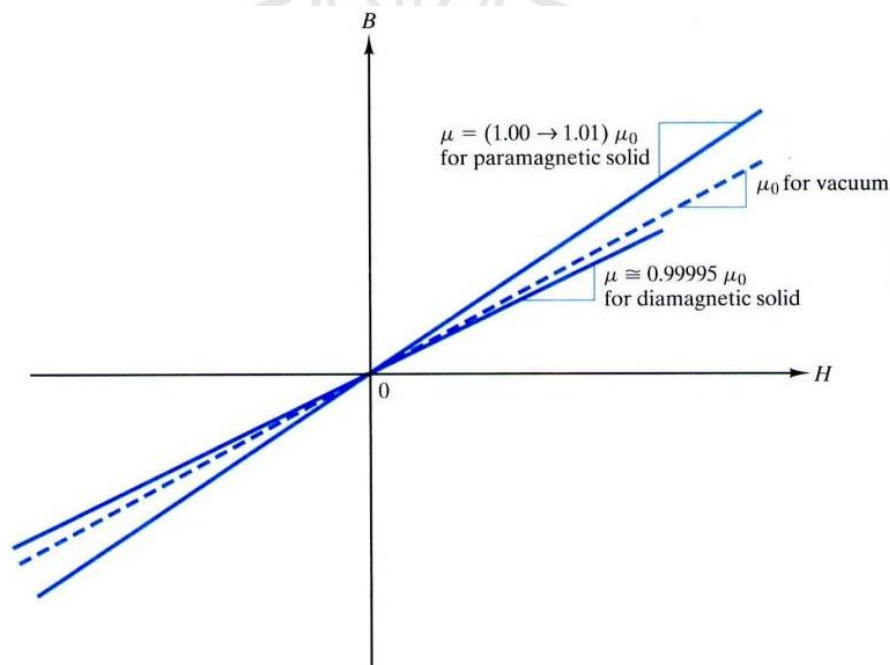


Figure 2.10 Comparison of diamagnetism and paramagnetism on a plot of induction (B) versus magnetic-field strength (H) (Shackelford, 2005).

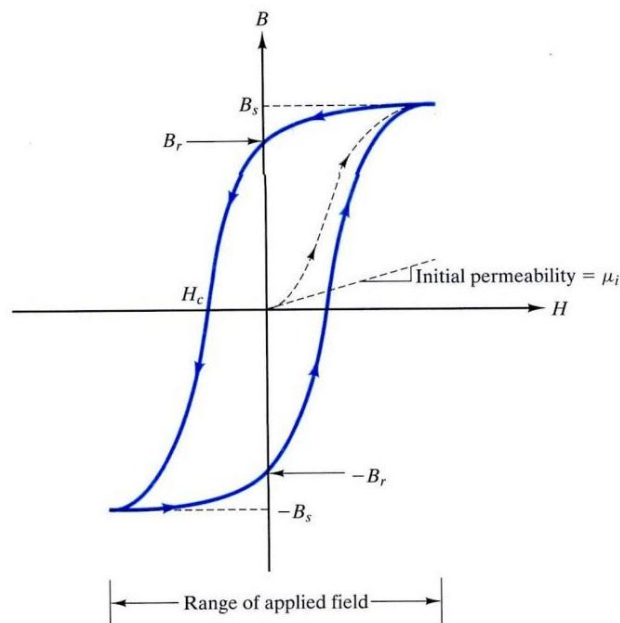


Figure 2.11 B - H hysteresis loop of ferromagnetic materials (Shackelford, 2005).

The units of these various magnetic terms are webers/m² for B (the magnitude of B), webers/ampere-meter or henries/m for μ , and amperes/m for H and M . The magnitude of μ_0 is $4\pi \times 10^{-7}$ H/m ($= \text{N/A}^2$). The relative permeability, μ_r , is frequently used to describe the magnetic behavior of a solid, given by

$$\mu_r \equiv \frac{\mu}{\mu_0} \quad (2.6)$$

A close inspection of Eq. 2.5 indicates that B , which includes a $\mu_0 H$ contribution, will continue to increase with increasing H . Since the magnitude of B is much greater than that of $\mu_0 H$ at the point of saturation, B appears to level off, and the term saturation induction is widely used. In fact, induction never truly saturates (Shackelford, 2005).

Equal in significance to the large value of B_s is the fact that much of that induction is retained upon the removal of the field. Following the B - H curve as the

field is removed (arrows to the left), the induction drops to a nonzero, remanent induction, B_r , at a field strength of $H = 0$. This remanent induction can be removed by applying the sufficiently reversed field, so called coercive field (H_c). By continuing to increase the magnitude of the reverse field, the material can again be saturated (at an induction $-B_s$). As before, a remanent induction ($-B_r$) remains as the field is reduced to zero. The dashed line with arrows in Figure 2.11 represents the initial magnetization, but the solid line represents a completely reversible path that will continue to be traced out as long as the field is cycle back and forth between the extremes indicated and called hysteresis loop (Shackelford, 2005).

To understand the nature of this hysteresis loop, one must explore both the atomic-scale and microscopic-scale structure of the material. As shown in Figure 2.12, a current loop is the source of a magnetic field given orientation. This loop provides a primitive model of a magnetic contribution of the orbital motion of the electrons in an atom as electron spin. Electron spin is actually a relativistic effect associated with the intrinsic angular momentum of the electron. In any case, the magnitude of the magnetic dipole, or magnetic moment, due to electron spin is the Bohr magneton, $\mu_B (= 9.27 \times 10^{-24} \text{ ampere} \cdot \text{m}^2)$. It can be a positive quantity (spin up) or negative quantity (spin down). The orientation of spins is, of course, relative, but it is important in terms of the magnetic contribution of associated electrons. In a filled atom shell, the electrons are all paired with each pair consisting of electrons of opposite spin and zero net magnetic moment ($+\mu_B - \mu_B = 0$). The electronic structure of $3d$ orbital for the transition metal is given in Figure 2.13. Each unpaired electron contributes a single Bohr magneton to the “magnetic nature” of the metal. The number of Bohr magneton per element is given in Figure 2.13. The iron element has

four unpaired $3d$ electrons, and, consequently, a contribution of $4\mu_B$. So, ferromagnetism is clearly associated with iron, but can identify several other transition metals with the same behavior (Shackelford, 2005).

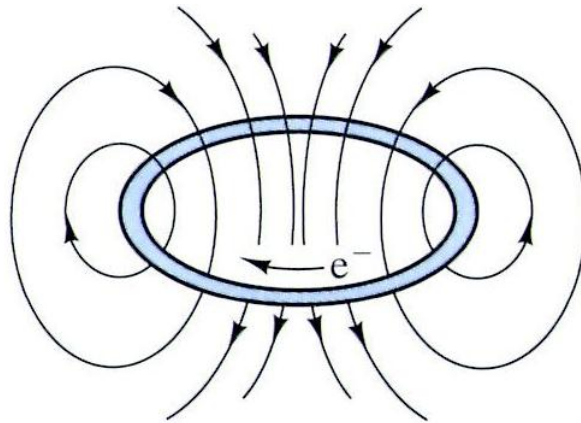


Figure 2.12 Diagram of the magnetic field generated around electron current loop (Shackelford, 2005).

Atomic number	Element	Electronic structure of $3d$	Moment (μ_B)
21	Sc	\uparrow \square \square \square \square	1
22	Ti	\uparrow \uparrow \square \square \square	2
23	V	\uparrow \uparrow \uparrow \square \square	3
24	Cr	\uparrow \uparrow \uparrow \uparrow \uparrow	5
25	Mn	\uparrow \uparrow \uparrow \uparrow \uparrow	5
26	Fe	$\uparrow\downarrow$ \uparrow \uparrow \uparrow \uparrow	4
27	Co	$\uparrow\downarrow$ $\uparrow\downarrow$ \uparrow \uparrow \uparrow	3
28	Ni	$\uparrow\downarrow$ $\uparrow\downarrow$ $\uparrow\downarrow$ \uparrow \uparrow	2
29	Cu	$\uparrow\downarrow$ $\uparrow\downarrow$ $\uparrow\downarrow$ $\uparrow\downarrow$ $\uparrow\downarrow$	0

\uparrow = electronic spin orientation

Figure 2.13 The electron structure of the $3d$ orbital for transition metals (Shackelford, 2005).

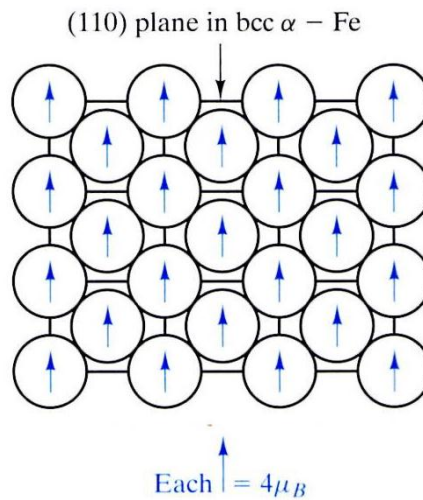


Figure 2.14 Alignment of magnetic moments for pure *bcc* iron (Shackelford, 2005).

The alignments of magnetic moment for adjacent atoms can be used to explain why transition metals can have high value of induction. If adjacent atoms in the crystal structure have their net magnetic moment aligned, the result is a substantial magnetic moment for the bulk crystal (Figure 2.14). The tendency of adjacent atoms to have aligned magnetic moments is a consequence of the exchange interaction between adjacent electron spins in the adjacent atoms. As such, this case is analogous to the electron sharing that is the basis of the covalent bond. The exchange interaction is a sensitive function of crystallography. In α (*bcc*) iron, the degree of interaction (and the resulting saturation induction) varies with crystallographic direction. More significantly, γ (*fcc*) iron is paramagnetic, which allows austenitic stainless steels to be used in designs requiring “nonmagnetic” steels.

Figure 2.14 shows how a high value of induction (B_s) is possible, but it also raises a new question as to how the induction can ever be zero. The answer to this question is by having equal volumes of oppositely oriented moments, the net effect is zero induction. The case of unmagnetized iron crystal with $B = 0$ is shown in Figure

2.15. The microstructure is composed of domains, which have an appearance similar to polycrystalline grains, but differ in meaning. Adjacent domains differ not in crystallographic orientation but in the orientation of magnetic moments. The dramatic rise in induction at the beginning of magnetization is due to a large fraction of the individual atomic moments orienting toward a direction parallel to the direction of an applied field (Figure 2.16). In effect, domains favorably oriented with the applied field “grow” at the expense of those not favorably oriented. That can appreciate the ease with which this growth can occur by noting the magnetic “structure” of the boundary between adjacent domains. The narrow region that show changing of the orientation of atomic moments systematically by 180° is called a Bloch wall as can see in Figure 2.17. During domain growth, the domain wall shifts in a direction to favor the domain more closely oriented with the applied field. Figure 2.18 monitors the domain microstructure during the course of ferromagnetic hysteresis loop (Shackelford, 2005).

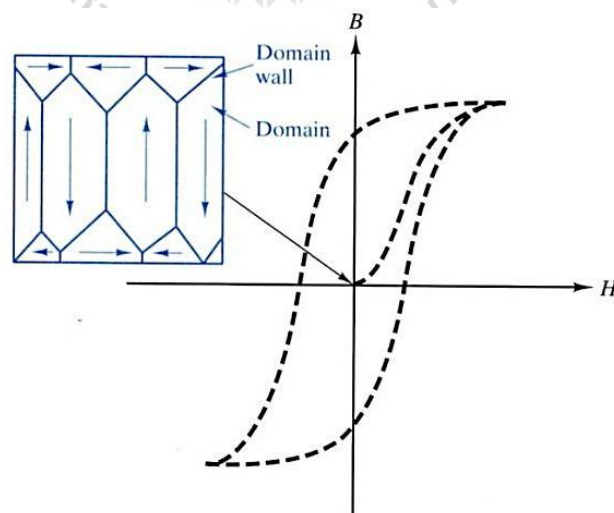


Figure 2.15 The domain structure of an unmagnetized iron crystal (Shackelford, 2005).

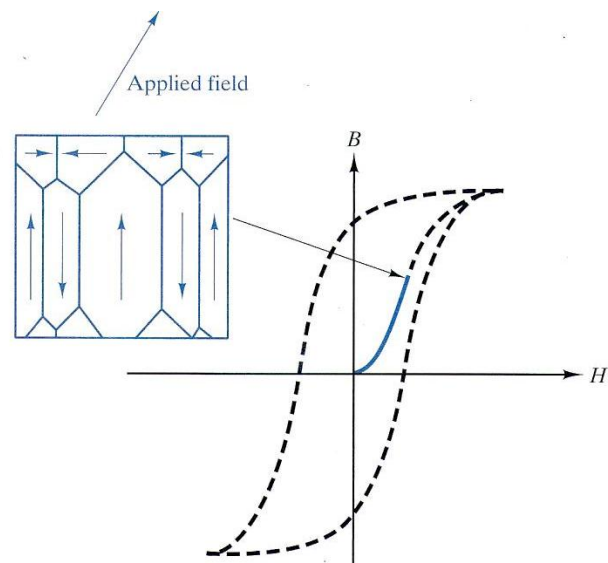


Figure 2.16 The sharp rise in B during initial magnetization is due to domain growth (Shackelford, 2005).

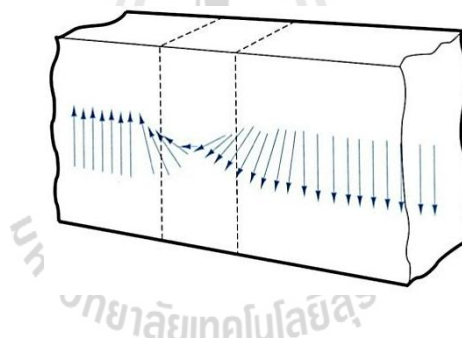


Figure 2.17 The domain, or Bloch, wall is a narrow region in which atomic moments change orientation by 180° (Shackelford, 2005).

In addition, different classes of spontaneous magnetization have been identified when there is more than one magnetic ion per primitive cell of the material, leading to a stricter definition of "ferromagnetism" that is often used to distinguish it from ferrimagnetism. In particular, a material is "ferromagnetic" in this narrower sense only if all of its magnetic ions add a positive contribution to the net magnetization. If some of the magnetic ions subtract from the net magnetization (if

they are partially anti-aligned), then the material is "ferrimagnetic". If the moments of the aligned and anti-aligned ions balance completely so as to have zero net magnetization, despite the magnetic ordering, then it is an antiferromagnet (Shackelford, 2005).

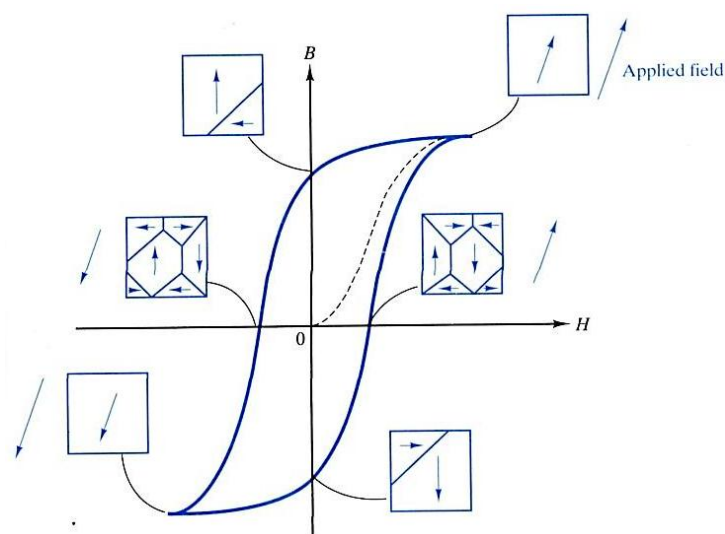


Figure 2.18 The domain microstructures of a ferromagnetic hysteresis loop (Shackelford, 2005).

2.5 Perovskite structure

The ABO_3 where A and B are cations and O is an anion that bonds to both cations is general formula of perovskite structure, as shown in Figure 2.19. At the first glance, the perovskite structure appears to be a combination of simple cubic, bcc , and fcc structures. But closer inspection indicates that different atoms occupy the corner (A -site) and body-centered (B -site) as cation positions and face-centered (O^{2-}) as anion position. As a result, this structure is another example of a simple cubic Bravais lattice. There are five ions per lattice point and per unit cell (Shackelford, 2005). For examples, the B -site cations related to this work are listed in Table 2.1 which HS and

LS refer to high spin and low spin, respectively. These spin states affect to an atom's ionic radius which *LS* has smaller ionic radius than *HS*.

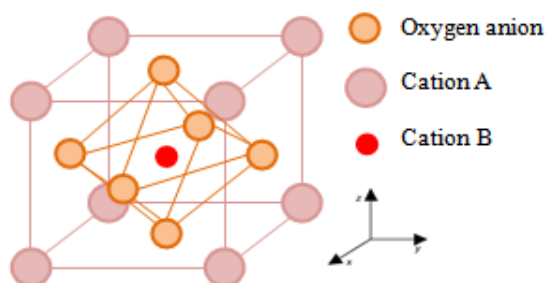


Figure 2.19 Illustration of perovskite structure.

Table 2.1 The effective ionic radii of *B*-site cations related to this work.

Ion	Elec. Config.	Coord. Number	Spin State	Crystal Radius (Å)	Ionic Radius (Å)
Cu^{+2}	$3d^9$	6		0.87	0.73
Cu^{+3}	$3d^8$	6	<i>LS</i>	0.68	0.54
Fe^{+2}	$3d^6$	6	<i>LS</i>	0.75	0.61
Fe^{+2}	$3d^6$	6	<i>HS</i>	0.92	0.78
Fe^{+3}	$3d^5$	6	<i>LS</i>	0.69	0.55
Fe^{+3}	$3d^5$	6	<i>HS</i>	0.785	0.645
Mn^{+3}	$3d^4$	6	<i>LS</i>	0.72	0.58
Mn^{+3}	$3d^4$	6	<i>HS</i>	0.785	0.645
Mn^{+4}	$3d^3$	6		0.67	0.53
Ti^{+4}	$3p^6$	6		0.745	0.605

2.6 Bismuth ferrite-Barium titanate system

The possible mechanism of the coexistence of magnetism and ferroelectricity (multiferroic) is lone-pair driven. The *A*-site drives the displacement and partially filled “*d*” shell on the *B*-site plays a role on the magnetism, the stable of magnetic *d*^{*n*} ion is in the center of its O₆ octahedral. For examples, BiFeO₃ and BiMnO₃, the *A*-site cation (Bi³⁺) has a stereochemically active 6s² lone-pair which causes the Bi 6*p* (empty) orbital to come closer in energy to the O 2*p* orbitals. This leads to hybridization between the Bi 6*p* and O 2*p* orbitals and drives the off-centering of the cation towards the neighboring anion resulting in ferroelectricity (Velev et al., 2011). The polarization and magnetization directions of BiFeO₃ are shown in Figure 2.4.

However, only few multiferroic materials can exhibit both magnetic and ferroelectric properties (Eerenstein et al., 2006; Velev et al., 2011). Recently, the development and research on multiferroic materials have been widely interested. But only BiFeO₃ (*BF*) is the most extensively investigated multiferroics exhibiting *ME* effect at room temperature and promised to use in high recording density (Kuble and Schmid, 1990; Ismailzade et al., 1980; Fujii et al., 1986; Sunder et al., 1995; Wada et al., 1997; Yun et al., 2004; Li et al., 2004; Vopsaroiu et al., 2008). Structure of *BF* is a distorted rhombohedral perovskite structure with *R3c* space group, $a = 5.634 \text{ \AA}$ and $\alpha = 59.348^\circ$. Moreover, *BF* shows both the ferroelectric (T_c : 830°C) and antiferromagnetic (T_N : 370 °C) characteristics (Kiselev et al., 1963; Fischer et al., 1980; Chang et al., 2006). However, *BF* has low resistivity due to oxidation state of iron coupling from Fe³⁺ to Fe²⁺ and lead to oxygen vacancy creation and lower *ME* effect (Wang et al., 2006). With the magnetic moment of pseudo-cubic *BF*, the ferromagnetic coupling will occur along direction <111> and the antiferromagnetic

coupling also occurred between adjacent planes (*G*-type antiferromagnetic). However, the preparation of pure BF in a bulk form without traces of impurities has proven a difficult task (Yoneda et al., 2008; Chandarak et al., 2009). Therefore, BF solid solution systems have attracted great attention as a means to increase structural stability. In addition, another serious problem of *BF*-based ceramics is their low electrical resistivity as described previously, which affects the measurement of ferroelectric (see in Figure 2.20) and dielectric properties at ambient temperatures. Perovskite materials such as BaTiO₃ (*BT*), PbTiO₃ (*PT*) and Pb(Zr,Ti)O₃ (*PZT*) are the ferroelectric materials that have been studied widely. Multiferroic BF material has been mixed with ferroelectric *PT* material and found that it shows higher multiferroic properties, polarization and magnetization than pure *BF*.

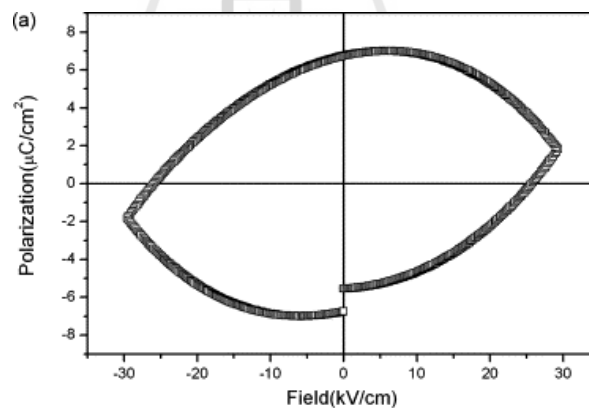


Figure 2.20 The rounded *P-E* hysteresis loop of pure BiFeO₃ ceramic (Mazumder and Sen, 2009).

It is however well known that Pb is the toxic element, so lead-free ferroelectric materials have been studied for mixing with *BF* and still show great properties like *PT*. *BT* is a prototype ferroelectric material with excellent electrical properties (for single crystal, T_c : 121 °C, P_s : 26 $\mu\text{C}/\text{cm}^2$, and $\epsilon_r = 2000$, and for ceramics, T_c : 130 °C,

P_s : $14.6 \mu\text{C}/\text{cm}^2$, and $\epsilon_r = 1400\text{-}2100$) (Jaffe et al., 1971), similar to PT . It is also capable of stabilizing perovskite phase of other perovskite based materials (Chaisan et al., 2005; Chaisan et al., 2006; Chaisan et al., 2007; Yimnirun, 2006; Yimnirun, 2007).

In usual perovskite-based ferroelectrics like BaTiO_3 , the ferroelectric distortion occurs due to the displacement of B -site cation (Ti) with respect to the oxygen octahedral. Here the transition metal ion (Ti in BaTiO_3) requires an empty “ d ” shell since the ferroelectric displacement occurs due to the hopping of electrons between Ti “ d ” and O “ p ” atoms. This normally excludes any net magnetic moment because magnetism requires partially filled “ d ” shells. However, partially filled “ d ” shell on the B -site reduces the tendency of perovskites to display ferroelectricity (Khomskii, 2009).

One of the approaches to obtain materials with multiferroic properties is to suitably mix different kinds of ferroic materials. Considering from a structural viewpoint, barium titanate (BaTiO_3 or BT) is one of very interesting and widely studied perovskite-based ferroelectric materials with excellent electrical properties. Therefore, mixing two excellent prototypic ferroic materials with the same structure (perovskite structure: ABO_3), BT and BF is performed to improve electrical properties and to stabilize the multiferroic BiFeO_3 in the perovskite structure (Chandark, 2008; Chandarak et al., 2009; Itoh et al., 2007).

$\text{BiFeO}_3\text{-BaTiO}_3$ ($BF\text{-}BT$) solid solutions are recently established as multiferroic material that exhibits both ferroelectric and magnetic properties simultaneously. By using the advantage of two coupled ferroic properties based on local off-centered crystal distortion and electron spin, these materials are considered

for many applications (Wang et al., 2009). Ismailzade et al. (1981) reported that crystal structure was rhombohedral between $x = 0$ and 0.33, cubic between $x = 0.33$ and 0.925, and tetragonal over $x = 0.925$. Our previous investigation has also revealed that the $0.75BF-0.25BT$ is the *MPB* of the *BF-BT* ceramic system. Nonetheless, the $0.75BF-0.25BT$ ceramic still exhibits relatively low remanant polarization (P_r) of approximately $12 \mu\text{C}/\text{cm}^2$, with coercive field (E_c) of 22 kV/cm, and density $< 90\%$ the theoretical density (Chandarak et al., 2009).

Since *BF-BT* systems have highly leakage current, the ferroelectric loops show lossy ferroelectric loops and weak magnetization (Chandarak et al., 2009; Itoh et al., 2007). Therefore, further study to improve this system has been carried out by doping with the transition metals or multivalent elements to *A*- or *B*-site because it is expected that these elements can improve the ferroelectric and magnetic properties of the *BF-BT* system (Xiao-Hui et al., 2007; Xiao-Hui et al., 2008).

2.7 Dielectric properties

When applied an electric field to an ideal dielectric material no long range transport of charge occur but only a limited rearrangement that cause a dipole moment and is said to be polarized. Atomic polarization, occurs in all materials, is a little displacement of the electrons in an atom relative with the nucleus, for example, in ionic materials there is the ionic polarization that the displacement relate to cation and anion sub-lattices. The dipolar materials, a simple example is water, can become polarized because the applied electric field orients the molecules. Finally, space charge polarization involves a limited transport of charge carriers until they are stopped at a potential barrier, possibly a grain boundary or phase boundary (Moulson,

and Herbert, 2003).

In its most elementary form, an electric dipole comprises two equal and opposite point charges separated by a distance δx . The dipole moment p of the dipole, defined as

$$p = Q\delta x \quad (2.7)$$

p is a vector with its positive sense directed from the negative to the positive charge.

The effect of filling the space between the plates of a parallel-plate capacitor with a dielectric material is shown in Figure 2.21. From Gauss's theorem, the electric field E between and normal to two parallel plates carrying surface charge density σ and separated by a vacuum is

$$E = \sigma/\varepsilon_0 \quad (2.8)$$

Both situation (a) and situation (b) are applied with the same voltage, so electric field (E) remains the same. However, in situation (b) the polarization charge density σ_p appearing on the surfaces of the dielectric compensates part of the total charge density σ_T carried by the plates. Thus the effective charge density giving rise to E is reduced to $\sigma_T - \sigma_p$ so that

$$E = \frac{\sigma_T - \sigma_p}{\varepsilon_0} \quad (2.9)$$

The total charge density σ_T is equivalent to the magnitude of the electric displacement vector D , so that

$$D = \varepsilon_0 E + P \quad (2.10)$$

If the dielectric is 'linear', so that polarization is proportional to the electric field within the material as the following equation

$$P = \chi_e \varepsilon_0 E \quad (2.11)$$

where χ_e is the electric susceptibility. Unless otherwise stated it will be assumed in the following discussions that P and E are collinear, in which case χ_e is simply a scalar. It follows from Eq. (2.10) and Eq. (2.11) that

$$D = \varepsilon_0 E + \chi_e \varepsilon_0 E = (1 + \chi_e) \varepsilon_0 E \quad (2.12)$$

and, since $D = \sigma_T$,

$$\frac{Q_T}{A} = (1 + \chi_e) \varepsilon_0 \frac{U}{h} \quad (2.13)$$

in which Q_T is the total charge on the capacitor plate. Therefore the capacitance is

$$C = \frac{Q_T}{U} = (1 + \chi_e) \varepsilon_0 \frac{A}{h} \quad (2.14)$$

Since vacuum has zero susceptibility, the capacitance C_0 of an empty parallel plate capacitor is

$$C_0 = \varepsilon_0 \frac{A}{h} \quad (2.15)$$

If the space between the plates is filled with a dielectric of susceptibility χ_e , the capacitance is increased by a factor $1 + \chi_e$. The permittivity ε of the dielectric is defined by

$$\varepsilon = \varepsilon_0 (1 + \chi_e) \quad (2.16)$$

where

$$\frac{\varepsilon}{\varepsilon_0} = 1 + \chi_e = \varepsilon_r \quad (2.17)$$

and ε_r is the relative permittivity of the dielectric or dielectric constant.

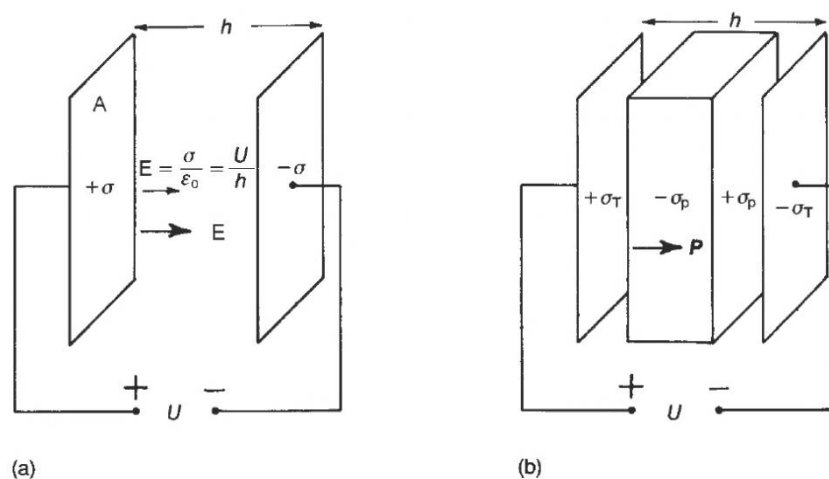


Figure 2.21 The role of the dielectric in a capacitor (Moulson, and Herbert, 2003).

Phasor diagram was used to describe the relationship of the current–voltage for the charging and discharging capacitor (Figure 2.22). A horizontal line is a representative of the applied voltage (U) at a given time and a vertical line is the instantaneous current (I_c) which leads the voltage by 90° . The ‘phasor’ diagram is an instantaneous snapshot of the voltage and current vectors as they rotate in an anticlockwise sense with angular frequency ω , maintaining a constant phase difference (Moulson, and Herbert, 2003).

If there is to be a net extraction of power from the source, there must be a component I_l of I in phase with U , as shown in Figure 2.23; I_l leads to power loss, whereas the capacitive component I_c does not. Therefore the time average power loss is

$$\bar{P} = \frac{1}{T} \int_0^T UI dt \quad (2.18)$$

$$= \frac{1}{T} \int_0^T U_0 \sin(\omega t) I_0 \cos(\omega t - \delta) dt \quad (2.19)$$

Integrating Eq. (2.19) gives

$$\bar{P} = \frac{1}{2} U_0 I_0 \sin \delta \quad (2.20)$$

since $I_0 = I_c / \cos \delta$ and $I_c = \omega U_0 C$,

$$\bar{P} = \frac{1}{2} U_0 I_c \tan \delta = \frac{1}{2} U_0^2 \omega C \tan \delta \quad (2.21)$$

where \bar{P} is the power loss

T is the period of time

t is time

U_0 is the amplitude of voltage

I_0 is the amplitude of current

δ is the phase difference of I_c and I

$\frac{U_0}{\sqrt{2}}$ is the root mean square voltage

$\frac{I_0}{\sqrt{2}}$ is the root mean square current

It can be seen from Eq. (2.20) that $\sin \delta$ (or $\cos \phi$) represents the fraction of the current–voltage product that is dissipated as heat. It is termed the ‘power factor’. From Eq. (2.21), the ‘dissipation factor’ $\tan \delta$ is the fraction of the product of the capacitive current (the component 90° out of phase with the voltage) and the voltage, dissipated as heat. In most cases of interest δ is small enough for $\sin \delta \approx \tan \delta$.

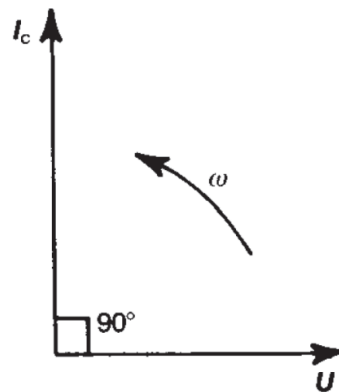


Figure 2.22 Phasor diagram for a perfect capacitor (Moulson, and Herbert, 2003).

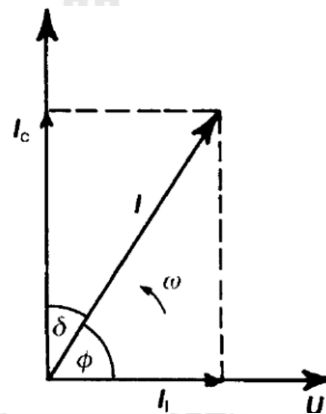


Figure 2.23 Phasor diagram for a real capacitor (Moulson and Herbert, 2003).

Eq. (2.21) can be put in terms of dielectric material parameters by substituting E_0h for U_0 , $\epsilon_r\epsilon_0A/h$ for C and V for Ah , leading to the equation for the dissipated power density in the dielectric:

$$\frac{\bar{P}}{V} = \frac{1}{2} E_0^2 \omega \epsilon_0 \epsilon_r \tan \delta \quad (2.22)$$

$\epsilon_r \tan \delta$ is termed the ‘loss factor’ of the dielectric and $\omega \epsilon_0 \epsilon_r \tan \delta$ is the ‘dielectric (or a.c.) conductivity, as followed

$$\sigma_{a.c.} = \omega \epsilon_0 \epsilon_r \tan \delta \quad (2.23)$$

2.8 X-Ray Absorption Spectroscopy (XAS)

2.8.1 Theory

The XAS, in range of soft X-ray, is the technique used for investigating the atomic structure of materials based on interaction between electrons and nucleus. Photon energy is absorbed by electron that has the same energy. The absorbed electron moves to the higher energy level and hole is generated. The energy level of hole can be used as the name of edge absorption, such as if the electron at *K* level is excited to higher level and hole occurs in this level it is called *K*-edge absorption. XAS can divide into two regions, X-ray absorption near-edge structure (*XANES*) and extended X-ray absorption fine structure (*EXAFS*). *XANES* is the observed spectrum at the low energy, covering photon energy up to about 40 eV above the absorption edge. *EXAFS* is observed at the higher energy from 40 eV up to ~1000 eV above the absorption edge. The *XANES* measurement can be used to determine the specific atom. The region of *XANES* and *EXAFS* is shown in figure 2.24. The inserted figures c) and d) show schematically the reinforcing and cancellation of electron waves (Harald, 2011). Furthermore, the *EXAFS* measurement allows the identification of the nearest neighboring atoms to the absorbing atom to determine the coordination environment for the atoms of interest. From Figure 2.24, the *XANES* area is fairly complicated, caused by a large number of recombination effects in the electron shell of the central atom such as many-body interaction, particle-hole interaction and multiple scattering. *XANES* investigations are usually done in conjunction with other experiments. This area is still being developed as a measurement method for various applications. The next area of the spectrum, away from the edge, is characterised by smaller and apparently more regular vibrations and referred to as *EXAFS*.

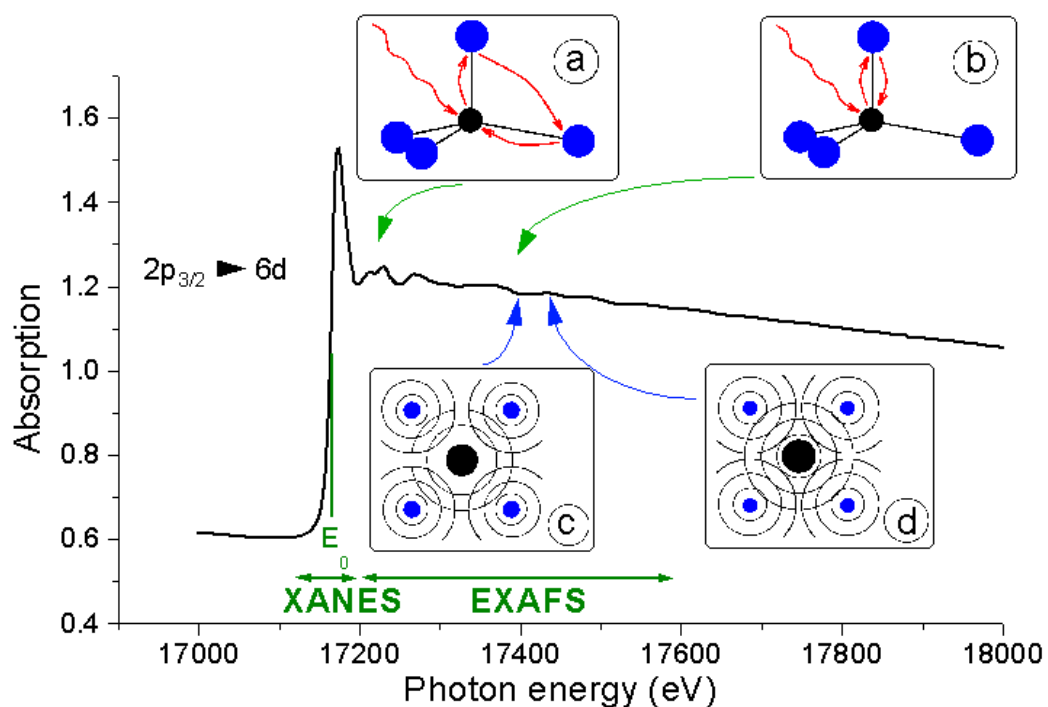


Figure 2.24 XAS-spectrum for the L_{III} edge of Uranium in the substance Calciumuranat (CaUO_4) (Harald, 2011).

2.8.2 Detail of XAS spectra features

1. XANES

Meaning of XANES spectra is the summation of pre-edge, edge and XANES.

Pre-edge are often found in transition metal XANES spectra. At present their main utility has been as an indicator of local site symmetry and orbital occupancy. It is useful to describe them in term of molecular orbital theory, although in some cases a quantitative analysis may require more detailed treatment in term of multiplets. In transition metals such as Mn there are $3d$ orbitals with energies in the pre-edge region that mix with ligand (and other metals) orbitals to make molecular orbitals (Bunker, 2010).

Edge shifts: it is clear from simple physical arguments that shifts of a few eV can indeed occur by transferring charge, but the amount of charge transfer that actually occurs in chemical binding is much less than the formal charge would suggest. Atoms remain nearly neutral even when chemical bonds are formed (Bunker, 2010).

2. EXAFS

The $\chi(k)$ spectrum consists of a sum of sine wave with amplitudes that depend on the type of atoms, and how they are distributed. Rapid oscillations in the data correspond to long path lengths. A complex wave pattern indicates a well-ordered structure. Usually, the more distant atoms are more highly disordered (if only because of thermal vibrations). If the amplitudes of the data decay rapidly above the edge, the backscatterers are probably of low atomic number. In most cases the contributions from nearby atoms $R < 3\text{\AA}$ is considerably stronger than more distant atoms $R > 3\text{\AA}$, so slower oscillations are normally stronger than the fast oscillations. The scattering amplitudes of light (low atomic number Z) atoms decay more quickly above the edge than higher Z atoms. For a high Z atom, depending on location in k of the minima in the amplitudes, the amplitude may actually increase and then decrease. If the atoms of a particular type have a large spread in distances the EXAFS amplitude will decay more rapidly above the edge (Bunker, 2010).

Atoms that differ in atomic number by about a row in the periodic table tend to have scattering phases that differ by about $\approx \pi$ radians, and if they occur at about the same distance they tend to interfere destructively and cancel out. The same effect occurs to a lesser degree if there is any phase difference between the scatterers. If two well defined groups of atoms are a few tenths of an \AA apart they

will produce “beats,” in which the combined amplitude oscillates. This beat pattern can be determined the difference in distance.

Beats: in EXAFS it is common to refer to groups of atoms at a similar distance as a coordination “shell”. Because of geometrical constraints (finite size) and chemical bonding, it is normal for the nearest neighbors to group at similar distances, making up the first shell of atoms. It is also typical for the radial distribution of atoms to have a minimum following the first shell maximum, and then rise to another maximum (second shell) at a larger distance. In crystal, it persists to large distances, even when thermal motion is taken into account. *EXAFS* is insensitive to such long-range order, however, except indirectly through its modest sensitivity to vibrational structure (Bunker, 2010).

2.9 Literature reviews

ME composites incorporate both ferroelectric (*FE*) and ferromagnetic (*FM*) phases which make them ready for technological applications. Vopsaroiu et al. (2008) proposed the new design of magnetic recording read head based on the *ME* effect by using the bulk trilayered *ME* composites of Terfenol-D/Pb(Zr,Ti)O₃/Terfenol-D. They estimated the output voltage of such a *ME* laminate of nanosized layers by using the approach for bulk *ME* laminates. The two extra antiferromagnetic (*AMF*) layers were added adjacent to the *FM* Terfenol-D layers to construct a *ME* sensor stack consisting of seven layers (compared with 15 in a typical *MR* head) arranged as seed/*AMF*/*FM*/*FE*/*FM*/*AMF*/cap. This *ME* read head does not need *DC* test current as required in the *MR* read heads because data are directly read back as an induced *ME* output voltage. This shows a clear benefit regarding Joule thermal heating issues that

occur in the high resistance tunneling *MR* sensor and also reduces the power consumption. However, it is hard to realize this proposed *ME* head design based on Terfenol-D/Pb(Zr,Ti)O₃/Terfenol-D laminate.

Zhang et al. (2008) reported the prototype *ME* read head using the simple *ME* heterostructures consisting of alternating layers of magnetic and *FE* oxides. A convincing direct *ME* effect in the bilayered heterostructure of ferrites (*e.g.* NiFe₂O₄ (*NF*) and CoFe₂O₄ (*CF*)) and BaTiO₃ (*BT*) grown in SrTiO₃ (*ST*) single crystal substrate has been observed. The result clearly showed that the bilayered thin film exhibited good coexistence of the evident *FE* and *FM* hysteresis loops. The bilayered thin films illustrate well-defined *ME* sensing to the applied magnetic field and the *ME* output clearly follows the magnetic excitation signal.

However, the very low response signals of the read heads need to be improved. Furthermore, the smaller size and simple structure read heads are needed to offer the possibility to increase the recording density. According to these requirements, single phase multiferroic material, such as *BF-BT* proposed in this study, is one of possible materials for the future hard disk drive read head. Previous investigations have focused on the ferroelectric and ferromagnetic properties of *BF-BT* systems, as detailed follow paragraph.

Binary solid solutions 0.7BiFeO₃-0.3BaTiO₃-*x* wt. % MnO₂ (*x* = 0, 0.2, 0.3 and 0.5) prepared by solid state mixed oxide method were studied by Xiao Hui et al. (2008). They found that Mn-dopant can improve the sintering ability of this system when MnO₂ content is below 0.3 wt.%. When MnO₂ exceeds 0.3 wt.%, the sintering ability is weakened and the phase structure of this system changes from rhombohedral into tetragonal phase (shown in Figure 2.25). With increasing concentration of MnO₂,

the resistivity increases at first and then decreases. The structure of the specimen for $x = 0.3$ is in the morphotropic phase boundary (*MPB*), which provides better polarization properties (shown in Figure 2.26). With increasing Mn content, the coercive electric field decreases at first and then increases, while the remanent magnetization (M_r) increases and the coercive magnetic field decrease (shown in Figure 2.27).

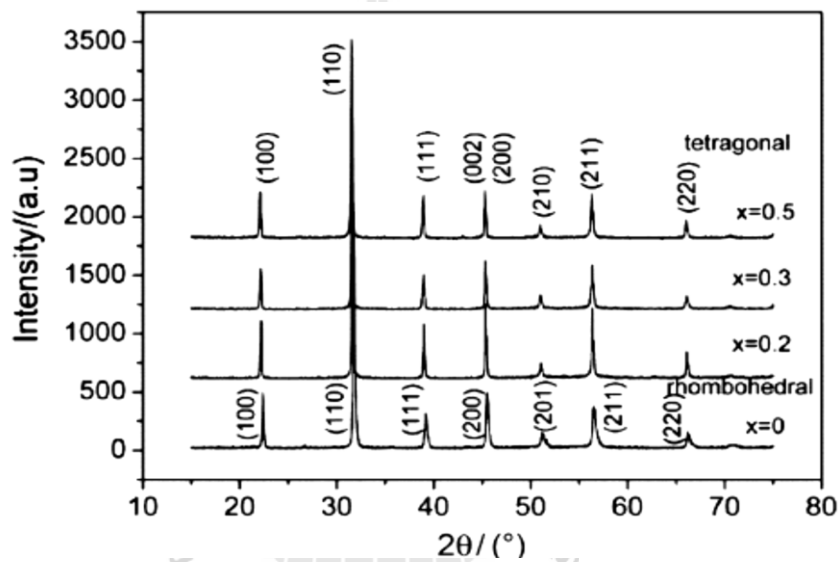


Figure 2.25 XRD patterns for $0.7\text{BiFeO}_3-0.3\text{BaTiO}_3-x$ wt.% MnO_2 solid solution system (Xiao-Hui et al., 2008).

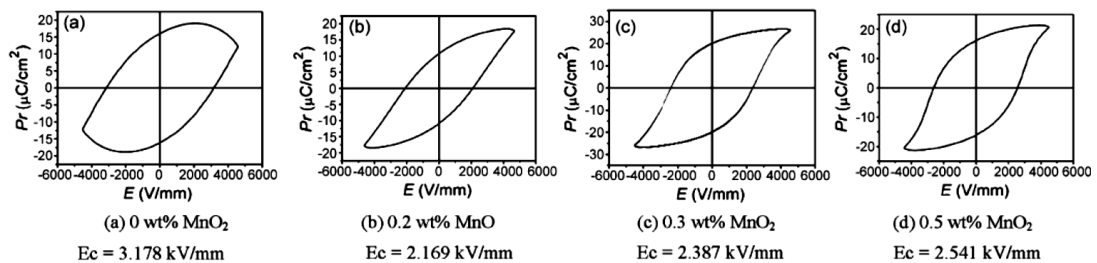


Figure 2.26 Ferroelectric $P-E$ hysteresis loops for $0.7\text{BiFeO}_3-0.3\text{BaTiO}_3-x$ wt.% MnO_2 solid solution system (Xiao-Hui et al., 2008).

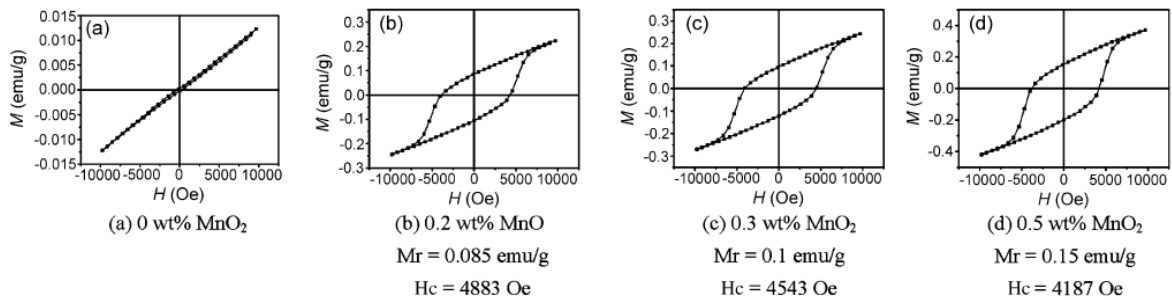


Figure 2.27 Ferromagnetic M - H hysteresis loops for $0.7\text{BiFeO}_3\text{-}0.3\text{BaTiO}_3\text{-}x$ wt.% MnO_2 solid solution system (Xiao-Hui et al., 2008).

Xiao-Hui et al. (2007) investigated the effects of gallium doping on microstructure, ferromagnetic, ferroelectric, dielectric properties and conductivity on the binary solid solutions $0.7\text{Bi}(\text{Ga}_x\text{Fe}_{1-x})\text{O}_3\text{-}0.3\text{BaTiO}_3$ ($x = 0, 0.025, 0.05, 0.1$) ceramics prepared by traditional ceramic process. The results indicated that Ga-dopant could improve the sintering ability of the solid solution when the Ga content x was below 0.05. When x was over 0.05, the sintering ability of the solid solution was weakened, and the phase structure of $0.7\text{BiFeO}_3\text{-}0.3\text{BaTiO}_3$ solid solution changed from rhombohedral to tetragonal ferroelectric phase (as shown in Figure 2.28). The electrical resistivity increased with the Ga content. With the Ga content increasing, the remanent magnetization (M_r) increased and the magnetic coercive field H_c decreased (as shown in Figure 2.29). However, the remanent polarization (P_r) fluctuated, increasing firstly and decreasing later (as shown in Figure 2.30).

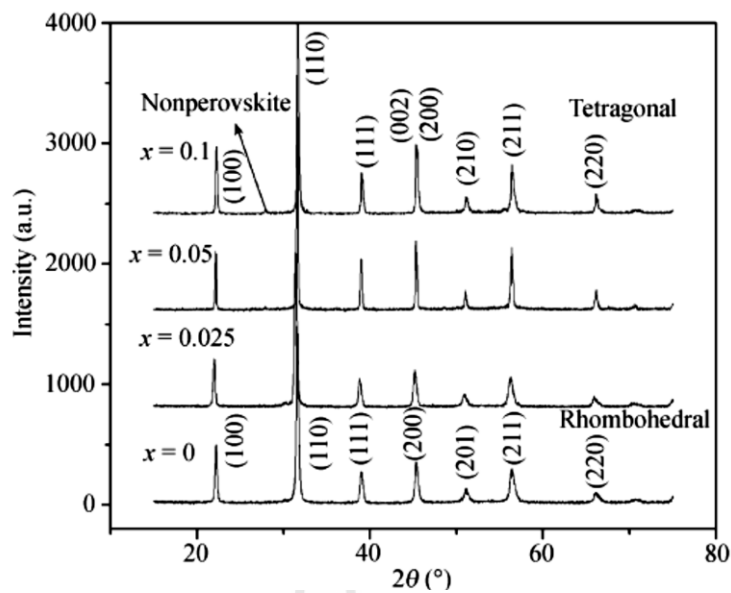


Figure 2.28 XRD patterns of $0.7\text{Bi}(\text{Ga}_x\text{Fe}_{1-x})\text{O}_3-0.3\text{BaTiO}_3$ ceramics with different Ga contents (Xiao-Hui et al., 2007).

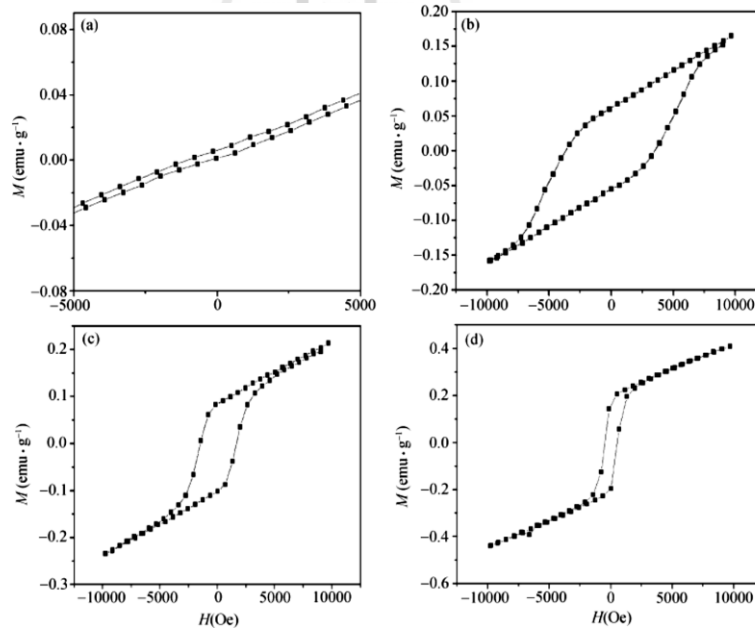


Figure 2.29 Ferromagnetic M - H hysteresis loops of $0.7\text{Bi}(\text{Ga}_x\text{Fe}_{1-x})\text{O}_3-0.3\text{BaTiO}_3$ ceramics with different Ga contents (room temperature). (a) $x = 0$, (b) $x = 0.025$, (c) $x = 0.05$ and (d) $x = 0.1$ (Xiao-Hui et al., 2007).

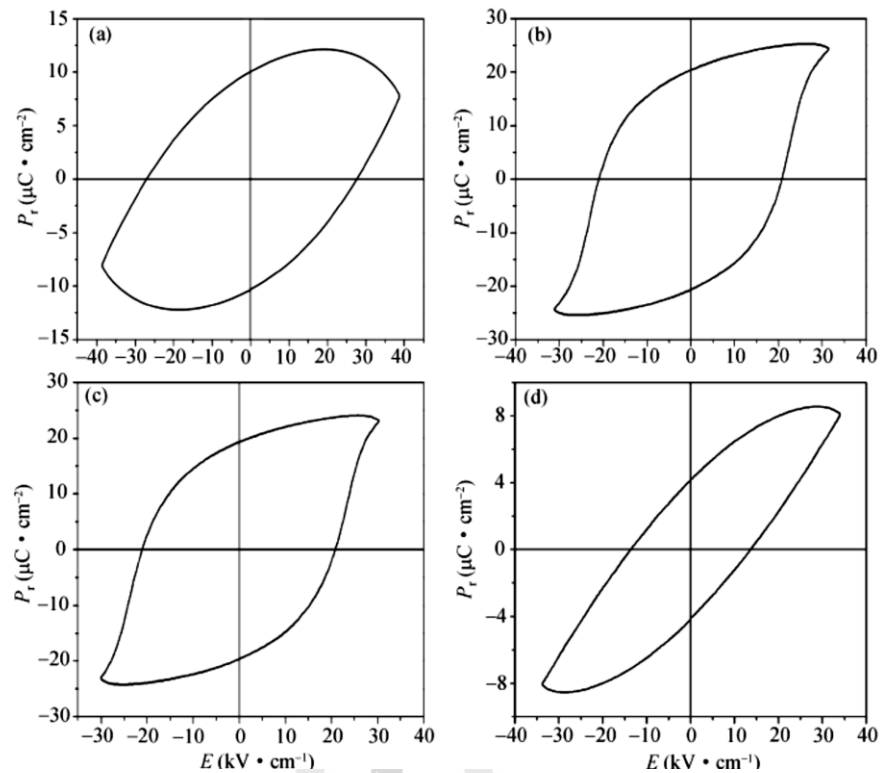


Figure 2.30 Ferroelectric P - E loops of $0.7\text{Bi}(\text{Ga}_x\text{Fe}_{1-x})\text{O}_3\text{-}0.3\text{BaTiO}_3$ ceramics with different Ga contents. (a) $x = 0$; (b) $x = 0.025$; (c) $x = 0.05$; (d) $x = 0.1$ (Xiao-Hui et al., 2007).

Xiao-Hui et al. (2008) studied the ferroelectric and ferromagnetic properties of $\text{BiFeO}_3\text{-BaTiO}_3$ doped with Cr at B -site ($0.7\text{BiFe}_{1-x}\text{Cr}_x\text{O}_3\text{-}0.3\text{BaTiO}_3$ ($\text{BFOC}_x\text{-BT}$, with $x = 0\text{-}0.2$)) prepared by using the traditional mixed oxide method. They found that all sintered ceramics showed single phase of rhombohedral perovskite structure for $x = 0\text{-}0.15$. The ceramic with $x = 0.2$ showed non-perovskite phases (as shown in Figure 2.31), but exhibited the largest dielectric constant (Figure 2.32). At $x > 0.1$, dielectric loss started to increase likely caused by dielectric relaxation which mainly resulted from oxygen vacancies, and became stronger with the content of Cr. All samples showed P - E loop with rounded corners, indicating significant conductive

losses, as shown in Figure 2.33. The $BFOC_x-BT$ solid solutions exhibited symmetric magnetic hysteresis loops, indicating that they are magnetically ordered materials (as shown in Figure 2.34).

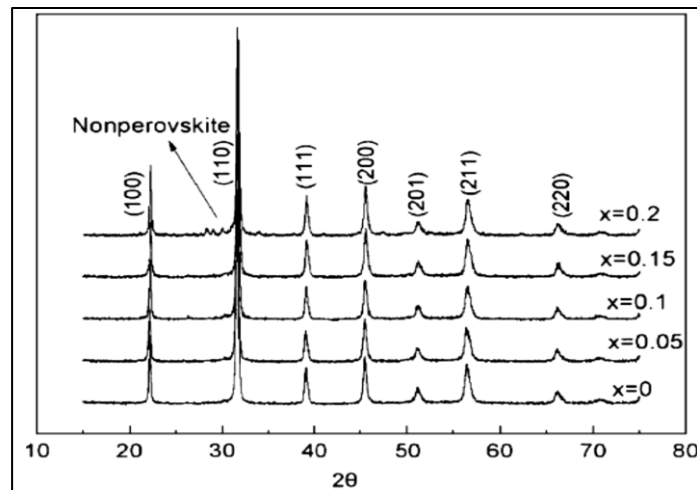


Figure 2.31 X-ray diffraction patterns of the $BFOC_x-BT$ ceramics with different Cr contents (Xiao-Hui et al., 2008).

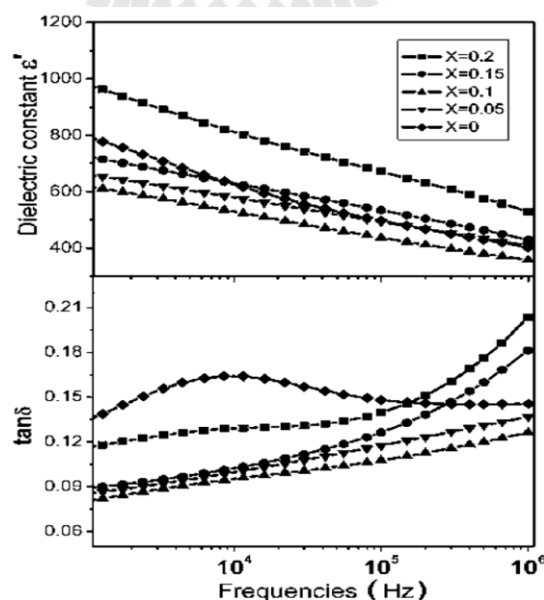


Figure 2.32 Dielectric constant and loss of the $BFOC_x-BT$ ceramics as a function of frequency with different Cr contents (Xiao-Hui et al., 2008).

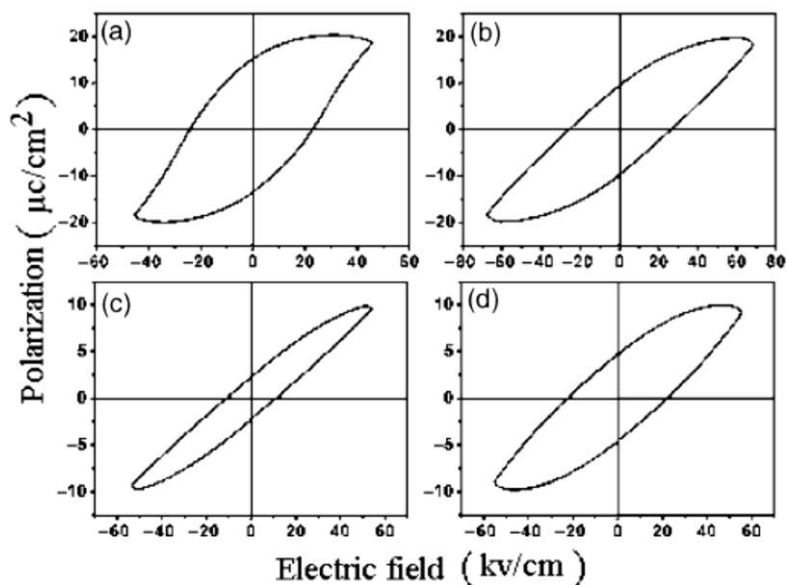


Figure 2.33 Ferroelectric P - E hysteresis loops of the $BFOC_x$ - BT samples with different Cr contents (a) $x = 0$, (b) $x = 0.05$, (c) $x = 0.1$, and (d) $x = 0.15$ (Xiao-Hui et al., 2008).

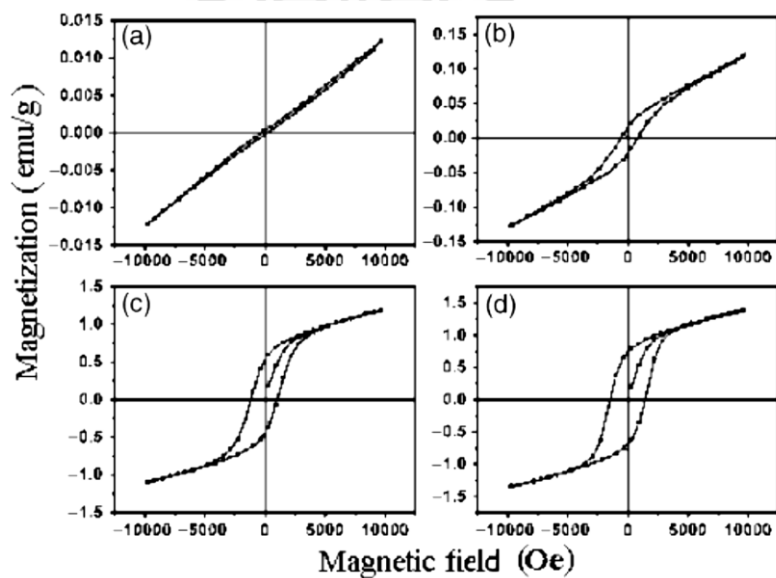


Figure 2.34 Ferromagnetic M - H hysteresis loops of the $BFOC_x$ - BT samples with different Cr contents (a) $x = 0$, (b) $x = 0.05$, (c) $x = 0.1$ and (d) $x = 0.15$ (Xiao-Hui et al., 2008).

The changes of dielectric constant and ferroelectric domain structures of the $0.75\text{BiFeO}_3\text{-}0.25\text{BaTiO}_3$ ceramics as a function of temperature in the range between 25°C and 527°C were investigated by Ozaki and Mori (2009). It was found that the dielectric constant exhibited a broad peak at around 500°C (as shown in Figure 2.35) which consistency with the obtained result from TEM technique that ferroelectric phase of $0.75\text{BiFeO}_3\text{-}0.25\text{BaTiO}_3$ and a rhombohedral to pseudocubic transition was observed at around 500°C .

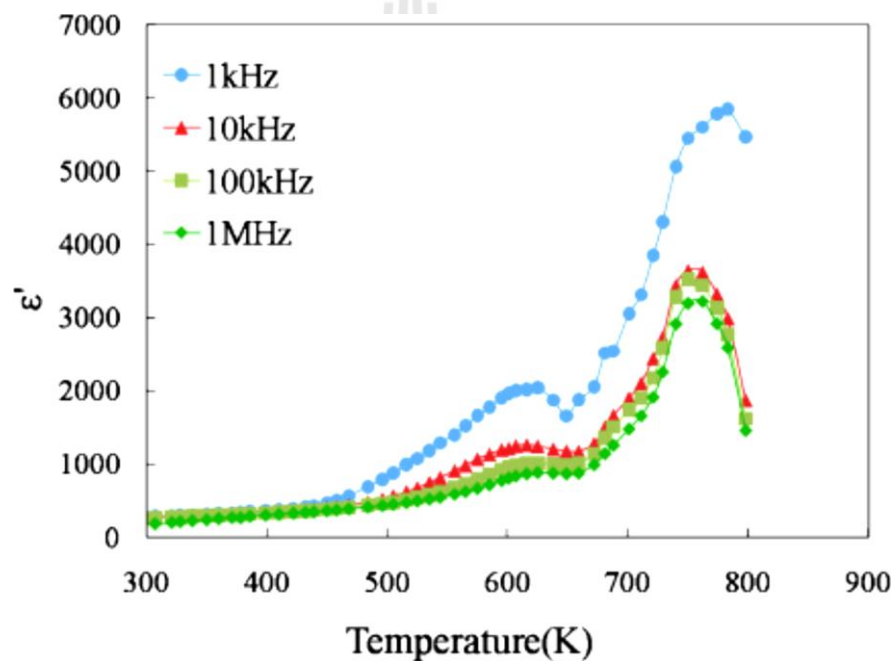


Figure 2.35 Temperature dependence of the dielectric constant of $0.75\text{BiFeO}_3\text{-}0.25\text{BaTiO}_3$ ceramic (Ozaki and Mori, 2009).

CHAPTER III

EXPERIMENTAL PROCEDURES

This chapter describes materials and equipments, sample preparations, characterizations and properties of the samples in $\text{Bi}_{0.75}\text{Ba}_{0.25}(\text{Fe,Ti})_{1-x}\text{Mn}_x\text{O}_3$ and $\text{Bi}_{0.75}\text{Ba}_{0.25}(\text{Fe,Ti})_{1-x}\text{Cu}_x\text{O}_3$ systems with $x = 0, 0.01, 0.02, 0.03, 0.04$ and 0.05 .

3.1 Materials and equipments

1. BaCO_3 purity $\geq 98.5\%$, SIGMA-ALDRICH
2. TiO_2 purity 99%, SIGMA-ALDRICH
3. Bi_2O_3 purity 99.9%, ALDRICH
4. Fe_2O_3 purity $\geq 99.0\%$, FLUKA
5. MnO_2 purity 99.99%, SIGMA-ALDRICH
6. CuO purity 99.9999%, ALDRICH
7. Vibro-milling machine
8. Ethanol
9. Sieve 90 mesh
10. Beaker
11. Alumina crucible
12. Spatula (stainless steel)
13. Mortar
14. Aqueous polyvinyl alcohol (*PVA*) binder with a concentration of 1%

15. Stainless steel mold (diameter 10 mm.)
16. Hydraulic press
17. Silver paint
18. Hot Plate
19. Aluminium foil
20. Silicone Oil
21. Grinding/polishing machine
22. Alumina powder
23. Alumina plate



Figure 3.1 Starting materials.

Table 3.1 Specifications of the starting materials.

Chemical	Trace element
Bi ₂ O ₃	Trace Metal Analysis ≤ 2000.0 ppm
Fe ₂ O ₃	Chloride (Cl) ≤ 0.1% Sulfate (SO ₄) ≤ 0.1% Ca ≤ 0.01% Cd ≤ 0.001% Co ≤ 0.005% Cr ≤ 0.001% Cu ≤ 0.005% K ≤ 0.005% Mg ≤ 0.005% Mn ≤ 0.3% Na ≤ 0.02% Ni ≤ 0.005% Pb ≤ 0.005% Zn ≤ 0.005% Chloride (Cl) ≤ 0.03% Ca ≤ 0.1% Cd ≤ 0.005%

Table 3.1 Specifications of the starting materials (Continued).

Chemical	Trace element
BaCO ₃	Co ≤ 0.005% Cu ≤ 0.005% Fe ≤ 0.005% K ≤ 0.01% Na ≤ 0.2% Ni ≤ 0.005% Pb ≤ 0.005% Sr ≤ 1.5% Zn ≤ 0.005%
TiO ₂	As ≤ 0.0001% Fe ≤ 0.005% Pb ≤ 0.002% Sb ≤ 0.005%
CuO	Trace Metal Analysis ≤ 20.0 ppm
MnO ₂	Trace Metal Analysis ≤ 200.0 ppm

3.2 Powder preparation

Powders of $\text{Bi}_{0.75}\text{Ba}_{0.25}(\text{Fe,Ti})_{1-x}\text{Mn}_x\text{O}_3$ and $\text{Bi}_{0.75}\text{Ba}_{0.25}(\text{Fe,Ti})_{1-x}\text{Cu}_x\text{O}_3$ systems were prepared by using solid state reaction method. BaCO_3 , TiO_2 , Bi_2O_3 , Fe_2O_3 , MnO_2 and CuO powders corresponding to $\text{Bi}_{0.75}\text{Ba}_{0.25}(\text{Fe,Ti})_{1-x}\text{Mn}_x\text{O}_3$ and $\text{Bi}_{0.75}\text{Ba}_{0.25}(\text{Fe,Ti})_{1-x}\text{Cu}_x\text{O}_3$ ($x = 0, 1, 2, 3, 4$ and 5 mol%) compositions were mixed by vibro-milling technique (Vibro-milling machine shown in Figure 3.2) and three batches of 20 grams for each composition were mixed. Chemical formula of $\text{Bi}_{0.75}\text{Ba}_{0.25}\text{Fe}_{0.75(1-x)/2}\text{Ti}_{0.25(1-x)/2}\text{Cu}_x\text{O}_3$ and $\text{Bi}_{0.75}\text{Ba}_{0.25}\text{Fe}_{0.75(1-x)/2}\text{Ti}_{0.25(1-x)/2}\text{Mn}_x\text{O}_3$ were used in this study.



Figure 3.2 The vibro-milling machine (McCrone micronizing mill).

The mixing steps for all mixtures were as follows:

- Put all starting materials into the container with ethanol as mixing agent
- Put the container into the vibro-milling machine (at Chiang Mai University) and then mill for 30 minutes
- Wash the container to obtain the mixture
- Dry at 100°C for 12 hours

In this study, we used calcination temperature at 900°C (one step calcination) for 5 hours with heating/cooling rate of 5°C/min, and leaved the samples in the furnace to room temperature (30°C). The calcination step is shown in Figure 3.3.

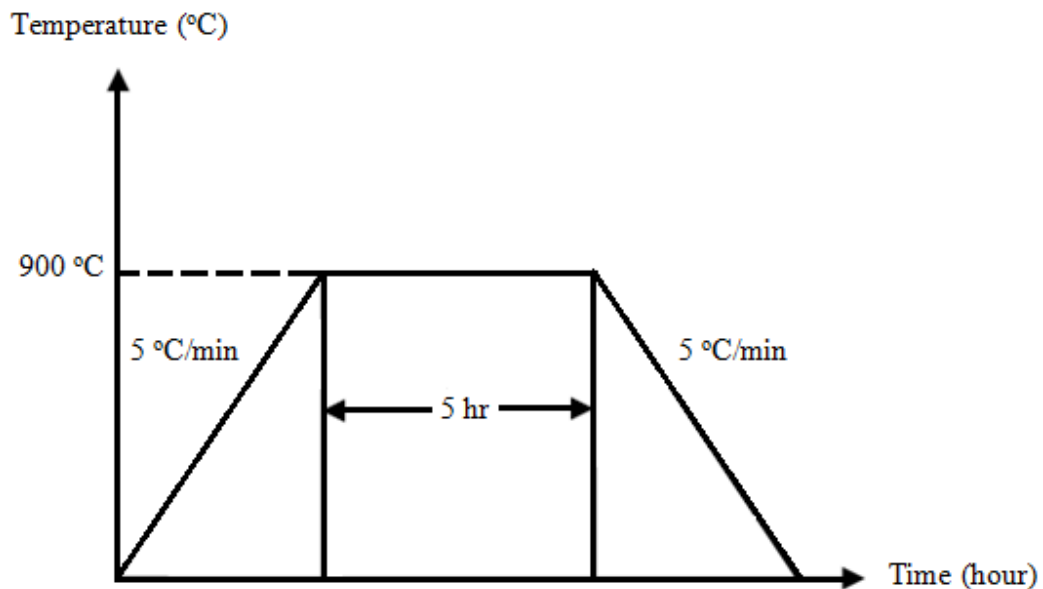


Figure 3.3 Calcination diagram of $\text{Bi}_{0.75}\text{Ba}_{0.25}(\text{Fe,Ti})_{1-x}\text{Cu}_x$ or Mn_xO_3 ($x = 0, 1, 2, 3, 4$ and 5 mol%).

3.3 Ceramic preparation

All calcined powders were sieved with sieve size 90 mesh and then weighted for 1 gram of each composition and mixed with 1 drop (0.04 grams) of the aqueous polyvinyl alcohol (PVA) binder with a concentration of 1%. The stainless steel mold with diameter of 10 mm (shown in Figure 3.4) was used in pressing process. The calcined powders were pressed as disk under a pressure of 130 MPa by using hydraulic presser CARVER hydraulic unit model #3912 (shown in Figure 3.5) and then sintered at 925, 950, 975, 1000 and 1025°C for 2 hours in air with heating/cooling rate of 5°C/min (as shown in Figure 3.6).



Figure 3.4 Stainless steel mold for pressing disk samples (diameter = 10 mm).



Figure 3.5 Hydraulic presser CARVER hydraulic unit model #3912.

In this study, we used the two sintering steps. First step, the temperature was increased from room temperature to 500°C with heating rate of 5°C/min and soaked for 1 hour. Second step, the temperature was increased to T_s (sintering temperature) with heating rate of 5°C/min and soaked for 2 hours and then cooled down to 30°C with cooling rate 5°C/min by using CARBOLITE RHF 1500 furnace in laboratory of School of Ceramic Engineering, Suranaree University of Technology, Thailand, as

seen in Figure 3.7. Figure 3.8 shows the arrangement of the powder disks before putting into the furnace for sintering process. Samples were put in an alumina crucible and were covered with alumina powder. Position of the crucible was at center of the furnace.

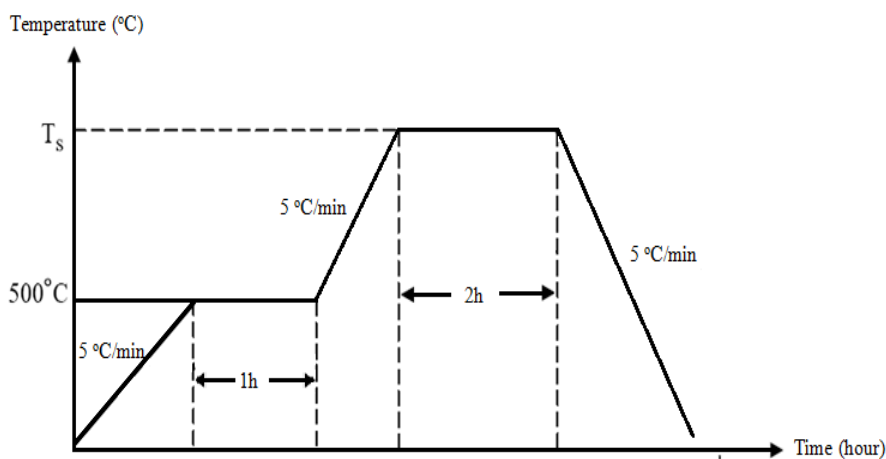


Figure 3.6 Sintering diagram of $\text{Bi}_{0.75}\text{Ba}_{0.25}(\text{Fe},\text{Ti})_{1-x}\text{Cu}_x$ or Mn_xO_3 ($x = 0, 1, 2, 3, 4$ and 5 mol%).



Figure 3.7 CARBOLITE RHF 1500 furnace.



Figure 3.8 Arrangement of samples in alumina crucible, white is alumina cover plate, red is alumina powder and black are samples.

3.4 Characterizations

3.4.1 Differential Thermal Analysis (DTA)

Differential Thermal Analysis (DTA) was used to investigate the thermal reaction of undoped $0.75\text{BiFeO}_3\text{-}0.25\text{BaTiO}_3$ powder under ambient atmosphere. The chemical reaction between undoped *BF-BT* powder and alumina as standard material was investigated over wide temperature range of 45 to 1000°C with heating/cooling rate $10^\circ\text{C}/\text{min}$. The DTA instrument is shown in Figure 3.9.



Figure 3.9 Differential Thermal Analyzer DTA7 instrument by Perkin Elmer.

3.4.2 X-ray diffraction (XRD) technique

The X-ray diffraction technique was used to analyze phase formation of powders and ceramics in $\text{Bi}_{0.75}\text{Ba}_{0.25}(\text{Fe,Ti})_{1-x}\text{Cu}_x$ or Mn_xO_3 system. Room temperature XRD patterns were recorded with a Bruker D5005 diffractometer using CuK_α radiation ($\lambda = 1.5405 \text{ \AA}$), as shown in Figure 3.10. The XRD patterns were recorded between $2\theta = 20^\circ$ to 60° at scan speed of 1 sec/step with increment 0.02.



Figure 3.10 X-ray diffractometer (Bruker D5005).

3.4.3 Particle size distribution

The relationship between packing density and particle size distribution was investigated. Particle size analyzer (HORIBA LA-950V2, Figure 3.11) was used to study on particle size distribution of the representative sample powders. The powders were first dispersed in water as media by using ultrasonic machine. Then dispersed powders were dropped into the sample holder. The results were in the form of histograms.



Figure 3.11 HORIBA Laser Scattering Particle Size Distribution Analyzer LA-950V2.

3.4.4 Relative density

The densities of all samples were determined using the Archimedes method. The sample was first weighed dry (W_1), then weighed again after fluid impregnation (W_2), and finally weighed while being immersed in fluid (W_3). The bulk density (ρ) can be calculated from the following equation:

$$\rho = \rho_w W_1 / (W_2 - W_3) \quad (3.1)$$

where ρ_w and ρ are the density of water and sample measured at room temperature, respectively.

Relative density of all compositions was computed by using the density calculated from *XRD* results, ρ_{XRD} , based on solid solution of 75% of BiFeO_3 and 25% of BaTiO_3 . The following equation was used to calculate ρ_{XRD} .

$$\rho_{XRD} = (n_A \times M_A) + (n_B \times M_B) + (n_O \times M_O) / (V \times N_A) \quad (3.2)$$

where n_A is the number of *A*-site atom per unit cell
 n_B is the number of *B*-site atom per unit cell
 n_O is the number of oxygen atom per unit cell
 M_A is the atomic mass of *A*-site atom (g/mol)
 M_B is the atomic mass of *B*-site atom (g/mol)
 M_O is the atomic mass of oxygen (g/mol)
 V is the volume per unit cell (cm³)
 N_A is Avogadro's number (6.022x10²³ mol⁻¹)

The calculated density of Cu- and Mn-doped compositions was calculated with 50% of the dopants substituted for Fe and another 50% substituted for Ti *B*-site atoms and using lattice parameter of each composition as listed in Table 3.2. The relative density, RD, of each sample was calculated with the following equation:

$$RD = \rho \times 100 / \rho_{XRD} \quad (3.3)$$

Table 3.2 Calculated lattice parameters¹ and unit cell volume of calcined powders.

Dopant	x	a (Å)	c (Å)	Volume (Å ³)
Cu	0	5.62	13.87	379.38
	1	5.62	13.82	378.02
	2	5.62	13.82	378.02
	3	5.60	13.82	375.33
	4	5.60	13.80	374.79
	5	5.60	13.73	372.89
Mn	1	5.62	13.85	378.84
	2	5.62	13.85	378.84
	3	5.60	13.82	375.33
	4	5.60	13.76	373.70
	5	5.60	13.74	373.16

¹computed in relation to the undoped sample and the standard was not used in this calculation.

However, the calculated lattice parameters are close to those of BiFeO₃ reported by Sosnowska et al.

(1996) with a and c of 5.577 and 13.861, respectively.

3.4.5 Firing shrinkage

The volume of all samples before sintered (green body), V_1 , and after sintered, V_2 , was calculated by using the following equation:

$$V = \pi r^2 d \quad (3.4)$$

where V is volume (cm^3), r is radius (cm) and d is thickness (cm) of samples.

Percent of volume shrinkage, S , was calculated by using the following equation:

$$S = (V_1 - V_2) \times 100 / V_1 \quad (3.5)$$

The steps below are the method to determine the volume shrinkage

1. Measure diameter and thickness of the green body
2. Measure diameter and thickness of the ceramics after sintered
3. Calculate volume of the samples V_1 and V_2 by using equation 3.4
4. Calculate percent of volume shrinkage, S , by using equation 3.5

3.4.6 Microstructure: Scanning Electron Microscopy (SEM)

JOEL JSM-6400 SEM, as shown in Figure 3.12, was used to determine the microstructure of ceramics. The surfaces were polished by using grinding papers number 600, 800, 1000, 1400 and 2400, respectively. The polished ceramics were cleaned with ultrasonic cleaner for 5 minutes and then dried in the oven with the temperature of 100°C for 24 hours. After that, thermal etching process was done at the temperature of 900°C for 15 minutes and heating/cooling rate is $10^\circ\text{C}/\text{min}$. The steps of microstructure investigation are as follow:

1. Stick the polished samples on brass stubs with carbon tape
2. Coat samples with gold by using ion sputtering machine, as shown in Figure 3.13, for 5 minutes
3. Investigate the microstructure by *SEM*, shown in Figure 3.11
4. Mean linear intercept method was used to investigate the average grain size of the samples



Figure 3.12 *SEM* instrument, JOEL JSM-6400.

The steps of mean linear intercept method, used to calculate average grain size of all ceramics, are shown below:

1. Randomly line on the *SEM* micrographs with length L
2. Count number of the grain intercept with the drew lines, N_L
3. Calculate with the following equation:

$$D_L = L/N_L \quad (3.6)$$

where L is the summation of length of the draw lines, N_L is number of the grain intercepts with draw lines and D_L is average grain size.



Figure 3.13 Ion sputtering machine JEOL JCF-1100E.

3.5 Electrical properties

Before electrical properties characterizations, the ceramic disks were first ground until faces were flat and parallel using a final grit paper number 1500. The polished ceramics were cleaned in an ultrasonic bath for 10 min before electroded with silver on the polished surfaces.

3.5.1 Dielectric properties

The dielectric properties of the sintered ceramics were measured 3 times of 3 samples for each composition as a function of frequency (at 1, 2, 5, 10, 20, 50 and 100 kHz) at room temperature with an automated dielectric measurement system GW Instek LCR-821 shown in Figure 3.14. The measured data were collected

as the capacitance and dielectric loss by computer controlled system. The dielectric constant was then calculated from equation:

$$\varepsilon_r = \frac{Cd}{\varepsilon_0 A} \quad (3.7)$$

where ε_r and ε_0 are the dielectric constant and permittivity of free space ($\varepsilon_0 = 8.85 \times 10^{-12}$ F/m). C is the capacitance (F), and d (m) and A (m^2) are the thickness and area of the sample, respectively.

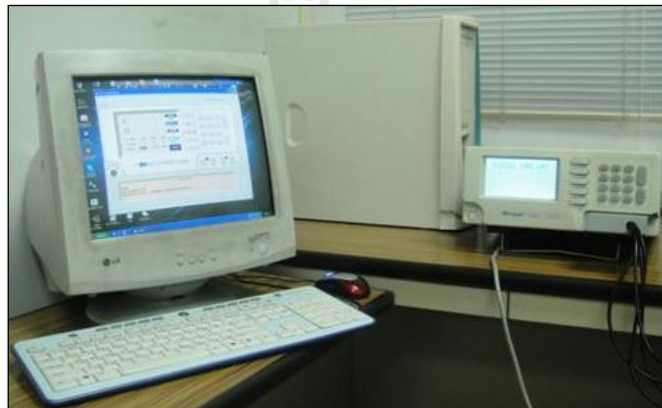


Figure 3.14 Dielectric measurements system (GW Instek LCR-821).

3.5.2 Ferroelectric properties

The room temperature ferroelectric properties were examined by a modified Sawyer–Tower circuit (Figure 3.15) at frequency of 100 Hz. The circuit was connected to high voltage power supply (TREK Model 20/20C High Voltage Amplifier), and data recording computer. The system is an automated device intended primarily for measuring the polarization of materials induced by an electric field. The optimized density samples were placed in the sample holder (brass cell) which was submerged in a silicone oil to prevent electric breakdown. Each sample was

connected to a standard capacitor on the Sawyer-Tower circuit. The sample could be considered as a capacitor (C_s) connected in series to the standard capacitor (C_o). Since the capacitance of the sample is much smaller than that of the standard capacitor, almost all of the electric potential of the high voltage source acts on the sample.

By definition, polarization is the value of dipole moment per unit volume or amount of charge accumulated per unit surface area. Polarization of the sample induced by electric field loading, P_{sample} is given by

$$P_{sample} = \frac{Q_s}{A} \quad (3.8)$$

where, P_{sample} is polarization of sample (unit, C/cm²), Q_s is the amount of charges accumulated on the electrode of the sample (unit, C), while A is the area of the electrode of the sample (unit, cm²).

Since the reference (standard) capacitor is connected in series to the sample, then amount of charges are equivalent:

$$Q_s = Q_o \quad (3.9)$$

where, Q_o is the amount of charges accumulated on the standard capacitor (unit, C).

On the other hand, the amount of charges on the standard capacitor is equal to

$$Q_o = V_y C_o \quad (3.10)$$

where, V_y is the voltage across the standard capacitor (unit, V), and $C_o = 1 \mu\text{F}$, is the capacitance of the standard capacitor.

Then the polarization induced by electric field loading could be calculated as

$$P_{\text{sample}} = \frac{V_y C_o}{A} \quad (3.11)$$

Consequently, by monitoring the voltage across the standard capacitor, the polarization of the sample could be determined.

From the X-axis of the monitor of oscilloscope, the electric field was calculated using the following equation:

$$E = \frac{V_x}{d} \quad (3.12)$$

where, E is electric field applied to sample (unit, V/cm),

V_x is the voltage across the circuit (unit, V),

d is the thickness of the sample (unit, cm).

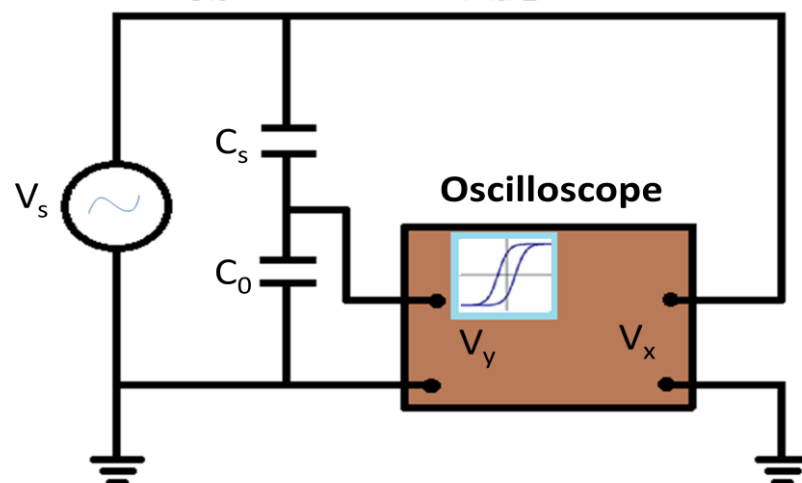


Figure 3.15 Sawyer-Tower circuit used for measuring hysteresis loop ($C_o = 0.1 \mu\text{F}$,

$C_s = \text{Sample}, C_o \gg C_s$).



Figure 3.16 TREK Model 20/20C High Voltage Amplifier.

3.5.3 Magnetic properties

The Vibrating Sample Magnetometer (VSM, LakeShore 7400 series) in which induction current is amplified by a trans-impedance amplifier and lock-in amplifier was used to investigate the magnetization field (M - H) hysteresis loops of high density samples. The various components are hooked up to a computer interface, as shown in Figure 3.17. Using controlling and monitoring software, the system can determine how much the sample is magnetized and how its magnetization depends on the strength of the constant magnetic field, hence M - H loops can be obtained.

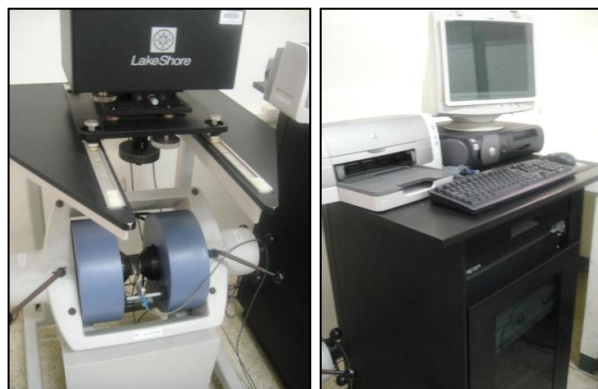


Figure 3.17 VSM components setup for magnetic measurement (LakeShore 7400 series).

3.5.4 X-ray Absorption Spectroscopy at SLRI, Thailand

X-ray Absorption Spectroscopy (XAS) technique in X-ray Absorption Near Edge Structure (XANES) region at Synchrotron Light Research Institute (Public Organization) (SLRI) was used to investigate the local structure within ceramic samples.

XANES spectra were recorded with the measurement at Ba, Bi, Ti, Fe, Mn and Cu edges under condition of:

Photon Energy Scan (eV)	=	-30,80
Photon Energy Step (eV)	=	0.2
Time Step (s)	=	1-5 (depend on output signal)

The edge, edge-energy, crystal and standards, and gas types used for the measurements are shown in Tables 3.3 and 3.4. All ceramic samples were investigated by fluorescence mode with 13-component germanium detector.

Table 3.3 The edge, edge-energy, crystal and standard of all elements.

Element	Edge	Edge-energy	Crystal	Standard	Calibrator
Ba	L_3	5247	Ge(220)	-	Ti foil
Bi	M_5	2580	Si(111)	-	FeSO ₄ powder
Ti	K	4966	Ge(220)	BaTiO ₃ single crystal	Ti foil
Fe	K	7112	Ge(220)	Fe ₂ O ₃ and FeO	Fe foil

Table 3.3 The edge, edge-energy, crystal and standard of all elements (Continued).

Element	Edge	Edge-energy	Crystal	Standard	Calibrator
Mn	<i>K</i>	6539	Ge(220)	MnO ₂ , MnO and Mn ₂ O ₃	Mn foil
Cu	<i>K</i>	8979	Ge(220)	Cu ₂ O and CuO	Cu foil

Table 3.4 Gas type and Gas pressure.

K-edge	<i>L</i> ₃ edge	<i>M</i> ₅ edge	10-cm long ion chamber (<i>I</i> ₀)	40-cm long ion chamber (<i>I</i> ₁)
		Bi	37 mbar N ₂	200 mbar N ₂
Ti	Ba		15 mbar Ar	80 mbar Ar
Mn			31 mbar Ar	170 mbar Ar
Fe			39 mbar Ar	214 mbar Ar
Cu			76 mbar Ar	413 mbar Ar

CHAPTER IV

RESULTS AND DISCUSSION

This chapter contains the results of $\text{Bi}_{0.75}\text{Ba}_{0.25}(\text{Fe},\text{Ti})_{1-x}\text{Cu}_x\text{O}_3$ and $\text{Bi}_{0.75}\text{Ba}_{0.25}(\text{Fe},\text{Ti})_{1-x}\text{Mn}_x\text{O}_3$ ($x = 0, 0.01, 0.02, 0.03, 0.04$ and 0.05) samples in both calcined powders and sintered ceramics. The relationships between calcination and sintering conditions, phase formation, physical properties, dielectric, ferroelectric and magnetic properties of all samples are described. The multiferroic properties are also investigated through magnetoelectric coefficient. Finally, XAS measurement in XANES region is used to identify oxidation number and position of the absorber atom measured at Fe, Ti, Cu, Mn, Ba and Bi edges are also reported and discussed.

4.1 Differential Thermal Analysis (DTA)

The differential thermal analysis (DTA) result of undoped $0.75\text{BF}-0.25\text{BT}$ powder is shown in Figure 4.1. There is only single endothermic reaction can be observed and the half endothermic reaction is located at temperature of 768°C . This temperature is expected to be the starting formation temperature of $0.75\text{BF}-0.25\text{BT}$. In addition, our previous work (Chandarak, 2008) which studied on $(1-x)\text{BF}-(x)\text{BT}$ system found that single phase perovskite could be obtained for all compositions when the powders were calcined at temperature of 900°C with heating/cooling rates of $5^\circ\text{C}/\text{min}$. Therefore, the same calcination condition has been chosen for this work. As seen in Figure 4.1, at temperature of 900°C , there is no further reaction which indicated that $0.75\text{BF}-0.25\text{BT}$ system is completely formed.

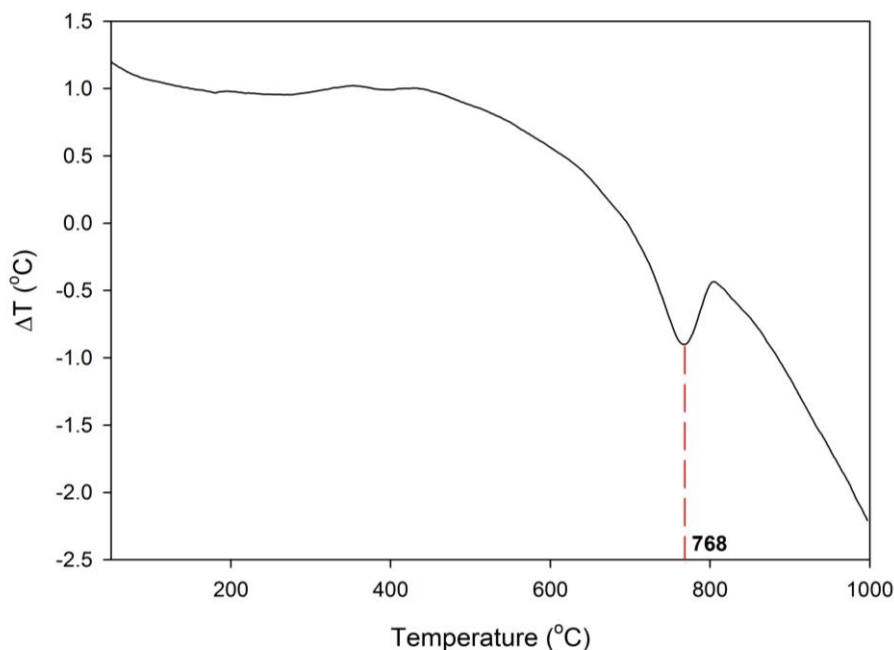


Figure 4.1 DTA curve of undoped 0.75BF-0.25BT powder.

4.2 Phase formation by X-ray diffraction (XRD)

4.2.1 Calcined powders

XRD patterns of all calcined powders (calcined at 900°C) are shown in Figure 4.2. Undoped 0.75BF-0.25BT sample shows single phase perovskite structure and the XRD pattern is consistent with the previous studies (Itoh et al., 2007; Chandarak, 2008; Xiao-Hui et al., 2008; Chandarak et al., 2009).

The undoped 0.75BF-0.25BT sample still shows splitting peaks (2θ ~38-40 and 56-58) as distorted rhombohedral structure (Kumar et al., 2000; Itoh et al., 2007). When more Cu and Mn contents were added in 0.75BF-0.25BT system the changing in XRD patterns indicating that the structure trend to be lower distorted rhombohedral structure. These results confirm that single phase perovskite of undoped 0.75BF-0.25BT and Cu- and Mn-doped samples can be obtained by using the

chosen calcination condition.

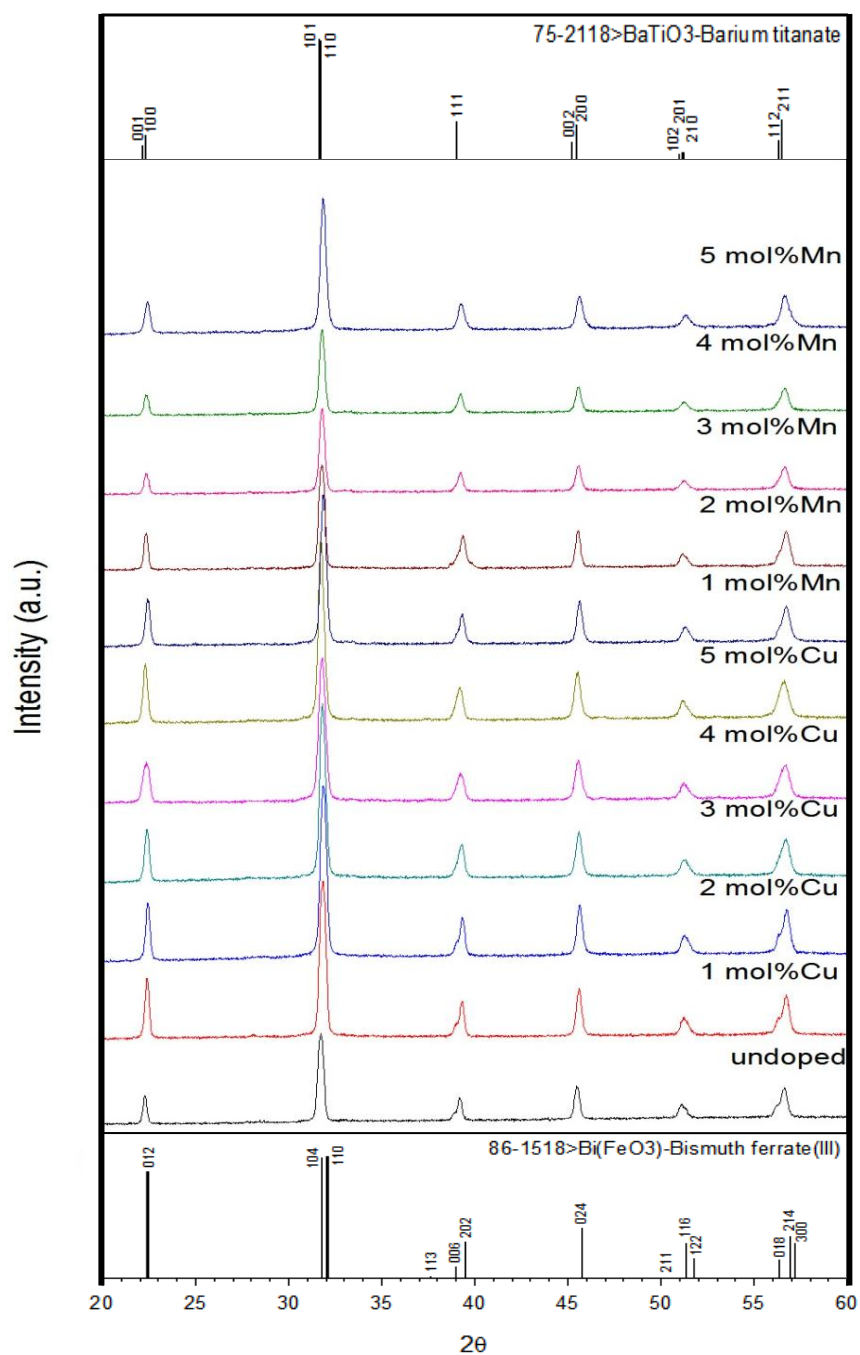


Figure 4.2 XRD patterns of $\text{Bi}_{0.75}\text{Ba}_{0.25}(\text{Fe},\text{Ti})_{1-x}\text{Cu}_x$ or Mn_xO_3 with $x = 0, 1, 2, 3, 4$ and 5 mol% calcined at 900°C .

4.2.2 Sintered ceramics

High resolution *XRD* was employed to investigate the phase formation behavior in the sintered ceramics. The highest relative density of undoped 0.75*BF*-0.25*BT* (< 90%) and high relative density of Cu- and Mn-doped (> 90%) samples were chosen for this investigation. The *XRD* results show single phase perovskite without secondary phase in all sintered samples (as shown in Figure 4.3).

XRD pattern of undoped 0.75*BF*-0.25*BT* still shows typical distorted rhombohedral structure as observed in calcined powder. While Cu- and Mn-doped ceramics show more structural symmetry (Figures 4.3(b) and (c)) similar to previous study by Leontsev and Eitel (2009) which found that in 0.5 mol% Mn-doped 0.75*BF*-0.25*BT* and 0.67*BF*-0.33*BT* there was no characteristic splitting associated with the deviation from cubic symmetry possibly because of extremely small rhombohedral distortion. Moreover, the different in *XRD* patterns of doped samples could not be observed, possibly, they have the same structure. These results indicate that this sintering condition is suitable to prepare high purity samples of undoped 0.75*BF*-0.25*BT* and Cu- and Mn-doped ceramics.

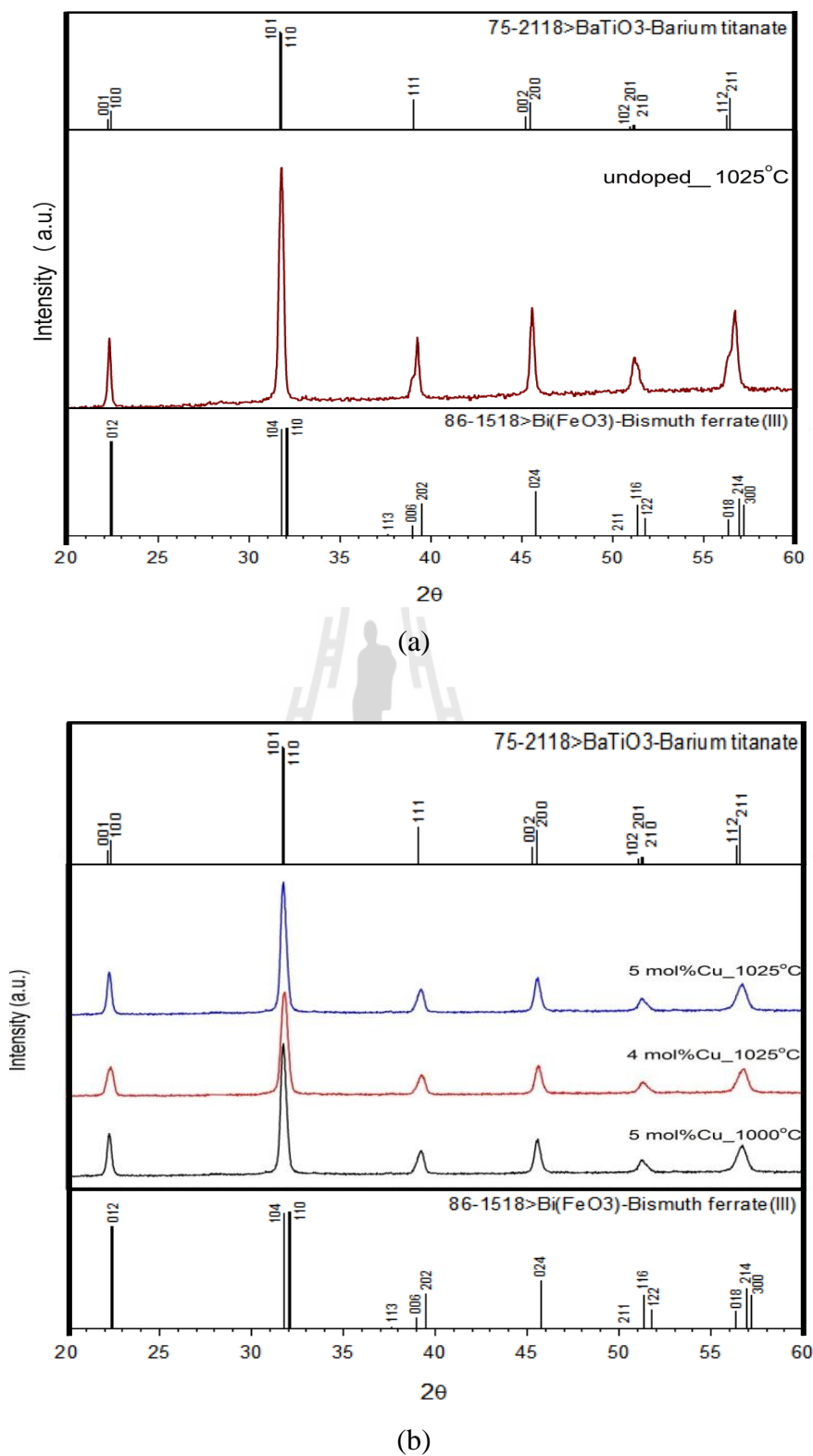


Figure 4.3 XRD patterns of high density samples (a) undoped, (b) Cu and (c) Mn doped 0.75BF-0.25BT ceramics.

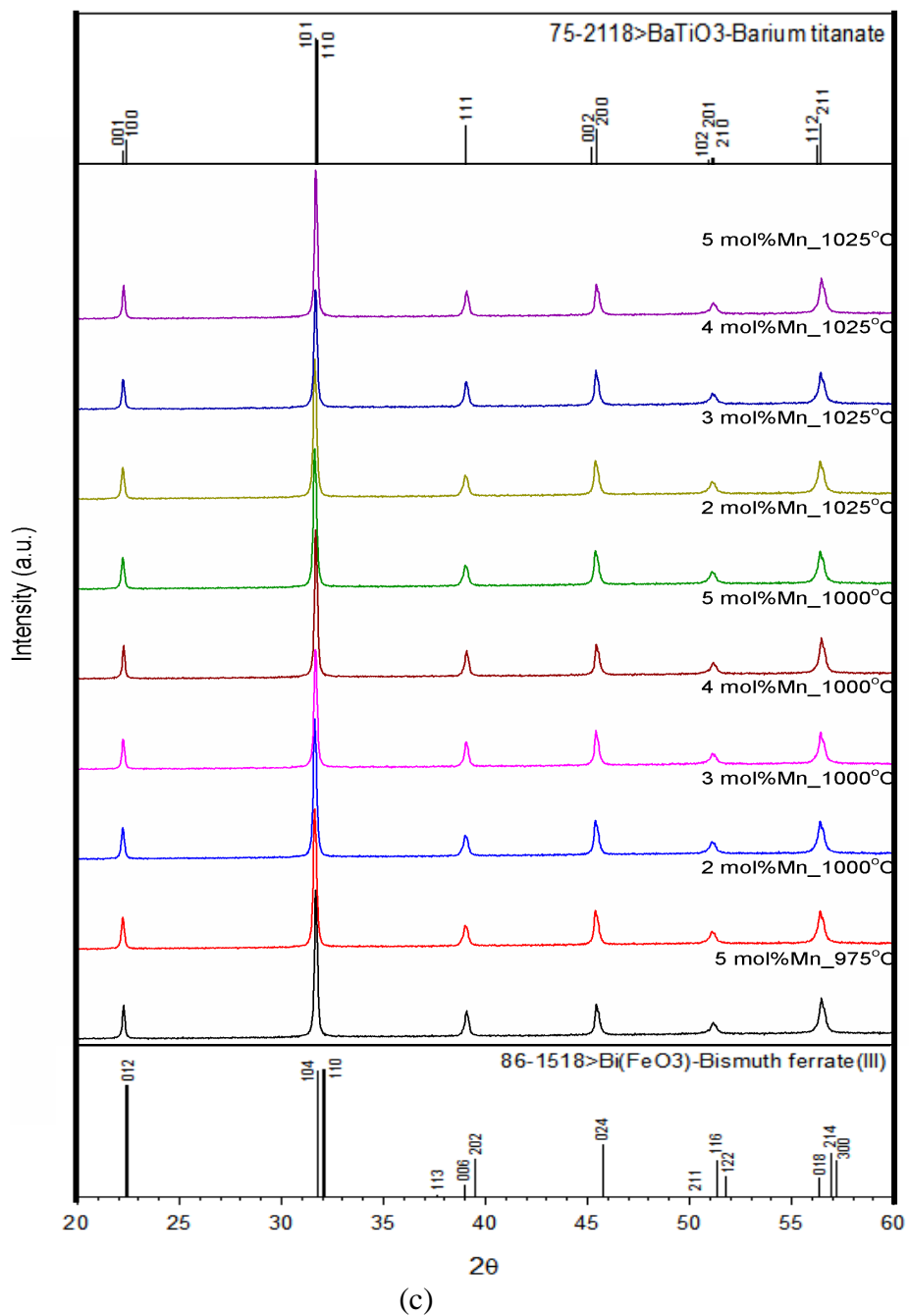


Figure 4.3 XRD patterns of high density samples (a) undoped, (b) Cu and (c) Mn doped $0.75BF-0.25BT$ ceramics (Continued).

4.3 Density

4.3.1 Particle size distribution and packing density of green body

All powders were mixed with a drop of aqueous PVA binder (0.04 grams) for 1 gram of each sample powder. The packing density of all disk samples was observed by measuring after the samples were pressed. The results as listed in Table 4.1 show that there is variation of packing density (in range of 5.23-5.48 g/cm³) because practical filling densities are lower than theoretical random packing, as not all particles reach the optimal position during the filling process (Oberacke, 2012).

Table 4.1 Packing density of all compositions measured after pressed.

Composition		Packing density (g/cm ³)
0.75BF-0.25BT	0	5.34 ± 0.09
Cu	1	5.39 ± 0.18
	2	5.43 ± 0.12
	3	5.48 ± 0.06
	4	5.26 ± 0.12
	5	5.40 ± 0.15
Mn	1	5.24 ± 0.10
	2	5.23 ± 0.21
	3	5.29 ± 0.12
	4	5.27 ± 0.10

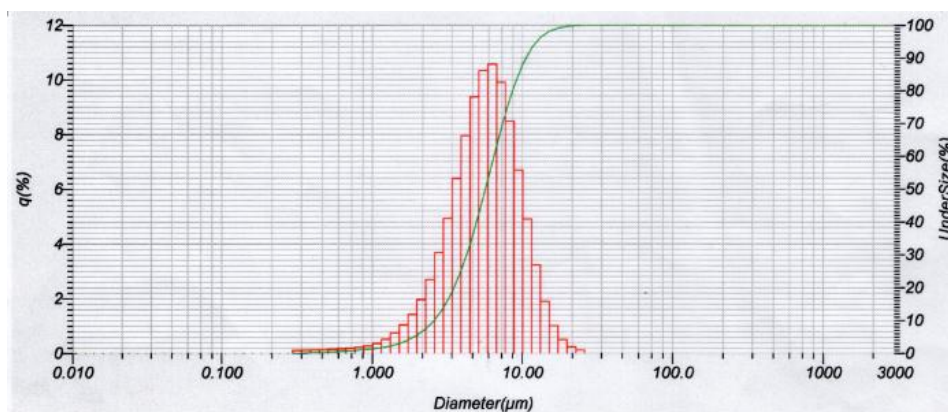
Table 4.1 Packing density of all compositions measured after pressed (Continued).

Composition		Packing density (g/cm ³)
Mn	5	5.30 ± 0.09

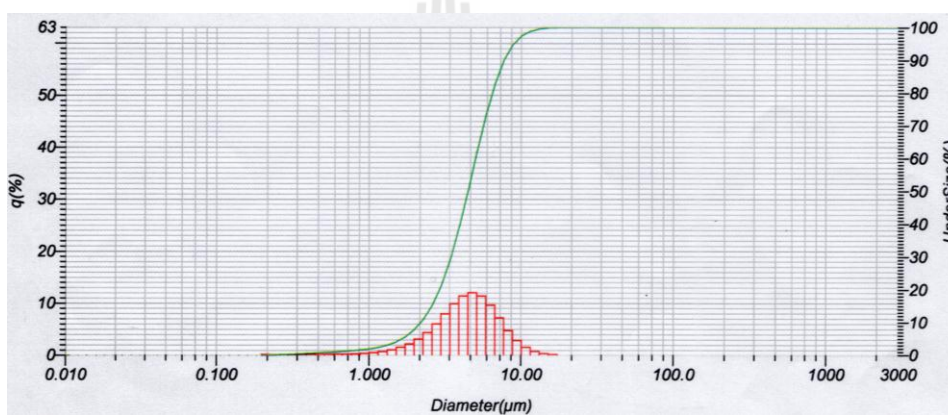
The histogram of particle size distribution of selected compositions is shown and listed in Figure 4.4 and Table 4.2. Mn-doped sample shows the largest mean size (8.53 μm) and the particle size distribution is broad. Cu-doped sample shows the smallest particle size (4.78 μm) with narrow particle size distribution. The particle size and particle size distribution of undoped 0.75BF-0.25BT vary between those of Cu- and Mn-doped samples.

Table 4.2 Particle size distribution parameters.

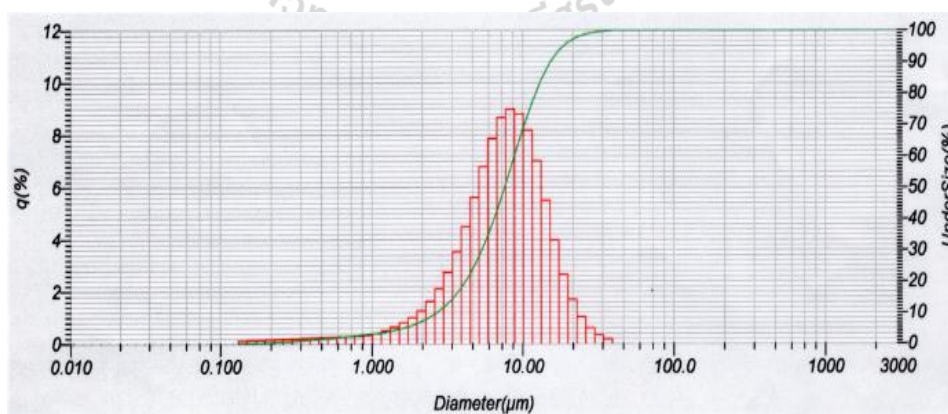
Parameter	undoped	3 mol%Cu	3 mol%Mn
Mean size	6.24	4.78	8.53
Standard Deviation	3.33	2.28	5.39



(a)



(b)



(c)

Figure 4.4 Particle size distribution of (a) undoped, (b) 3 mol% Cu and (c) 3 mol% Mn doped 0.75BF-0.25BT calcined powders.

To investigate shape of the powder particles, *SEM* micrographs of the selected compositions were observed, shown in Figure 4.5. The results show that in Cu doped 0.75BF-0.25BT sample, the powder particles are very fine ($\sim 1 \mu\text{m}$) but they agglomerate to form larger particles ($\sim 5\text{-}10 \mu\text{m}$). While Mn doped 0.75BF-0.25BT powder particles show coarse particles and a little bit agglomeration were observed. On the other hand, agglomeration was observed in undoped 0.75BF-0.25BT sample.

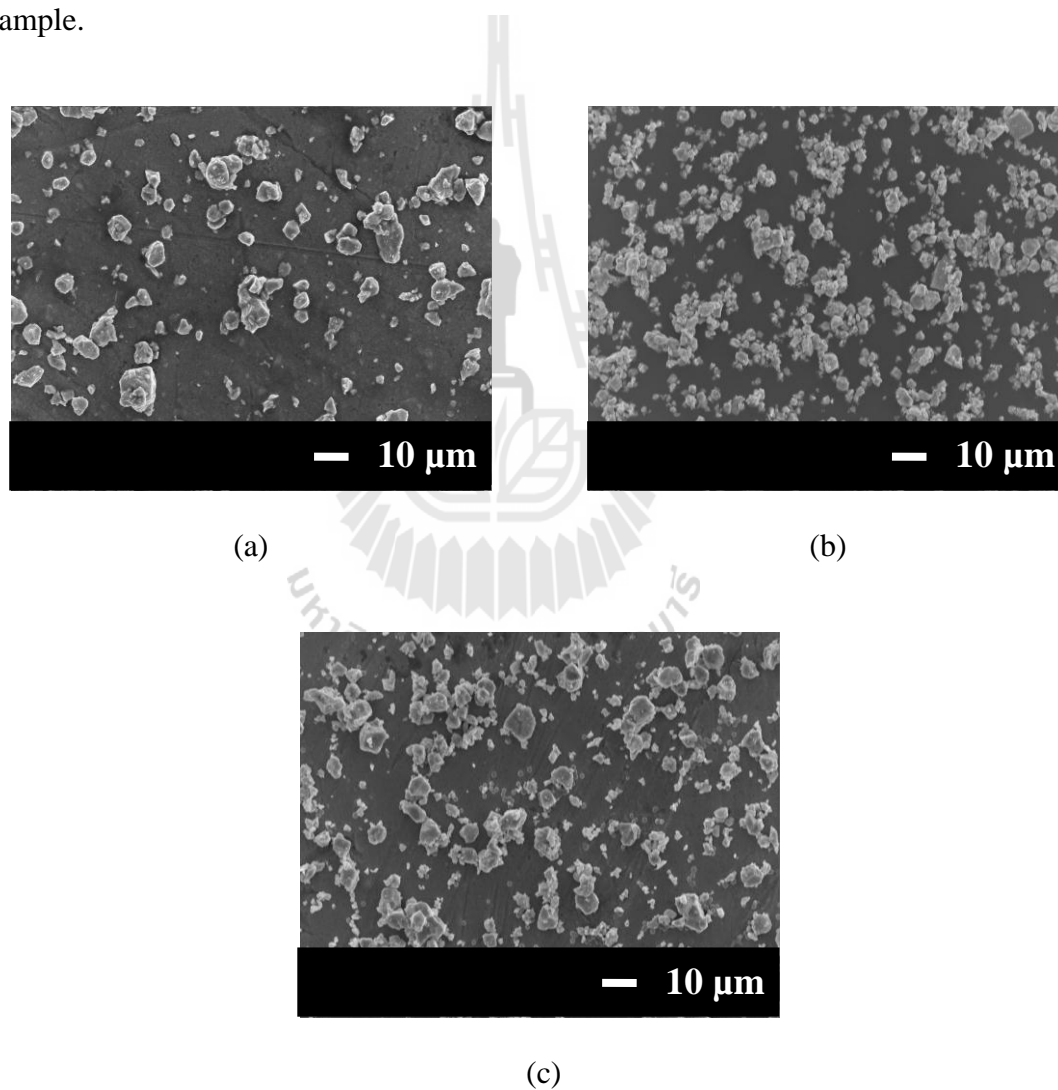
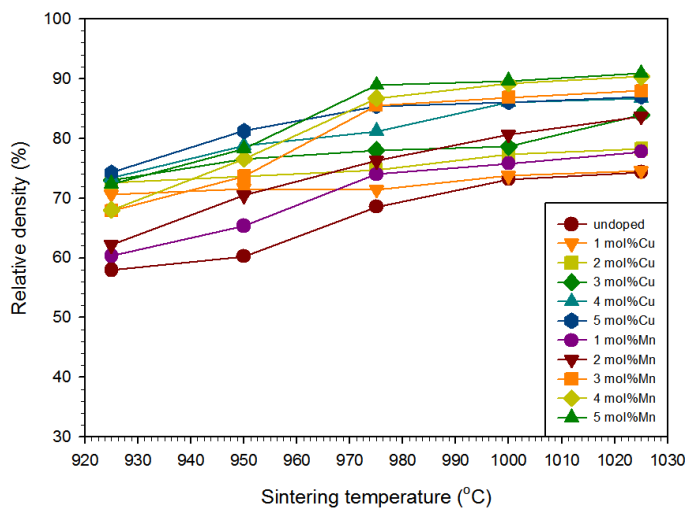


Figure 4.5 *SEM* micrographs of (a) undoped, (b) 3 mol%Cu, and (c) 3 mol%Mn doped 0.75BF-0.25BT calcined powders.

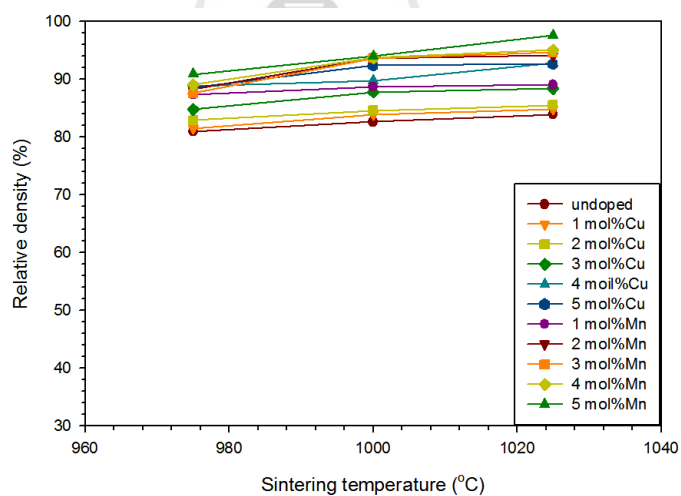
4.3.2 Relative density

The Archimedes method was used to obtain bulk density of all samples for calculating relative density. It was found that only 3 ceramics, 5 mol%Mn doped sample sintered at 1000, and 4 and 5 mol%Mn doped sample sintered at 1025°C, show high relative density as required in the objective of this work, Figure 4.6(a). This result may be due to powder compaction process. The powder compaction is simply the processing of a free flowing powder. The powder may be dry pressing (i.e., without the addition of the binder) or pressed with the addition of a small amount of suitable binder (Carter and Norton, 2007). Binder is a component that is added to hold the powder together in pressing process. The binder provides the dry (green) shape with strength sufficient to survive the handling process between shaping and sintering. One of the most important requirements for the binder is that it must be able to be eliminated from the compact during the firing process without any disruptive effect. For the pressing process, the suitable amount of binder is between 0 and 5 wt% of a binder (Carter and Norton, 2007). However, in this work, two drops of aqueous *PVA* of about 0.08 grams weight were first mixed with 1 gram of sample powder. This amount of aqueous *PVA* is about 8% by weight of the sample powder which is relatively high proportion regard to the suitable amount of binder described above. As well known, binder is absorbed and acts as a bridge between powder particles provide a binding action (Das, 2011). Hence, more amount of aqueous *PVA* causes a longer bridge which is more powder particles separation. Therefore, in the debinding process, binder was burnt out and leaved voids or pores. When the temperature was increased to sintering temperature, the pores are sealed off and the material behaves like a solid with isolated pores (Riedel and Chen, 2012). Thus more aqueous *PVA*, as

described above, affected high porosity in debinding process and then caused low density sample.



(a)



(b)

Figure 4.6 Relative density of (a) $\text{Bi}_{0.75}\text{Ba}_{0.25}(\text{Fe},\text{Ti})_{1-x}\text{Cu}_x$ or Mn_xO_3 ceramics at $x = 0, 1, 2, 3, 4$ and 5 mol% with (a) aqueous *PVA* 2 drops and (b) aqueous *PVA* 1 drop per gram of sample powders for pressing process.

Table 4.3 Relative density of all high density samples.

Composition	T_s (°C)	Relative density (%)
5 mol%Mn	975	90.86
5 mol%Cu	1000	92.34
2 mol%Mn		93.61
3 mol%Mn		93.63
4 mol%Mn		93.71
5 mol%Mn		93.93
4 mol%Cu		1025
5 mol%Cu	92.62	
2 mol%Mn	94.07	
3 mol%Mn	94.63	
4 mol%Mn	95.04	
5 mol%Mn	97.52	

To improve bulk density of the samples, the reduction of aqueous *PVA* to one drop which is about 0.04 grams (4 wt% compared with weight of sample powder) was used. As seen in Figure 4.6(b) and listed in Table 4.3, this reduction of aqueous *PVA* can increase the relative density up to 90-98% of the ceramic samples.

4.4 Firing shrinkage

The firing shrinkage of the samples is plotted in Figures 4.7 and 4.8. The sintering temperature affected to the volume shrinkage behavior noticeably. The volume shrinkage is increase with increasing sintering temperature. In addition, adding more amount of dopants also increase the firing shrinkage. This result associated with the density of the sample. The firing shrinkage of all samples mixed with 2 drops (0.08 grams) aqueous *PVA* per gram of sample powders is shown in Appendix A.

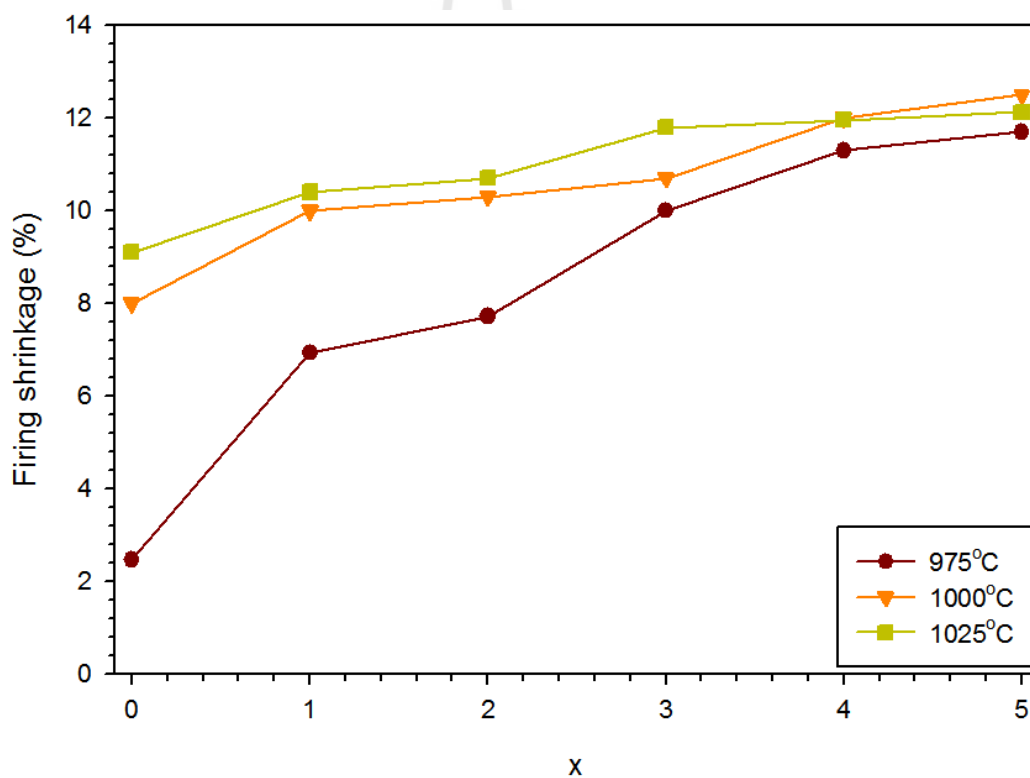


Figure 4.7 Firing shrinkage of $\text{Bi}_{0.75}\text{Ba}_{0.25}(\text{Fe},\text{Ti})_{1-x}\text{Cu}_x\text{O}_3$ ceramics at $x = 0, 1, 2, 3, 4$ and 5 mol% with 1 drop (0.04 grams) aqueous *PVA* per gram of sample powders for pressing process.

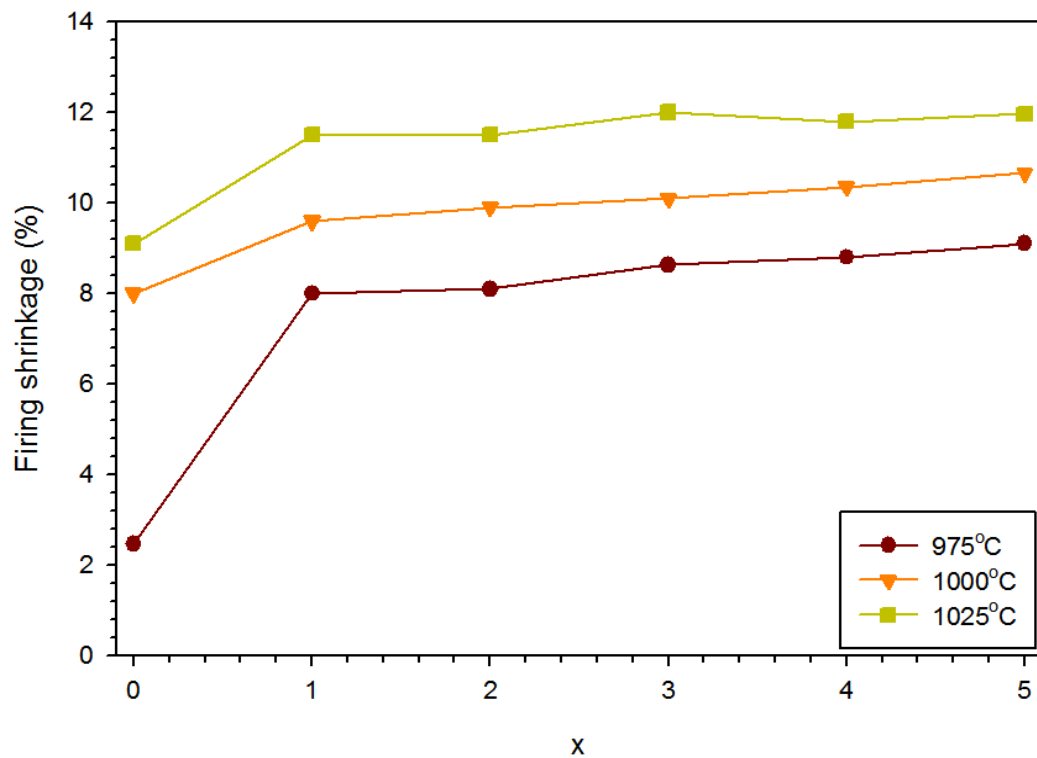
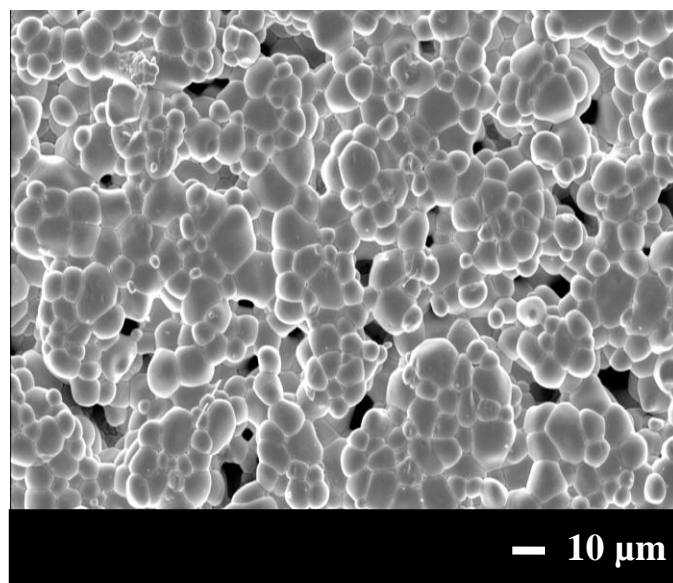


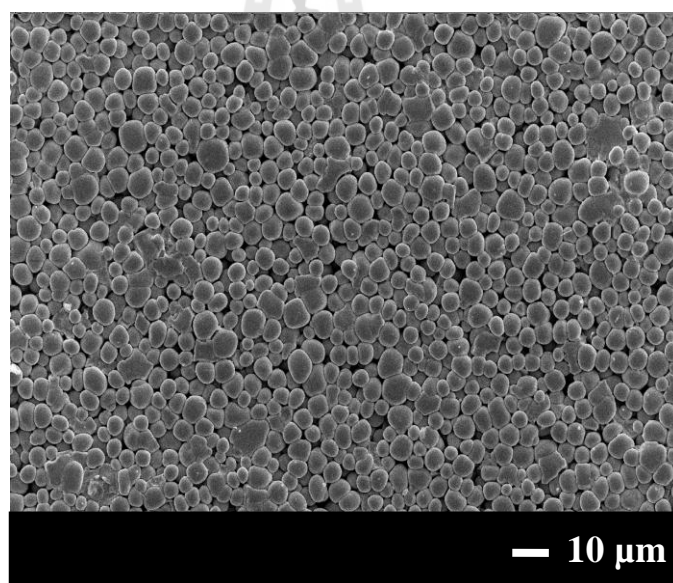
Figure 4.8 Firing shrinkage of $\text{Bi}_{0.75}\text{Ba}_{0.25}(\text{Fe},\text{Ti})_{1-x}\text{Mn}_x\text{O}_3$ ceramics at $x = 0, 1, 2, 3, 4$ and 5 mol% with with 1 drop (0.04 grams) aqueous *PVA* per gram of sample powders for pressing process.

4.5 Microstructure by Scanning Electron Microscope (*SEM*)

Figure 4.9 shows microstructures of all high density ceramic samples sintered at 1025°C . The undoped $0.75\text{BF}-0.25\text{BT}$ sample shows high porosity which results to low density of the sample. While Cu- and Mn-doped samples show lower porosity and thus high density sample can be obtained.



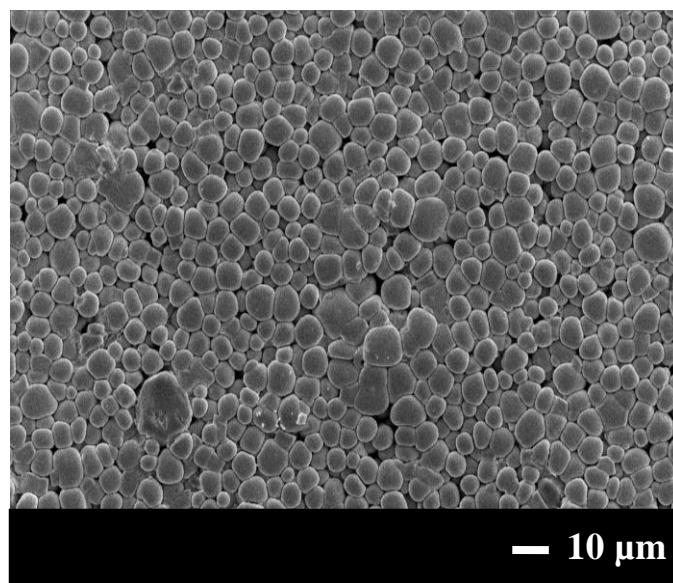
(a)



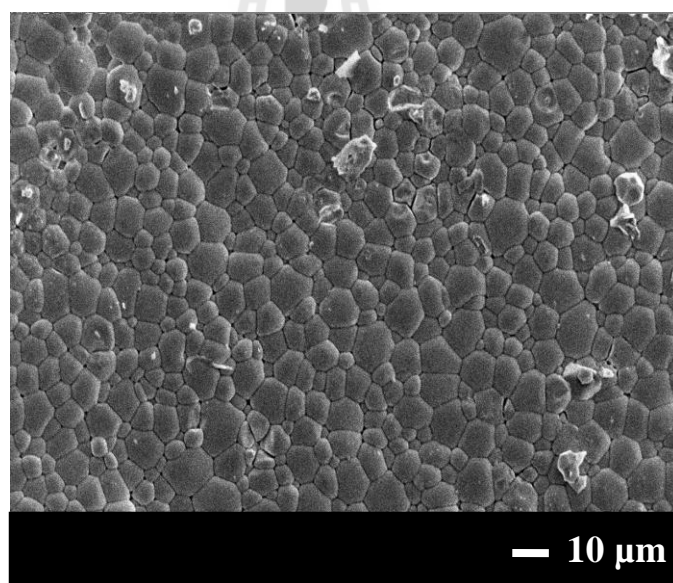
(b)

Figure 4.9 SEM micrographs of high density samples sintered at 1025°C.

- | | |
|--------------|--------------|
| (a) undoped | (e) 3 mol%Mn |
| (b) 4 mol%Cu | (f) 4 mol%Mn |
| (c) 5 mol%Cu | (g) 5 mol%Mn |
| (d) 2 mol%Mn | |

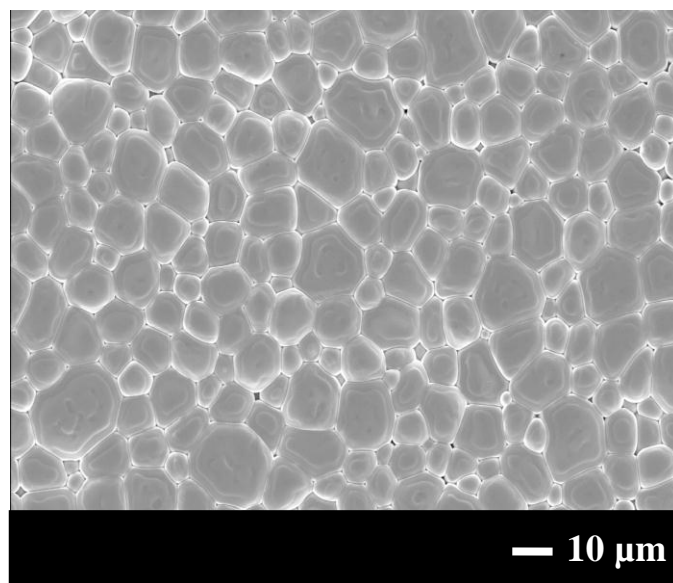


(c)

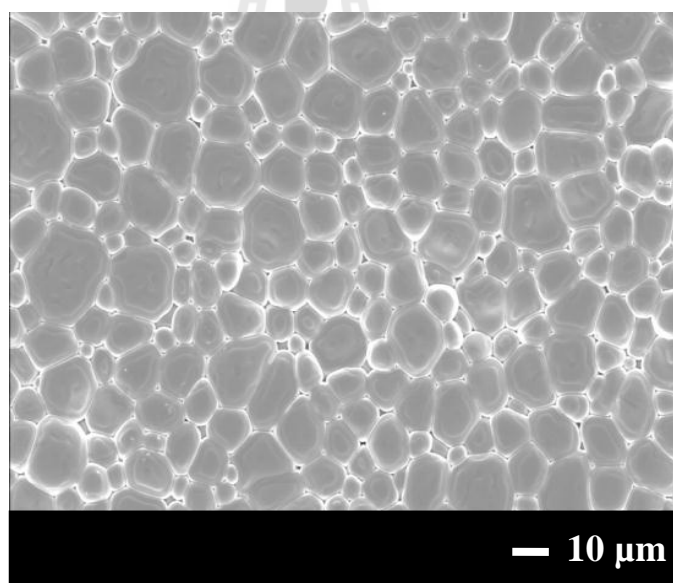


(d)

Figure 4.9 SEM micrographs of high density samples sintered at 1025°C
(Continued).

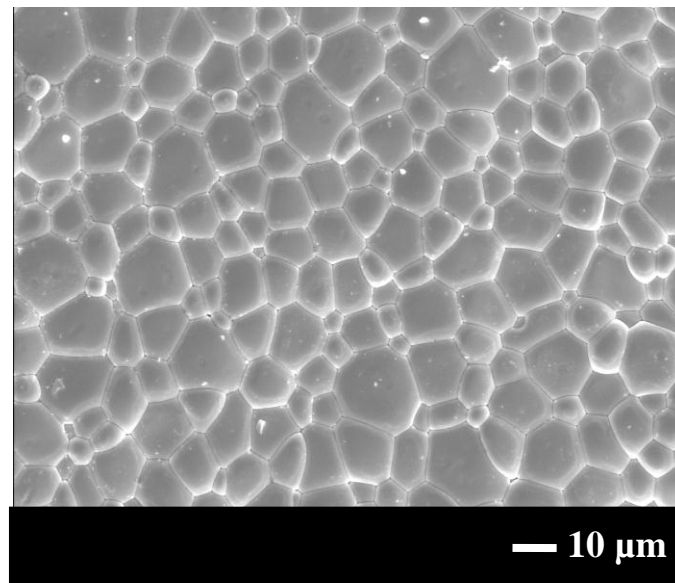


(e)



(f)

Figure 4.9 SEM micrographs of high density samples sintered at 1025°C
(Continued).



(g)

Figure 4.9 SEM micrographs of high density samples sintered at 1025°C

(Continued).

The average grain sizes of undoped, Cu and Mn doped 0.75BF-0.25BT samples were determined by the linear intercept method as listed in Table 4.4. It was found that Cu and Mn contents affect to the average grain size and the average grain size increased with increasing amount of Cu and Mn. The largest average grain sizes can be observed in 5 mol%Cu- and 5 mol%Mn-doped samples with 5.74 μm and 9.22 μm, respectively. The Cu-doped samples show higher porosity than the Mn-doped samples which caused by the agglomeration and narrow particle size distribution as shown in Figure 4.5(b). On the other hand, Mn-doped samples show lesser porosity than undoped 0.75BF-0.25BT and Cu-doped samples. This cause of Mn behaves like a flux likes as found by Xiao-Hui et al., 2008, which in turn increases the density and sintering ability of the solid solution.

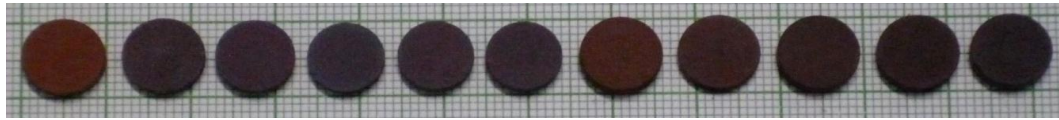
Table 4.4 Average grain sizes of all samples sintered at 1025°C.

Sample	Grain size (μm)
undoped	6.19
4 mol%Cu	5.04
5 mol%Cu	5.74
2 mol%Mn	6.57
3 mol%Mn	8.90
4 mol%Mn	9.00
5 mol%Mn	9.22

4.6 Physical appearance

Physical appearances of the samples are also interested as seen in Figure 4.10, size of the samples are associated with the trend of density and volume shrinkage. As described previously, the particles of Cu-doped powders are agglomerated which lead to decreasing of total surface area of the samples and caused thicker binder layer covered on the surface. This thick layer increased the distance between the agglomerated powder particles. When the samples were sintered, this thick layer was burnt out and leaved such large pore. Then the particles that stayed surround the pores moved closer to the neighboring particles and result to the decreasing of the overall size as can be seen in the high firing shrinkage samples. While Mn-doped samples show a very little effect to firing shrinkage. The sintering temperature affects to firing

shrinkage of all samples. Firing shrinkage increases with increasing of the sintering temperature.



(a)



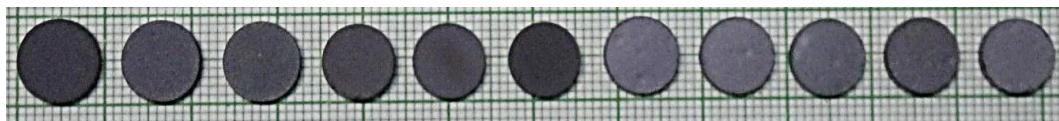
(b)



(c)



(d)



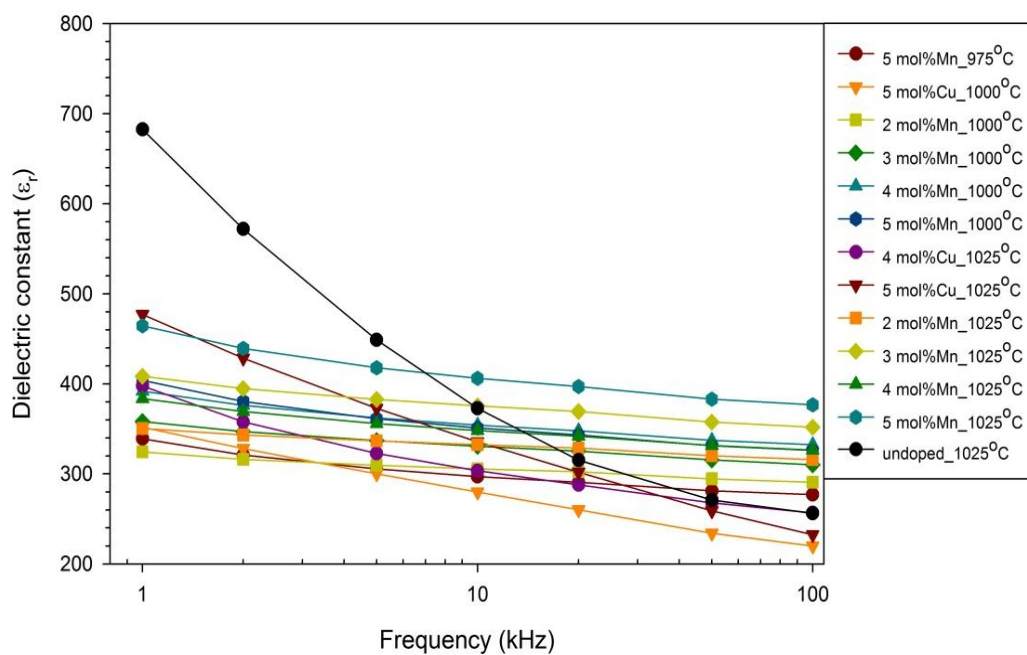
(e)

Figure 4.10 Photographs of $\text{Bi}_{0.75}\text{Ba}_{0.25}(\text{Fe},\text{Ti})_{1-x}\text{Cu}_x\text{O}_3$ and $\text{Bi}_{0.75}\text{Ba}_{0.25}(\text{Fe},\text{Ti})_{1-x}\text{Mn}_x\text{O}_3$ sintered at (a) 925°C, (b) 950°C, (c) 975°C, (d) 1000°C and (e) 1025°C (undoped, 1-5 mol%Cu and Mn doped 0.75BF-0.25BT samples, from left to right) mixed with 1 drop of aqueous PVA.

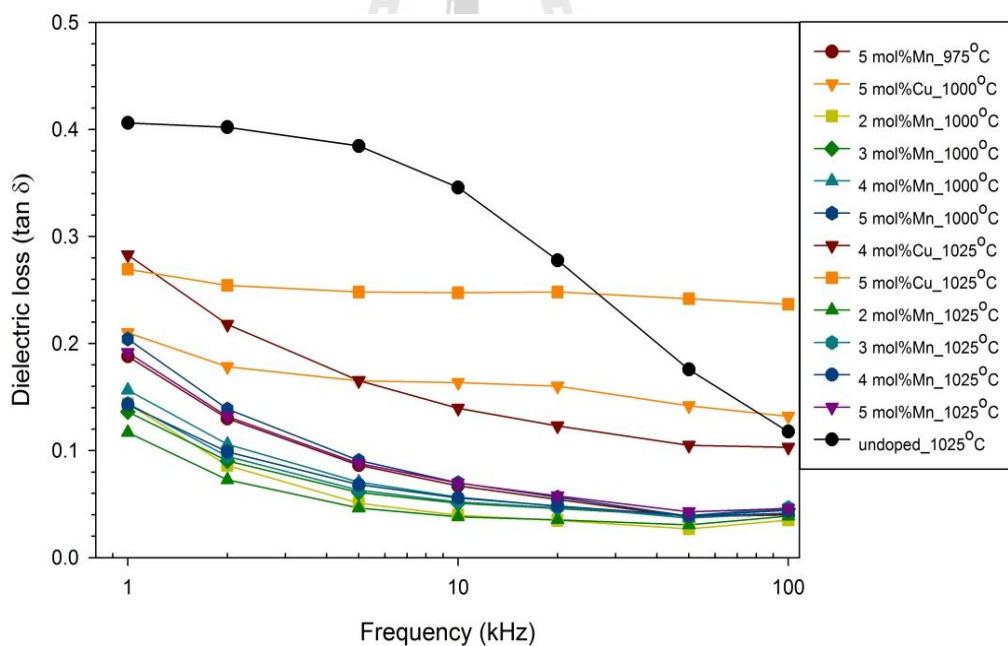
4.7 Electrical properties

4.7.1 Dielectric properties

In this work, the changing of dielectric properties mainly depends on 2 factors, oxygen vacancy and space charge polarization which involve a limited transport of charge carriers until they are stopped at the potential barrier, possibly porosity (Moulson and Herbert, 2003; Li et al., 2008). As well known, the effect of charge compensation of Fe^{2+} and Fe^{3+} in BiFeO_3 resulting to oxygen vacancy creation lead to low resistivity and high frequency dependence on dielectric properties of BiFeO_3 (Mazumder and Sen, 2009; Eerenstein et al., 2005; Pabst et al., 2007; Gu et al., 2010). However, in this work, the strong frequency dependence and high dielectric loss not relate to charge compensation effect of Fe^{2+} and Fe^{3+} according to absence of Fe^{2+} as seen in XAS section. Nevertheless, oxygen vacancy still exists in the doped samples with the other source of oxygen vacancy creation, in this work, is charge compensation of the dopants (Cu^{3+} and Mn^{3+}) substitute for Ti^{4+} . Therefore, frequency dependence on dielectric properties is still observed. On the other hand, as described above, appearance of porosity in all samples also affect to frequency dependence on dielectric properties. As seen in Figures 4.9 and 4.11, samples that show high porosity also show high frequency dependence of dielectric properties as a result of space charge effect (Moulson and Herbert, 2003; Li et al., 2008).



(a)



(b)

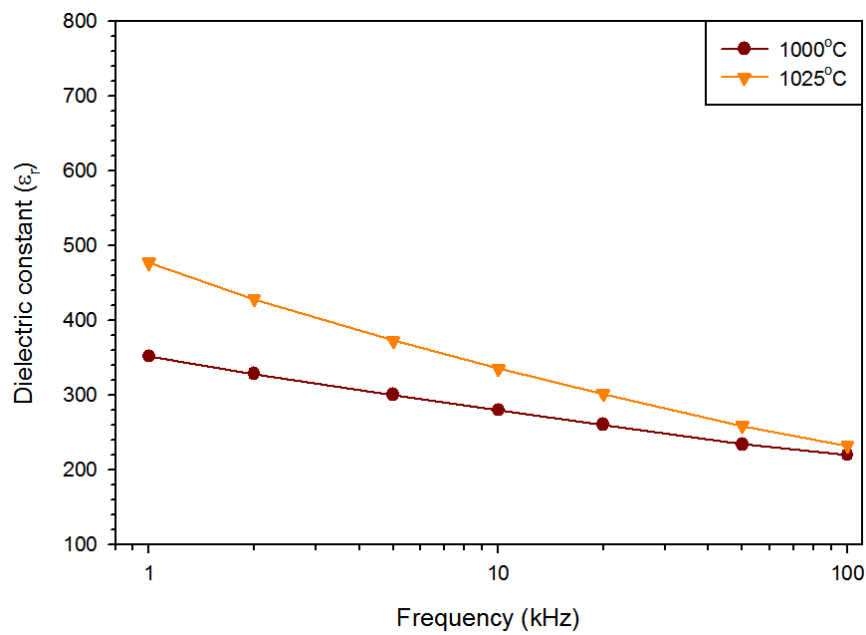
Figure 4.11 Frequency dependent dielectric properties of $\text{Bi}_{0.75}\text{Ba}_{0.25}(\text{Fe},\text{Ti})_{1-x}\text{Cu}_x\text{O}_3$ or $\text{Bi}_{0.75}\text{Ba}_{0.25}(\text{Fe},\text{Ti})_{1-x}\text{Mn}_x\text{O}_3$ samples (a) dielectric constant and (b) dielectric loss (measured at 25°C).

1. Effect of sintering temperature

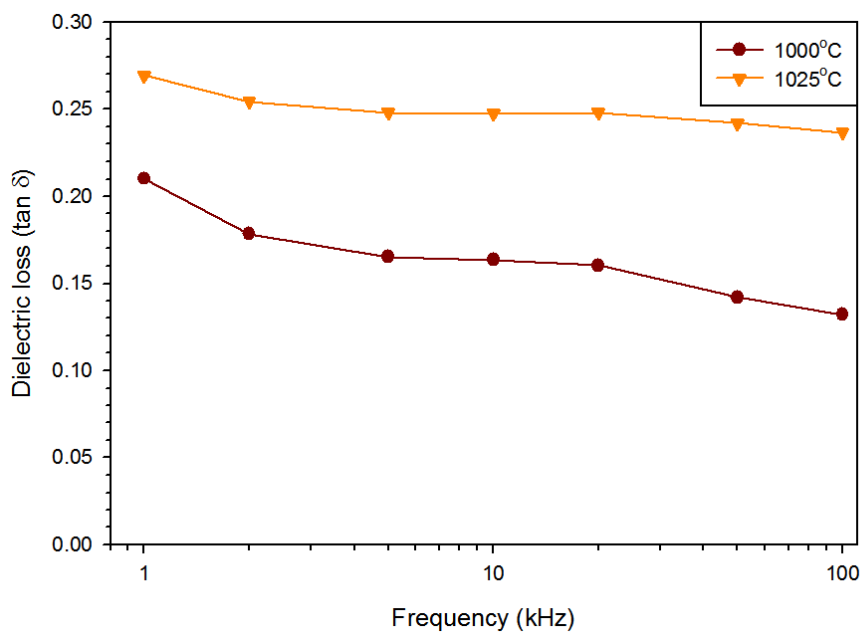
1.1 Cu-doped samples

This section, the effect of sintering temperature on dielectric properties of each high density composition will be described.

Figure 4.12 shows the effect of sintering temperature on dielectric properties of 5 mol% Cu-doped sample sintered at 1000 and 1025°C. As described previously, porosity and oxygen vacancy affect to frequency dependence on dielectric properties in this work, however, due to the samples have the same density so the effect of porosity should not be concerned. Therefore, frequency dependence on dielectric properties depends only on oxygen vacancy, which caused by higher sintering temperature. As reported by Ciomaga et al. (2011), in sintering process, the fast cooling from the sintering temperature down to the room temperature does not allow a homogeneous reoxidation of the overall ceramic grain. Therefore, the concentration of oxygen vacancies is different in the regions of grain bulk and grain boundaries, giving the idea that the ceramics consists by an oxidized insulating grain boundary region and an oxygen-deficient semiconducting grain core. Hence, this giving rise to grain boundary related phenomena which play a major role in dielectric relaxation and high dielectric loss also caused by the same effect.



(a)



(b)

Figure 4.12 Dielectric properties (a) dielectric constant and (b) dielectric loss of 5 mol%Cu doped 0.75BF-0.25BT ceramics sintered at various temperatures.

1.2 Mn-doped samples

Figures 4.13 and 4.14 show dielectric properties of Mn-doped samples sintered at various temperature. The results show enhancing of dielectric constant when sintered at higher temperature. Increasing of dielectric constant should be caused by higher density of the sample. While dielectric loss of these samples still show the same value.

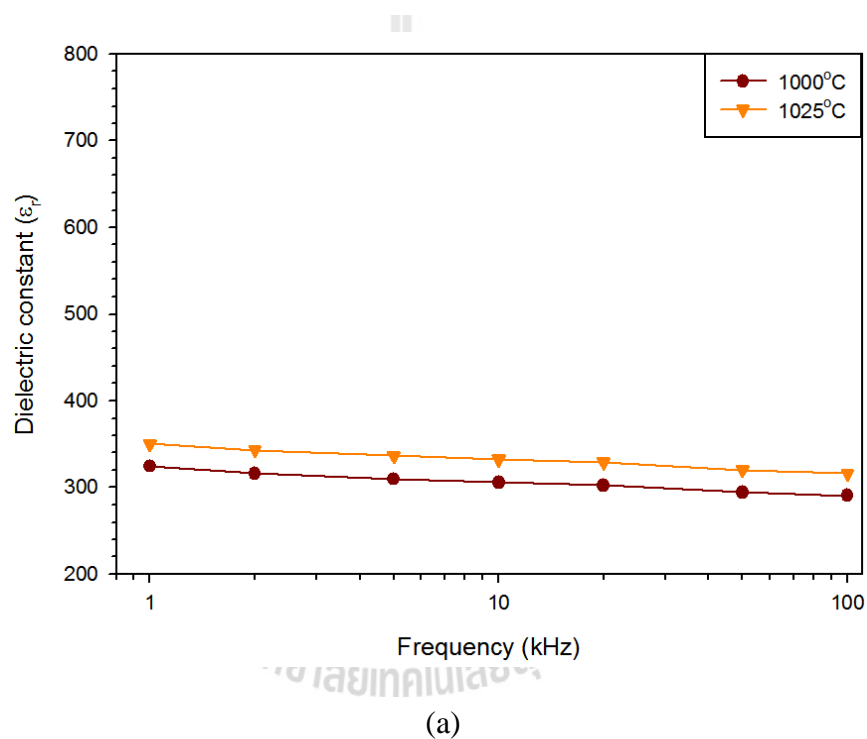
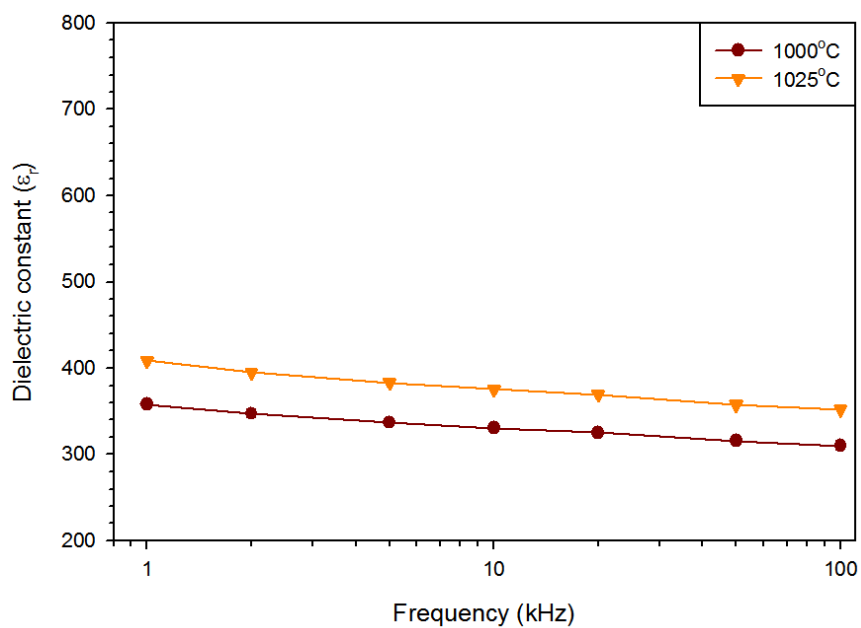
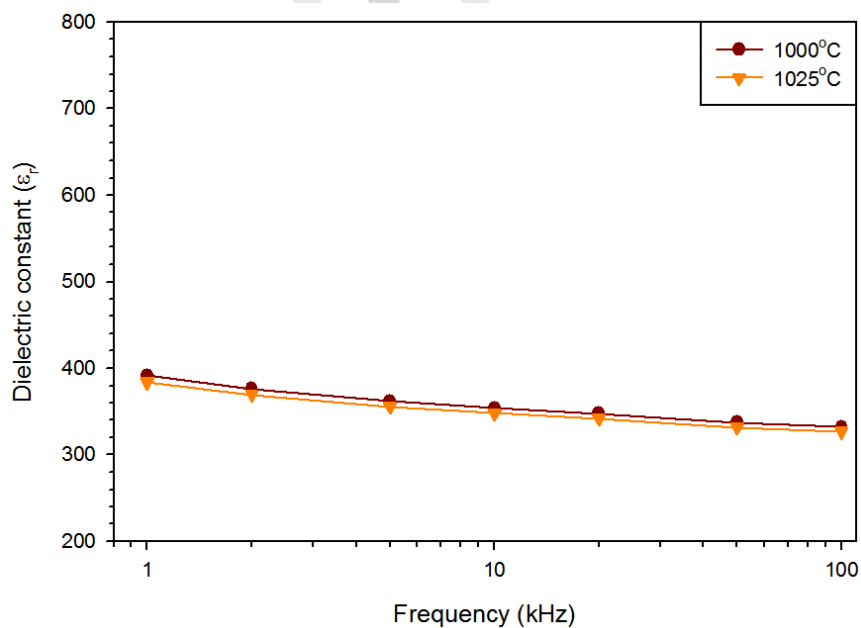


Figure 4.13 Dielectric constant of (a) 2 mol%, (b) 3 mol%, (c) 4 mol% and (d) 5 mol% Mn-doped $0.75BF-0.25BT$ ceramics sintered at various temperatures.

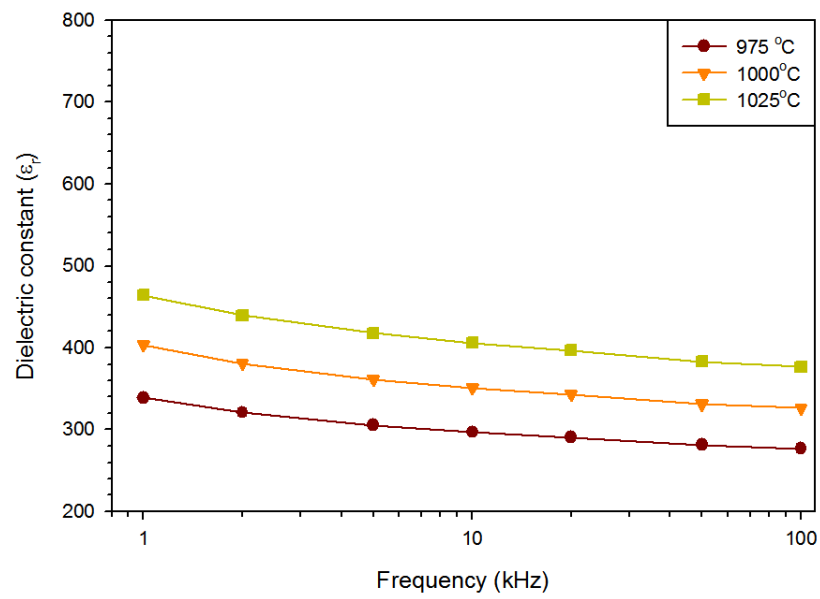


(b)



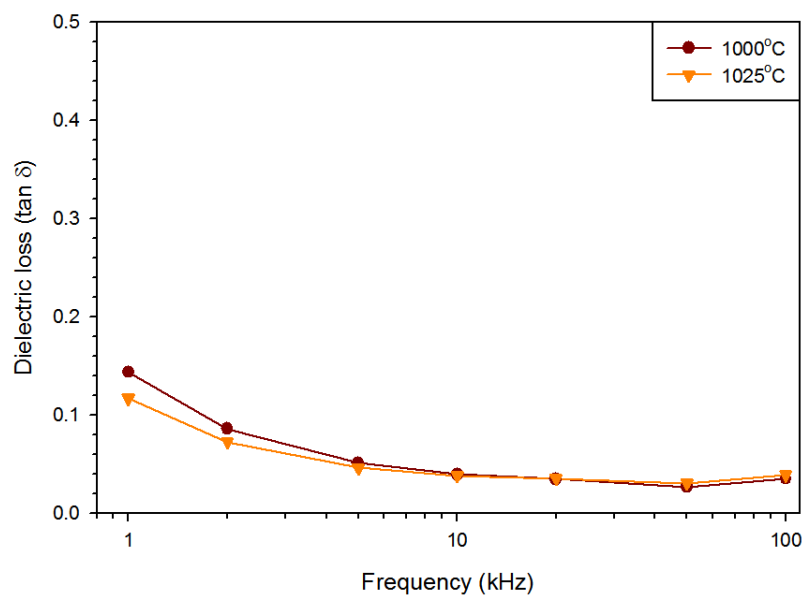
(c)

Figure 4.13 Dielectric constant of (a) 2 mol%, (b) 3 mol%, (c) 4 mol% and (d) 5 mol% Mn-doped 0.75BF-0.25BT ceramics sintered at various temperatures (Continued).

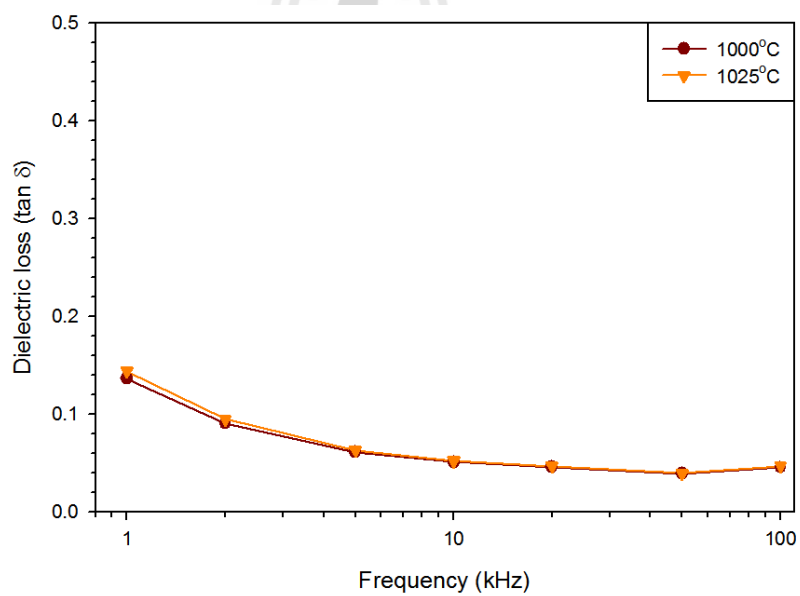


(d)

Figure 4.13 Dielectric constant of (a) 2 mol%, (b) 3 mol%, (c) 4 mol% and (d) 5 mol% Mn-doped $0.75BF-0.25BT$ ceramics sintered at various temperatures (Continued).

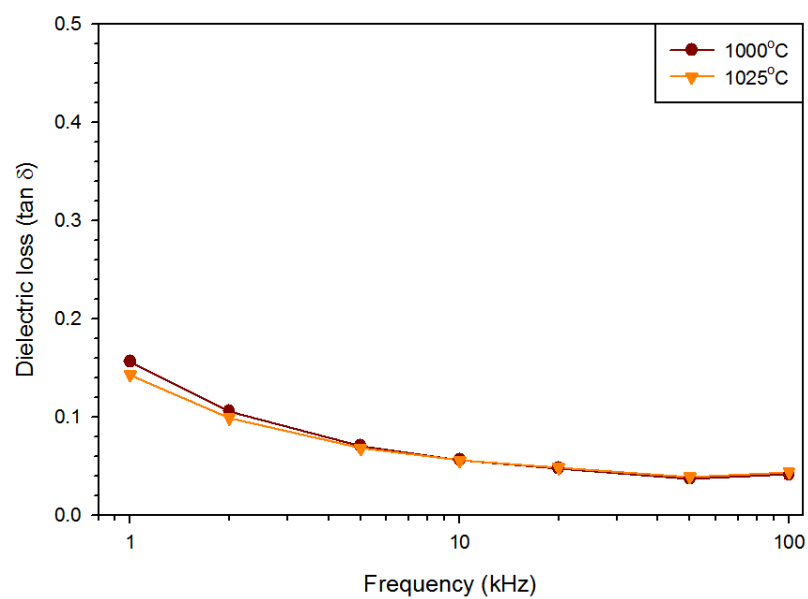


(a)

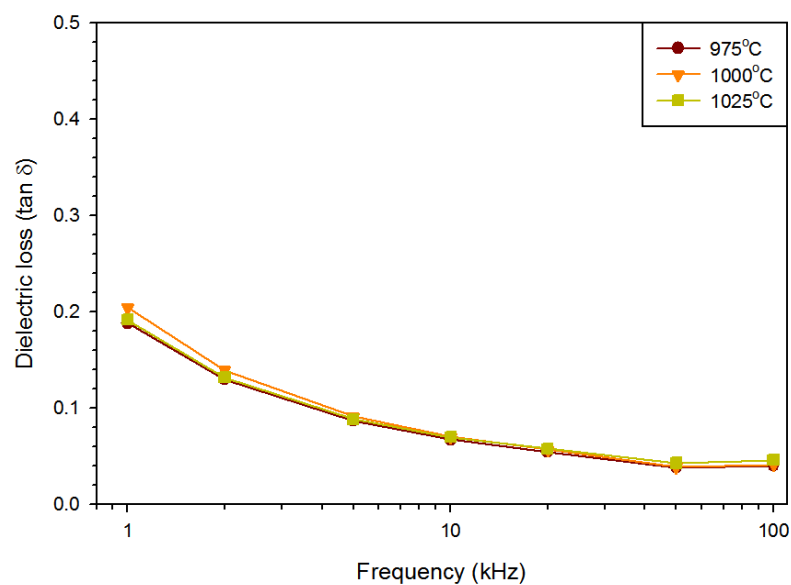


(b)

Figure 4.14 Dielectric loss of (a) 2 mol%, (b) 3 mol%, (c) 4 mol% and (d) 5 mol% Mn doped $0.75BF-0.25BT$ ceramics sintered at various temperatures.



(c)

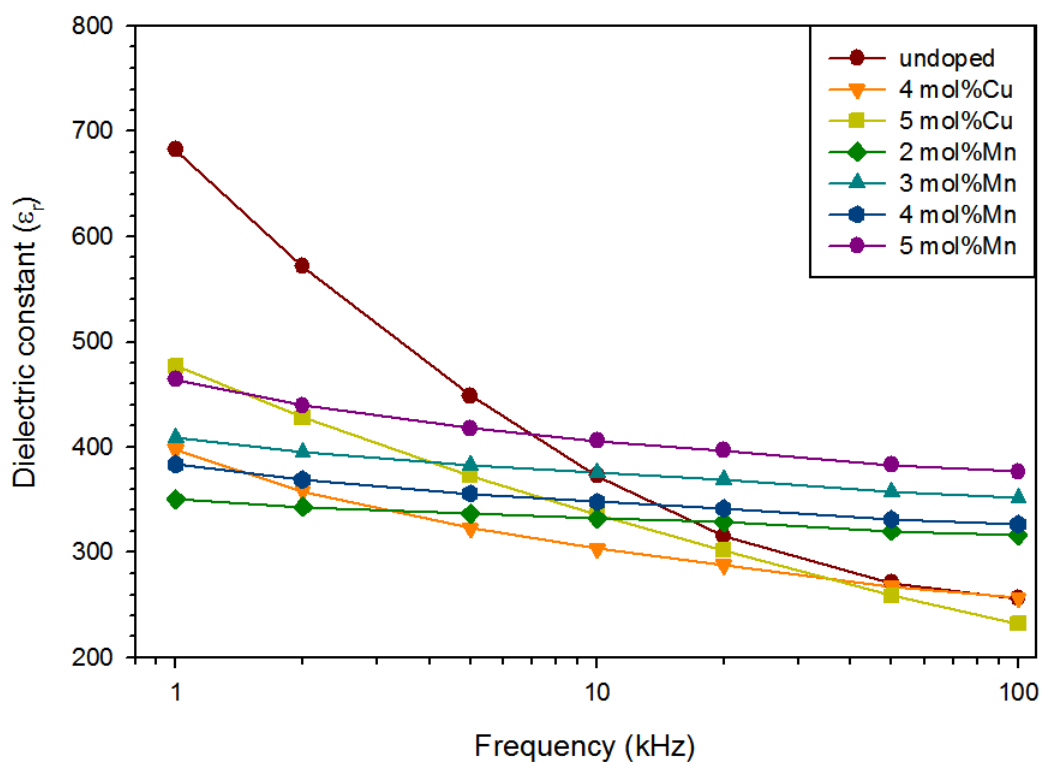


(d)

Figure 4.14 Dielectric loss of (a) 2 mol%, (b) 3 mol%, (c) 4 mol% and (d) 5 mol% Mn doped $0.75BF-0.25BT$ ceramics sintered at various temperatures (Continued).

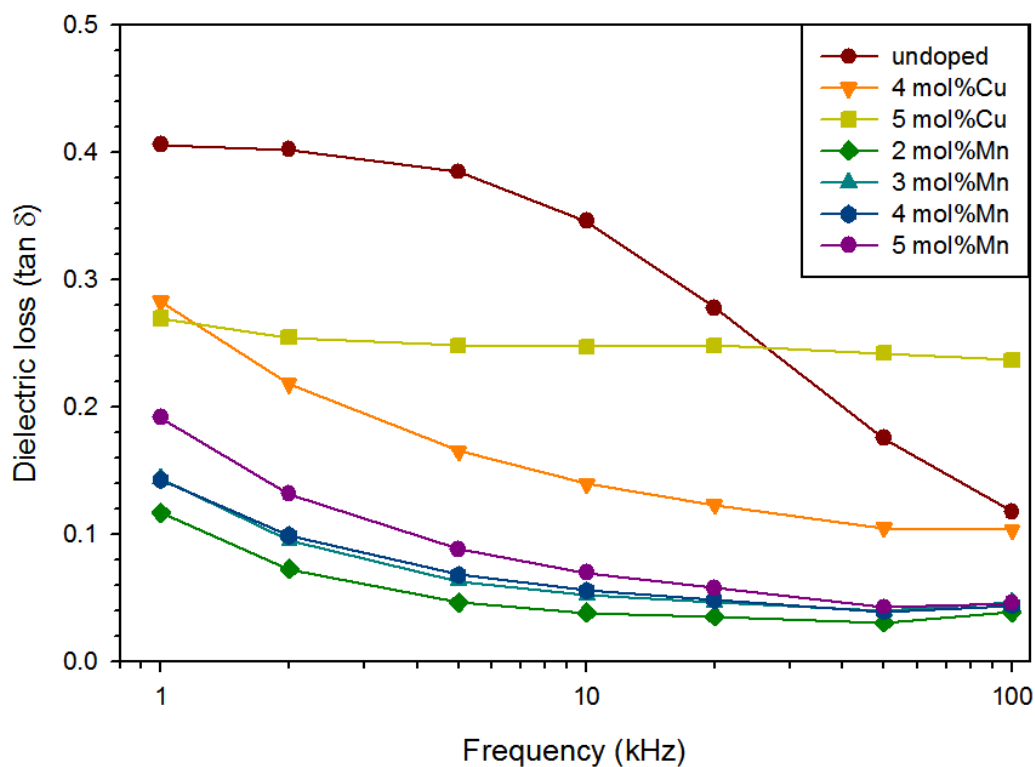
2. Effect of composition

Figure 4.15 shows dielectric properties of all ceramic samples sintered at the same sintering temperature (1025°C). As seen in Figure 4.15, improving of frequency dependence on dielectric properties of $0.75BF-0.25BT$ can be done by additions of Cu and Mn dopants. However, Cu-doped samples show stronger frequency dependence of dielectric properties than the Mn-doped samples. This causes by the effects of porosity and oxygen vacancy in Cu-doped samples.



(a)

Figure 4.15 Dielectric properties (a) dielectric constant and (b) dielectric loss of high density Cu- and Mn-doped $0.75BF-0.25BT$ ceramics sintered at 1025°C compared with undoped sample.



(b)

Figure 4.15 Dielectric properties (a) dielectric constant and (b) dielectric loss of high density Cu- and Mn-doped $0.75BF-0.25BT$ ceramics sintered at 1025°C compared with undoped sample (Continued).

On the other hand, the Mn doped $0.75BF-0.25BT$ show slightly higher on dielectric properties of both dielectric loss and dielectric constant when added more Mn content into $0.75BF-0.25BT$, as seen in Figure 4.15. As well known the function of the dopants is the creation of oxygen vacancies or negative charged defects which contribute to the schottky barrier formation and lead to high leakage current (Lee et al., 2006) which these effects affect to higher dielectric constant and dielectric loss.

Table 4.5 Dielectric properties of all ceramic samples measured at 1 kHz.

Composition	T_s (°C)	ϵ_r	$\tan \delta$
5 mol%Mn	975	339	0.19
5 mol%Cu	1000	352	0.21
2 mol%Mn		324	0.14
3 mol%Mn		358	0.14
4 mol%Mn		392	0.16
5 mol%Mn		404	0.20
undoped		690	0.41
4 mol%Cu		398	0.28
5 mol%Cu	477	0.27	
2 mol%Mn	1025	350	0.12
3 mol%Mn		408	0.14
4 mol%Mn		384	0.14
5 mol%Mn		464	0.19

4.7.2 Ferroelectric properties

Figure 4.16 shows the ferroelectric P - E hysteresis loops of all high density ceramic samples. The P - E hysteresis loops were measured at room temperature by pulse measurement (one cycle sine wave). The effects of Cu and Mn

addition on the ferroelectric properties of 0.75BF-0.25BT ceramics are clearly displayed in Figure 4.16.

P-E hysteresis loops of Cu-doped samples show rounded hysteresis loops than the undoped sample ($P_r = 8 \mu\text{C}/\text{cm}^2$) as a result of high leakage current which lead to low electrical break down voltage. Then saturated ferroelectric hysteresis loop of Cu-doped samples cannot be observed. It is possible oxygen vacancy, as charge carrier, from the substitution of Cu^{3+} for Ti^{4+} and grain boundary related phenomena are played dominant role when applied high electric field. However, in-situ investigation of oxygen migration should be done to support this expectation.

Figure 4.16(b) shows *P-E* hysteresis loops of Mn-doped samples. It was found that only 2 samples (2 mol%Mn sintered at 1000 and 1025°C) show typical ferroelectric hysteresis loops. The ferroelectric hysteresis loops could not be observed in the others samples. According to ferroelectric properties are controlled by Bi and Ti off-centered. As seen in *XRD* results, when added more Mn contents into 0.75BF-0.25BT, the distorted rhombohedral structure shows more symmetry, so ferroelectricity was reduced. Moreover, replacing of ferroelectric element Ti by magnetic element Mn, ferroelectricity is also decreased. Ferroelectric properties of all samples are listed in Table 4.6.

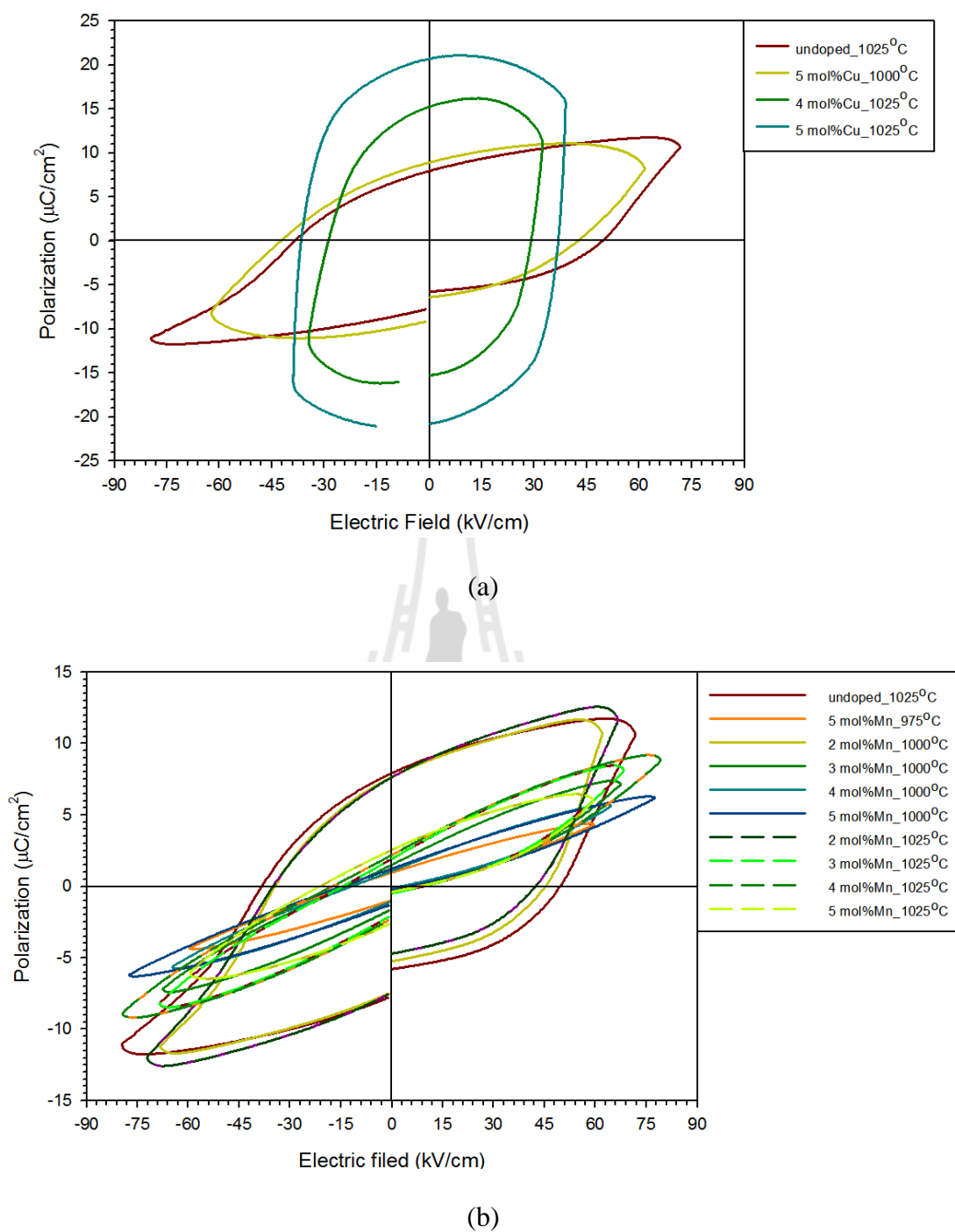


Figure 4.16 Ferroelectric properties of high density samples (a) Cu and (b) Mn doped $0.75BF-0.25BT$ ceramic samples compared with undoped ceramic sample.

Table 4.6 Ferroelectric properties of high density samples.

Sample	T_s ($^{\circ}\text{C}$)	P_r ($\mu\text{C}/\text{cm}^2$)	P_s ($\mu\text{C}/\text{cm}^2$)		E_c (kV/cm)	
			-	+	-	+
5 mol%Mn	975	1.0	4.4	4.4	12.8	4.3
5 mol%Cu	1000	8.9	8.2	8.3	42.6	42.4
2 mol%Mn		7.7	11.2	10.7	34.6	45.0
3 mol%Mn		1.6	7.2	7.2	13.1	8.0
4 mol%Mn		1.1	5.6	5.7	11.9	2.6
5 mol%Mn		1.2	6.2	6.2	15.0	4.5
4 mol%Cu		15.4	11.2	11.4	28.9	29.1
5 mol%Cu	1025	20.7	16.1	16.2	36.6	36.8
2 mol%Mn		7.7	11.9	11.8	35.1	42.1
3 mol%Mn		1.9	8.2	8.2	15.0	8.7
4 mol%Mn		2.2	8.9	9.0	18.2	6.2
5 mol%Mn		2.6	6.1	6.0	21.4	7.7

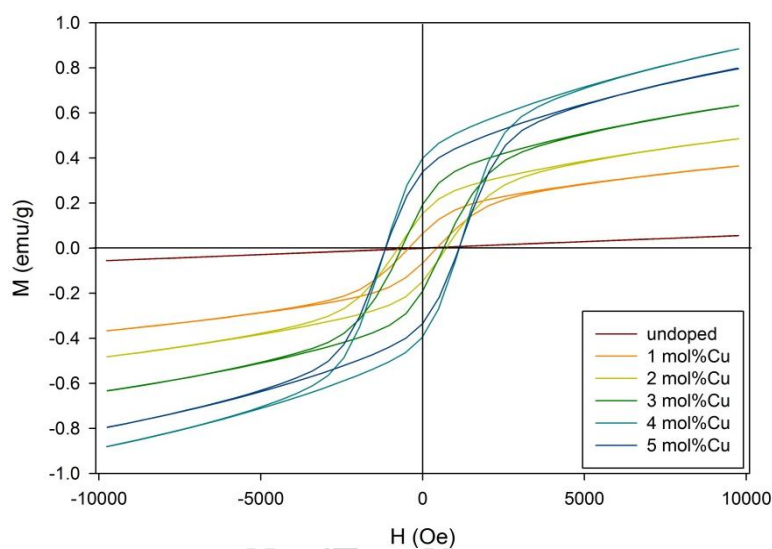
4.8 Magnetic properties

As described in Chapter II, magnetic properties arise from d^n configuration effect as filling d -shell that can only find in Fe^{3+} for $0.75BF-0.25BT$. However, magnetism of the doped samples not only depends on Fe^{3+} but also depends on the

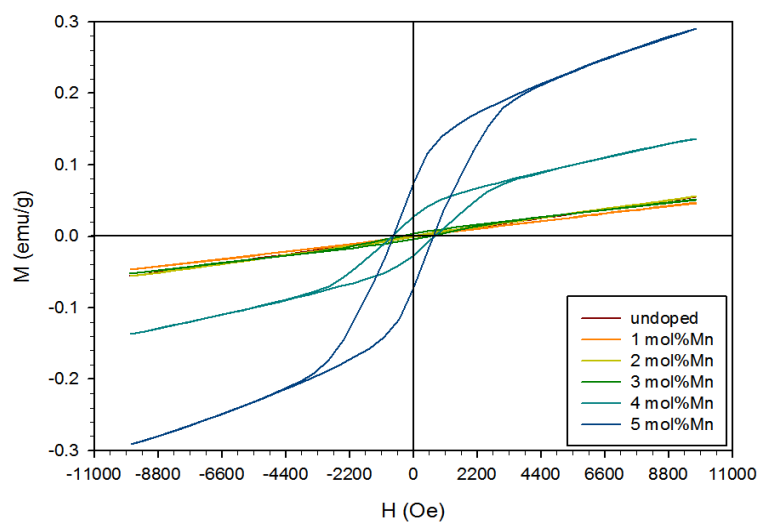
effects of structural symmetry and creation of lattice defect as reported previously (Gehring, 1994; Kumar et al., 1998; Liu et al., 2008). According to the spontaneous magnetic moment disappears when the structure becomes more symmetry (Kumar et al., 1998; Liu et al., 2008) and the creation of the lattice defects might lead to bulk magnetization and ferromagnetism (Gehring, 1994).

On the one hand, structural symmetry point of view, the *XRD* patterns revealed that the doped samples show no difference in their *XRD* patterns and they seem likely to be the same with previous work as extremely small rhombohedral distortion. Hence, the spontaneous magnetic moment which cause by structure distortion should be lower or disappear. On the other hand, creation of lattice defect point of view, as seen in Figure 4.17(a), magnetic properties of Cu-doped samples cause by the effect of lattice defect creation which Cu substitutes simultaneously for Fe and Ti ions in $0.75BF-0.25BT$ structure, so changing in magnetic properties should be contributed from the summation of the both substitution cases. When Cu ions substitute for Fe ions with the different filling *d*-shell, removing of Fe ions lead to lower cancelation of antiferromagnetism. In addition, in case of Cu ions substitute for Ti ions, ferroelectricity of Ti will be replaced by magnetism of Cu ions. Therefore, enhancing of ferromagnetic properties can be observed with increasing Cu content. Moreover, the effect of higher sintering temperature also affects to higher ferromagnetic properties of Cu-doped samples, the highest ferromagnetic properties can be observed in 4 mol%Cu sintered at 1025°C with $M_r \sim 0.4$ emu/g, as seen in Figure 4.18(a). The same results can be observed in case of the Mn-doped samples which the highest ferromagnetic properties ($M_r \sim 0.07$ emu/g) can be observed in 5 mol%Mn sintered at 1025°C. This can be noticed that the enhancing of ferromagnetic

properties of the undoped $0.75BF-0.25BT$ can be done by doping with Cu and Mn dopants. The magnetic properties of high density ceramic samples are listed in Table 4.7.



(a)



(b)

Figure 4.17 M - H hysteresis loops of (a) $\text{Bi}_{0.75}\text{Ba}_{0.25}(\text{Fe,Ti})_{1-x}\text{Cu}_x\text{O}_3$ and (b)

$\text{Bi}_{0.75}\text{Ba}_{0.25}(\text{Fe,Ti})_{1-x}\text{Mn}_x\text{O}_3$ with $x = 0, 1, 2, 3, 4$ and 5 mol%

(sintered at 1025°C).

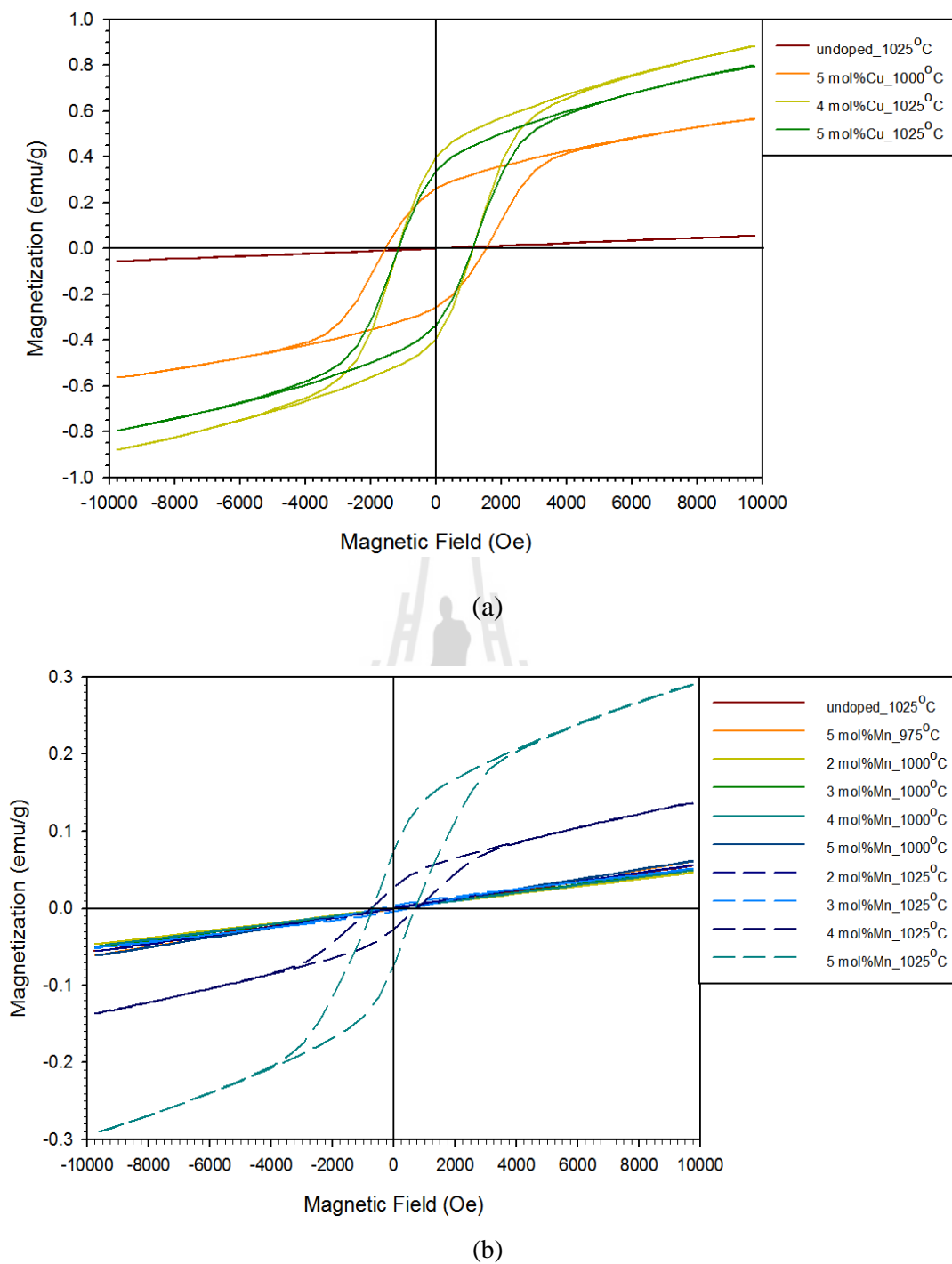


Figure 4.18 *M-H* hysteresis loops of the high density (a) Cu and (b) Mn doped $0.75BF-0.25BT$ samples compared with undoped.

Table 4.7 Magnetic properties of all samples.

Composition	T_s ($^{\circ}\text{C}$)	M_r (emu/g)	H_c (Oe)
5 mol%Mn	975	3.5×10^{-4}	55.2
5 mol%Cu	1000	2.6×10^{-1}	1524.5
2 mol%Mn		7.0×10^{-5}	18.6
3 mol%Mn		8.0×10^{-5}	22.9
4 mol%Mn		1.0×10^{-4}	14.9
5 mol%Mn		2.0×10^{-4}	37.2
undoped		8.6×10^{-4}	97.0
4 mol%Cu	1025	4.0×10^{-1}	1130.6
5 mol%Cu		3.4×10^{-1}	1121.4
2 mol%Mn		7.6×10^{-4}	120.5
3 mol%Mn		3.8×10^{-3}	493.9
4 mol%Mn		2.7×10^{-2}	723.3
5 mol%Mn		7.4×10^{-2}	689.8

4.9 Magnetoelectric coupling

As described in Chapter II, in point of view of possible application in the read head technology, magnetoelectric (*ME*) effect has been studied and used to identify potential of the sample for using in such technology. However, in this study, the optimized ceramic condition as required in the objective could not be observed.

Nevertheless, the representative samples that exhibit different multiferroic properties (ferroelectric and magnetic) of each dopant were investigated on *ME* effect through *ME* coefficient (α) for searching sample that can exhibit the great *ME* coefficient and suitable to develop for the future read head in hard disk drive technology. The *ME* coefficient was investigated by using a dynamic lock-in technique. The measurement was performed at constant frequency of 1 kHz and constant bias *AC* magnetic field of 5 Oe. The static *ME* coefficient was also measured as a function of *DC* magnetic field (H_{dc}) up to 4.6 kOe at room temperature. In this study, *ME* coefficient (α) was calculated by Eq. (4.1)

$$\alpha = V \text{ (mV) / thickness (cm) } * H_{dc} \text{ (kOe)} \quad (4.1)$$

As listed in Table 4.8, the representative Mn-doped samples which show the highest magnetic and ferroelectric properties and Cu-doped samples which show the highest magnetic properties and dielectric loss were investigated and compared with the undoped 0.75*BF*-0.25*BT* sample.

As shown in Figure 4.19, high dielectric loss of 5 mol%Cu-doped sample shows the lowest *ME* coefficients (α). While the others show higher *ME* coefficients (α) compared with undoped sample. The maximum *ME* coefficients (α) of Mn-doped samples can be observed in 2 mol%Mn doped 0.75*BF*-0.25*BT* sample with 0.44 mV/cmOe at H_{dc} 1.46 kOe.

The maximum *ME* coefficients (α) of Cu-doped samples can be observed in 4 mol%Cu doped 0.75*BF*-0.25*BT* sample with 0.18 mV/cmOe at H_{dc} 1.80 kOe.

Composition of 2 mol% Mn-doped 0.75*BF*-0.25*BT* sintered at 1025°C exhibits noticeably good magnetoelectric effect and is thus considered as the optimized

composition in this work to develop as the future read-head of the hard disk drive technology. It is possible that the composition has more geometrical mean of electric and magnetic susceptibility than the others, as described in Chapter II.

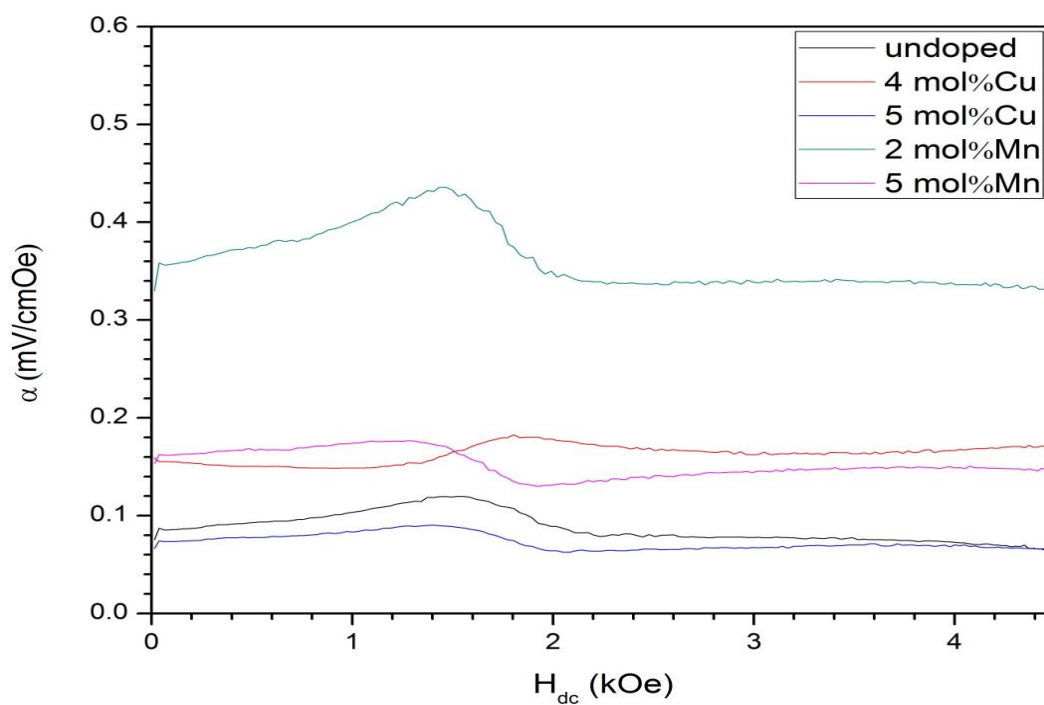


Figure 4.19 ME coefficients of undoped and 4 and 5 mol%Cu and 2 and 5 mol%Mn doped 0.75BF-0.25BT samples.

Table 4.8 Ferroelectric, magnetic and dielectric value of all high density samples.

Sample	T_s (°C)	M_r (emu/g)	P_r ($\mu\text{C}/\text{cm}^2$)	ϵ_r		$\tan \delta$	Relative density (%)
				1 kHz	100 kHz		
5 mol%Mn	975	3.5×10^{-4}	0.98	339	277	0.19	90.86
5 mol%Cu	1000	2.6×10^{-1}	8.93	352	219	0.21	92.34
2 mol%Mn		7.0×10^{-5}	7.69	324	290	0.14	93.61
3 mol%Mn		1.0×10^{-4}	1.59	358	310	0.14	93.63
4 mol%Mn		8.0×10^{-5}	1.09	392	332	0.16	93.71
5 mol%Mn		2.0×10^{-4}	1.23	404	326	0.20	93.93
undoped		8.6×10^{-4}	7.95	686	256	0.41	84.13
4 mol%Cu	1025	4.0×10^{-1}	15.24	398	256	0.27	92.74
5 mol%Cu		3.4×10^{-1}	20.70	477	232	0.28	92.62
2 mol%Mn		7.6×10^{-4}	7.72	350	316	0.12	94.07
3 mol%Mn		3.8×10^{-3}	1.93	408	351	0.14	94.63
4 mol%Mn		2.7×10^{-2}	2.24	384	326-	0.14	95.04
5 mol%Mn		7.4×10^{-2}	2.58	464	376	0.19	97.52

4.10 X-ray Absorption Spectroscopy (XAS)

The XAS technique in XANES region was used to determine the oxidation state and position of the interested atoms. The representative samples were characterized.

4.10.1 Fe K-edge

The selected samples were measured and compared with the standard Fe_2O_3 , the represent of Fe^{3+} . The results in Figure 4.20 show that Fe ions in the samples correspond to Fe^{3+} standard with Fe-O octahedral coordination. XANES spectra of the undoped 0.75BF-0.25BT sample show the same feature (A, B and C peak positions) of the standard Fe_2O_3 , seen in the inset of Figure 4.20. It can be conclude that the oxidation state of Fe ions of all samples are Fe^{3+} and the nearest atoms are oxygen. Interestingly, the XANES spectra of doped samples show lower intense of peak A which corresponds to higher centrosymmetric structure than the undoped 0.75BF-0.25BT sample (Mastelaro et al., 2009).

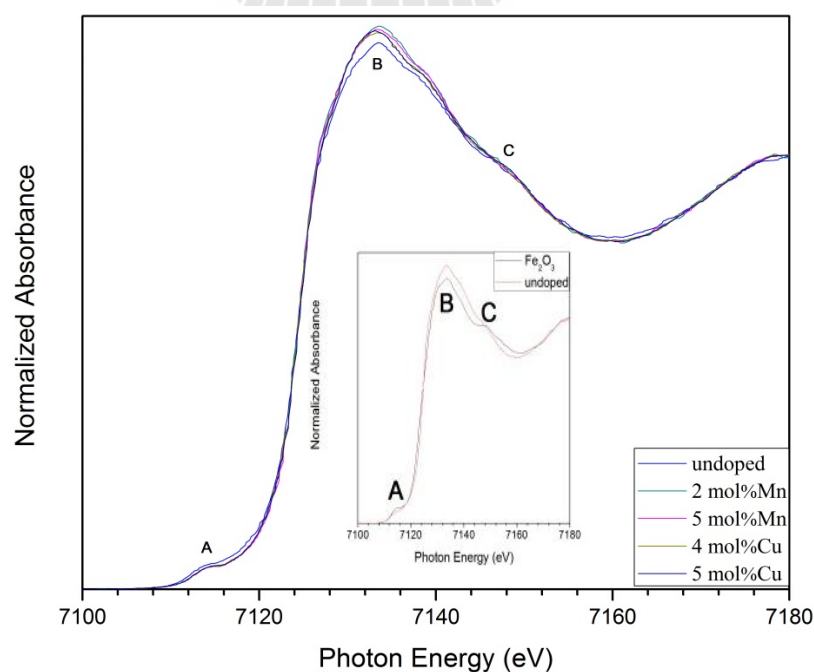


Figure 4.20 XANES spectra of all samples measured at Fe K-edge.

4.10.2 Ti *K*-edge

Ti *K*-edge spectra of the selected samples were performed to identify the oxidation state of Ti ions, shown in Figure 4.21. Bulk BaTiO₃ was used as a standard of Ti⁴⁺. The results show that the position and amplitude of pre-peak of the undoped 0.75*BF*-0.25*BT* sample (inset in Figure 4.21) and doped samples correspond to the standard. These results indicate that the oxidation state of Ti ions are Ti⁴⁺ and show 6-coordination as TiO₆ (Farges et al., 1997; Motta et al., 2009). It can be noticed that, there is a broad peak after the edge in all doped samples which can be attributed to short range order of the environment around the titanium ions (Motta et al., 2009).

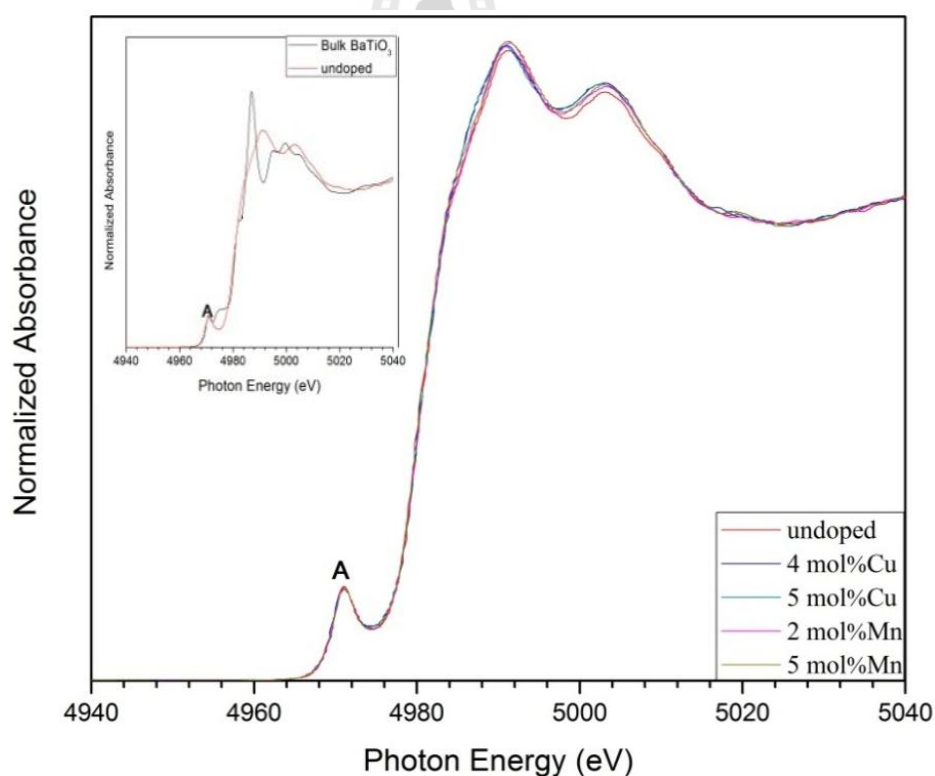


Figure 4.21 XANES spectra of the selected samples measured at Ti *K*-edge.

4.10.3 Cu K-edge

Figure 4.22 shows the XANES spectra of 4 and 5 mol%Cu doped 0.75BF-0.25BT samples measured at Cu K-edge and compared with Cu_2O and CuO as standards of Cu^{1+} and Cu^{2+} , respectively. The oxidation state of Cu in the samples does not correspond to any standard samples. As seen in Figure 4.22, the absorption edge of Cu in the samples located at higher energy than that of the two standards.

To identify the oxidation state of the samples, derivative and the point 50% of the jump ratio from the background absorption were done (Penner-Hahn, 2010). The results found that both the derivative and the point of 50% of the jump of the samples are located at higher energy than that of the standards. This result indicates that the oxidation state of Cu should be Cu^{3+} or a combination of Cu^{3+} and very small amount of Cu^{2+} .

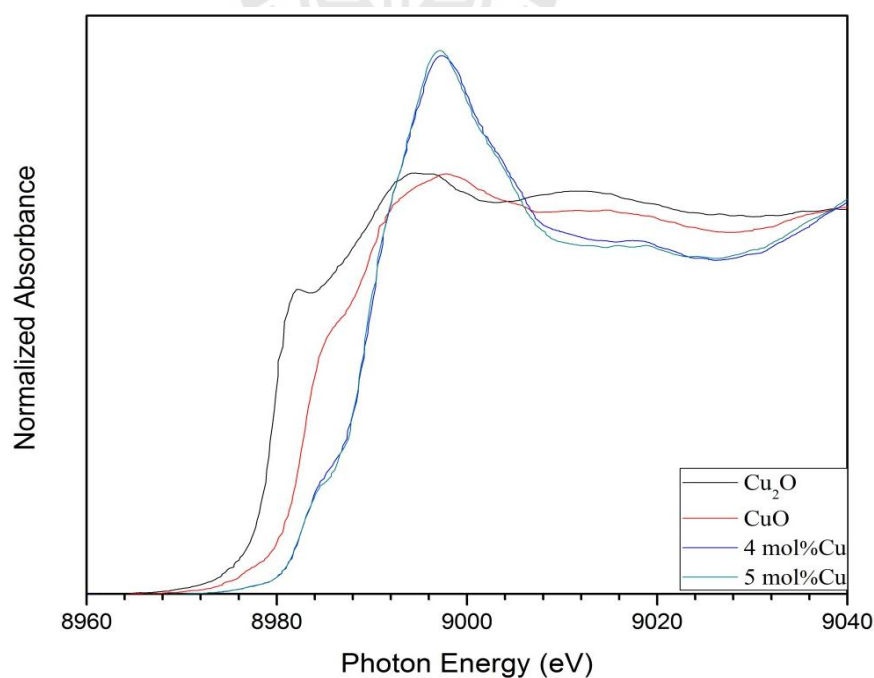


Figure 4.22 XANES spectra of Cu-doped samples measured at Cu K-edge.

4.10.4 Mn *K*-edge

Figure 4.23 shows the *XANES* spectra of Mn-doped samples measured at Mn *K*-edge and compared with MnO, Mn₂O₃ and MnO₂ as standards of Mn²⁺, Mn³⁺ and Mn⁴⁺, respectively. It can be noticed that the oxidation state of Mn is a combination of Mn⁴⁺ and Mn³⁺ as the absorption edge located between the absorption edges of Mn₂O₃ and MnO₂ (Higuchi et al., 2008). But the majority oxidation state should be Mn⁴⁺ as the edge absorption of the samples is closer than another one. Interestingly, the samples show the same Mn *K*-edge *XANES* spectra. That means amount of Mn addition in 0.75BF-0.25BT not affect to the oxidation state.

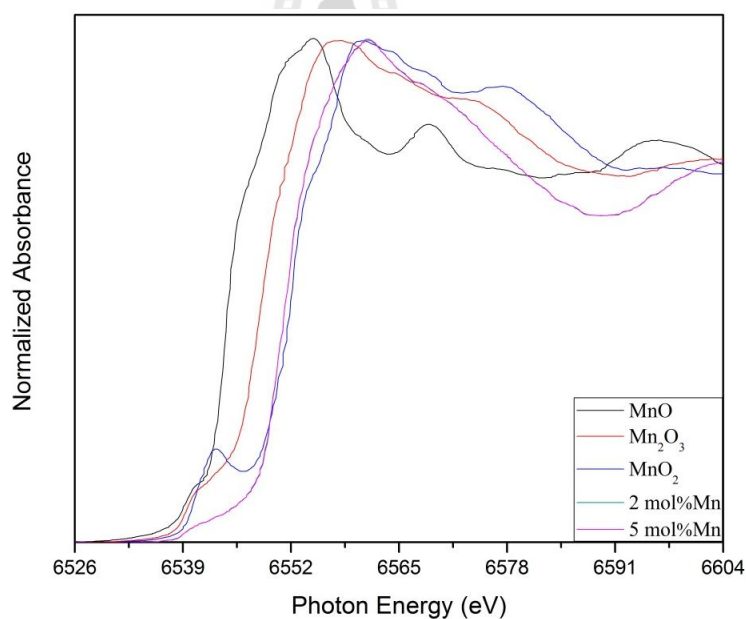


Figure 4.23 *XANES* spectra of Mn-doped samples measured at Mn *K*-edge.

4.10.5 Ba *L*₃- and Bi *M*₅-edges

XANES spectra of Ba and Bi measured at *L*₃- and *M*₅-edge are shown in Figures 4.24 and 4.25. Interestingly, Ba *L*₃-edge and Bi *M*₅-edge *XANES* spectra of the doped samples show the same feature as of the undoped 0.75BF-0.25BT sample.

These results indicate that the Ba and Bi-sites in the doped samples have the same environment as of the undoped $0.75BF-0.25BT$ sample.

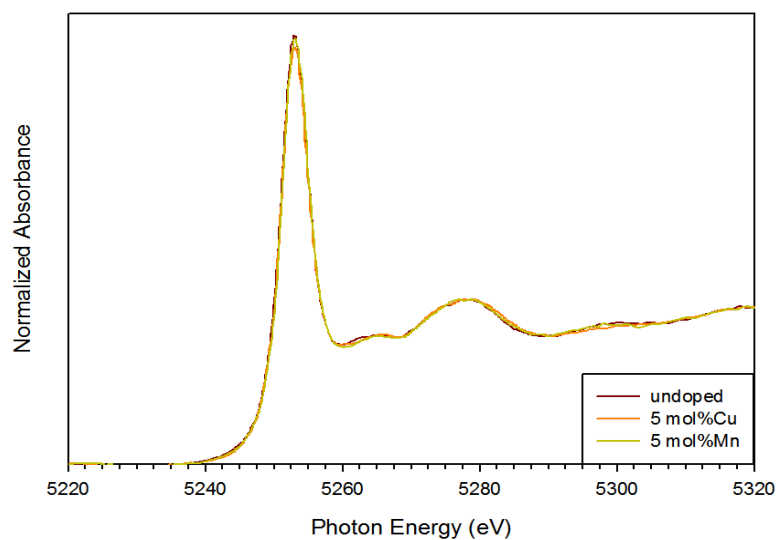


Figure 4.24 Ba L_3 -edge XANES spectra of undoped and Cu and Mn doped $0.75BF-0.25BT$ samples.

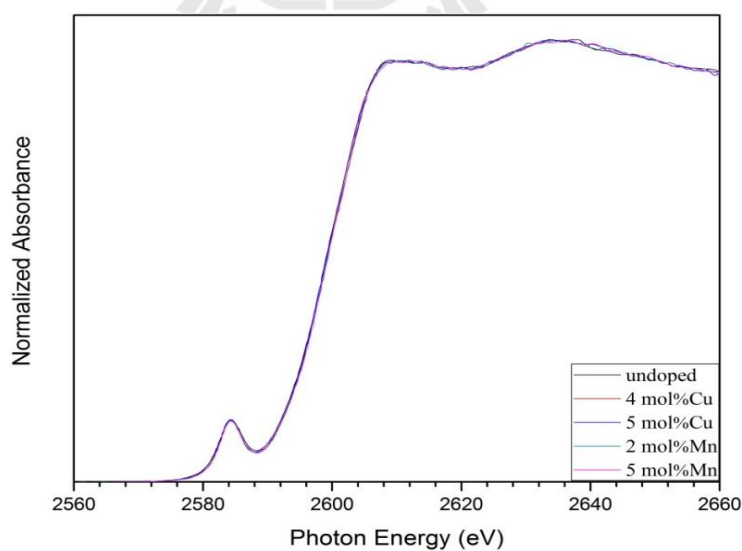


Figure 4.25 Bi M_5 -edge XANES spectra of undoped and Cu and Mn doped $0.75BF-0.25BT$ samples.

4.11 Simulation results

This work showed that $0.75BF-0.25BT$ structure was rhombohedral symmetry similar to that of the host BiFeO_3 , consistent with the previous work (Yoneda et al., 2008). Therefore, the simulated spectra of the absorbing atoms (Ti and Fe) were done by using the same structure as rhombohedral and lattice parameter of the undoped $0.75BF-0.25BT$. All simulated spectra were created by the atom.inp program and then calculated by FEFF8.2 code to obtain the simulated spectra.

4.11.1 Fe K-edge

Figure 4.26 shows the comparison of simulated and measured spectra of Fe K-edge. A small different feature was observed at peak B, at which the simulated spectra of BiFeO_3 show a splitting, while this could not be observed in the measured spectra. This simulated spectra was obtained from the approximation model, so they still show a little bit difference between them. However, the simulated spectra can be used to support that the structure of BiFeO_3 is rhombohedral.

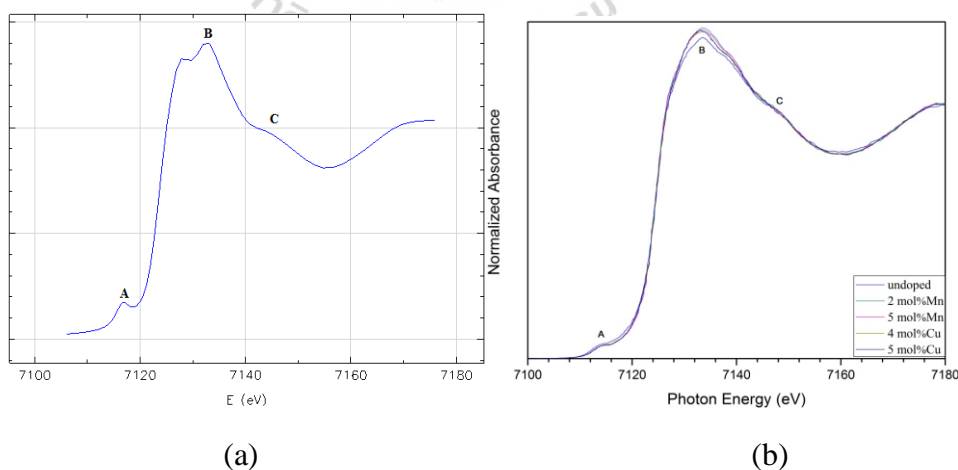


Figure 4.26 XANES spectra of Fe K-edge (a) simulated spectra of rhombohedral BiFeO_3 and (b) measured spectra.

4.11.2 Ti *K*-edge

Figure 4.27 shows the comparison of simulated and measured spectra of Ti *K*-edge. The simulated spectrum is similar to the measured spectra at Ti *K*-edge. Since the simulated spectra used the same parameters of $0.75BF-0.25BT$ rhombohedral structure, this result thus confirms that the structure of $BaTiO_3$ in all samples is rhombohedral.

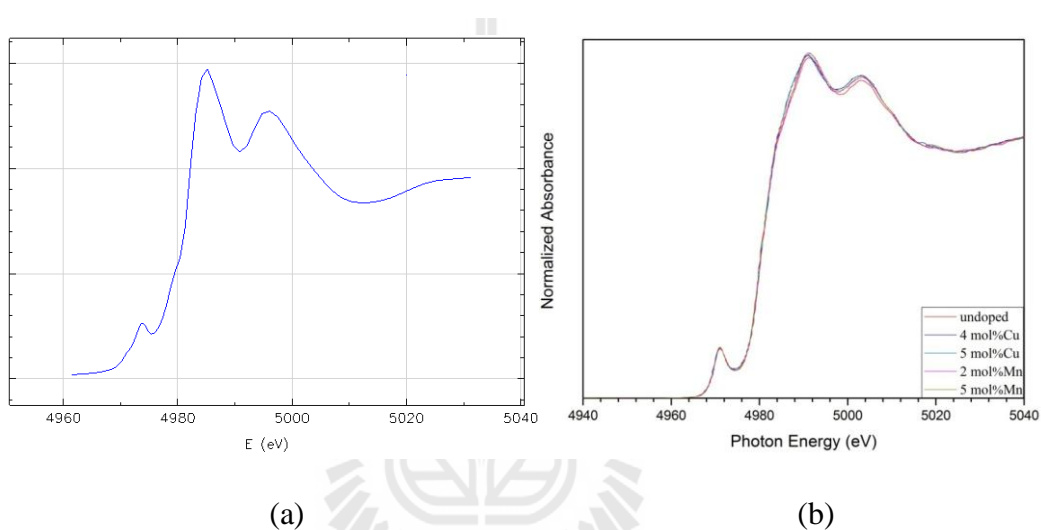


Figure 4.27 XANES spectra of Ti *K*-edge (a) simulated spectra of rhombohedral $BaTiO_3$ and (b) measured spectra.

To identify the oxidation state and position of the dopants Cu and Mn in $0.75BF-0.25BT$ structure, the results from *XRD* and *XAS* techniques were used. The *XRD* patterns indicate that Cu and Mn can be completely soluble in $0.75BF-0.25BT$, since there is no present of impurity phase. In addition, *XAS* results of Cu and Mn *K*-edge spectra show similar features to those of Fe and Ti *K*-edge spectra. These results can confirm that Mn and Cu are substituted for B-site atoms (Fe and Ti) as expected.

CHAPTER V

CONCLUSIONS AND SUGGESTIONS

5.1 Conclusions

The high relative density (90-98%) and purity single phase perovskite of $\text{Bi}_{0.75}\text{Ba}_{0.25}(\text{Fe},\text{Ti})_{1-x}\text{Cu}_x\text{O}_3$ and $\text{Bi}_{0.75}\text{Ba}_{0.25}(\text{Fe},\text{Ti})_{1-x}\text{Mn}_x\text{O}_3$ ceramics were obtained by using solid state reaction method with calcined temperature of 900°C and sintering temperature is in range of 975 - 1025°C . The XRD results show that their structures are extremely small rhombohedral distortion.

In addition, Cu and Mn doped $0.75\text{BF}-0.25\text{BT}$ show weaker frequency dependence on dielectric properties compared with the undoped sample. All high density ceramics show high dielectric constant in range of 320-480 measured at frequency of 1 kHz. However, dielectric loss in range of 0.05-0.15 as required in the research objective can be observed in some Mn doped $0.75\text{BF}-0.25\text{BT}$ compositions (2 and 3 mol%Mn sintered at 1000°C and 2, 3 and 4 mol%Mn sintered at 1025°C).

In case of ferroelectric properties, the addition of Mn content at 2 mol% sintered at 1000 and 1025°C show typical ferroelectric hysteresis loop with $P_r = 7.65$ and $7.72 \mu\text{C}/\text{cm}^2$, respectively. When Mn contents were increased, the typical ferroelectric hysteresis loops could not be observed due to more structural symmetry and replacement of ferroelectric Ti element effects. On the other hand, ferroelectric properties of Cu doped $0.75\text{BF}-0.25\text{BT}$ samples could not be measured because of their high leakage current effect from oxygen vacancy and grain boundary

related phenomena which played dominant role under high applied electric field.

High remanent magnetization (more than 0.15 emu/g) can be observed in only Cu-doped samples. The highest remanent magnetization can be obtained in 4 mol%Cu sintered at 1025°C with $M_r = 0.4$ emu/g.

The another interested property as *ME* coefficient (α) which used to identify the potential of read head in hard disk drive technology was also investigated in the selected samples. The results showed that 2 mol%Mn doped 0.75BF-0.25BT, which shows great ferroelectric and weak ferromagnetic properties, exhibits the highest *ME* coefficient (α) with 0.44 mV/cmOe at $H_{dc} = 1.46$ kOe. While the maximum *ME* coefficient (α) of Cu-doped sample can be observed in 4 mol%Cu doped 0.75BF-0.25BT sample with 0.18 mV/cmOe at $H_{dc} = 1.80$ kOe.

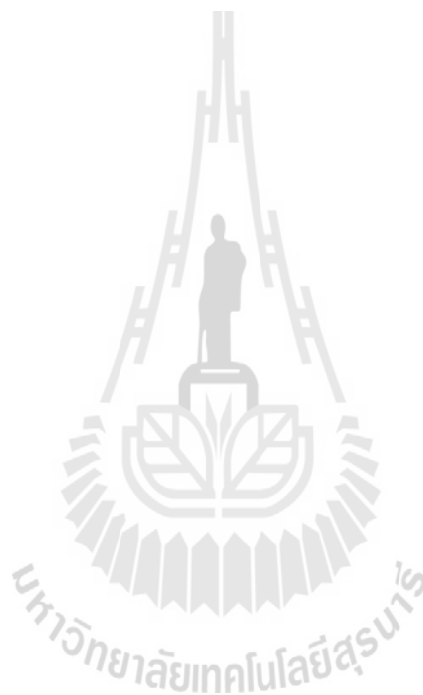
The investigation of the position and valency of Mn and Cu dopants in the 0.75BF-0.25BT with XAS technique revealed that oxidation state of Cu and Mn are Cu³⁺ or a combination of Cu³⁺ and very small amount of Cu²⁺ and combination of Mn⁴⁺ and very small amount of Mn³⁺, respectively. The simulated spectra of Fe and Ti *K*-edges showed that they are the same rhombohedral distortion structure. Therefore, the actual proportion of Cu and Mn substitute for Fe and Ti sites could not be identified. However, the results from XAS and XRD revealed that both Cu and Mn substituted for both Fe and Ti sites as there was no secondary phase obtained from XRD patterns and the similar XAS features in XANES region.

5.2 Suggestions

Although 2 mol%Mn doped 0.75BF-0.25BT is seen as the composition suitable for the development as the future read head, but in fact the read-head

technology should be formed as thin film. Therefore, thin-film form of such composition is of great interest to study on a possibility of practical application from this ceramic system.

In addition, since the *ME* effect is the important property to identify the performance of materials to be read head in *HDD* technology, one should consider performing more detailed magnetoelectric experiments on these ceramics in the future work.



REFERENCES

- Arlt, G., Hennings, D., and de With, G. (1985). Dielectric properties of fine-grained barium titanate ceramics. **Journal of Applied Physics**. 58: 1619-1625.
- Bunker, G. (2010). Introduction XAFS: A practical guide to X-ray Absorption Fine Structure Spectroscopy. **Cambridge University Press**.
- Carter CB., Norton MG. (2007). Ceramic Material/Science and Engineering. **Springer, New. York**.
- Chaisan, W., Yimnirun, R., Ananta, S., and Cann, D.P. (2005). Dielectric properties of solid solution in the Lead Zirconate Titanate-Barium Titanate system prepared by a modified mixed-oxide method. **Materials Letters**. 59(28): 3732-3737.
- Chaisan, W., Yimnirun, R., Ananta, S., and Cann, D.P. (2006). Phase development and dielectric properties of $(1-x)\text{Pb}(\text{Zr}_{0.52}\text{Ti}_{0.48})\text{O}_3-x\text{BaTiO}_3$ ceramics. **Materials Science and Engineering B**. 132(3): 300-306.
- Chaisan, W., Yimnirun, R., Ananta, S., and Cann, D.P. (2007). Dielectric and ferroelectric properties of lead zirconate titanate-barium titanate ceramics prepared by a modified mixed-oxide method. **Materials Chemistry and Physics**. 104(1): 113-118.
- Chandarak, S. (2008). Fabrication and Characterization of $(1-x)\text{BiFeO}_3-x\text{BaTiO}_3$ ceramics. **BS thesis, Chiang Mai University, Thailand**.
- Chandarak, S., Unruan, M., Sareein, T., Ngamjarrojana, A., Maensiri, S., Laorattanakul, P., Ananta, S., and Yimnirun, R. (2009). Fabrication and

- characterization of $(1-x)\text{BiFeO}_3-x\text{BaTiO}_3$ ceramics prepared by a solid state reaction method. **Journal of Magnetism**. 14(3): 120-123.
- Chang, J., Jang, H.M., and Kim, S.K. (2006). A possible origin of ferromagnetism in epitaxial BiFeO_3 thin films. **Journal of Magnetism**. 11(3): 108-110.
- Ciomaga CE., Buscaglia MT., Buscaglia V., Mitoseriu L. (2011). Oxygen deficiency and grain boundary-related giant relaxation in $\text{Ba}(\text{Zr,Ti})\text{O}_3$ ceramics. **Journal Applied Physics**. 110: 114110.
- Das S. (2011). Study of decomposition behavior of binders and the effect of binder type on strength and density of Alumina samples. **Bachelor Thesis. National Institute of Technology Rourkela**.
- de Souza, M.F., and de Souza, D.P.F. (1998). Glass phase expelling during liquid phase sintering of YSZ. **Materials Research**. 1: 53-58.
- Eerenstein, W, Morrison, F.D., Dho, J., Blamire, M.G., Scott, J.F., and Mathur, N.D. (2005). Comment on epitaxial BiFeO_3 multiferroic thin film heterostructures. **Science**. 307: 1203.
- Eerenstein, W., Mathur, N.D., and Scott, J.F. (2006). Multiferroic and magnetoelectric materials. **Nature**. 442: 759-765.
- Farges, F., Brown, Jr., G.E., and Rehr, J.J. (1997). Ti K-edge XANES studies of Ti coordination and disorder in oxide compounds: comparison between theory and experiment. **Physical Reviews B**. 56: 1809-1819.
- Fischer, P., Polomska, M., Sosnowska, I., and Szymanski, M. (1980). Temperature dependence of the crystal and magnetic structure of BiFeO_3 . **Journal of Physics a Solid C State Physics**. 13(9): 1931-1940.
- Fujii, T., Shimizu, S., Kajima, A., and Miyama, T. (1986). Film fabrication of solid

- solution of the $\text{BiFeO}_3\text{-BaTiO}_3$ system by rf-reactive sputtering. **Journal of Magnetism and Magnetic Materials**. 54(7): 1303-1304.
- Gehring GA. (1994). On the microscopic theory of the magnetoelectric effect. **Ferroelectrics**. 161: 275-285.
- Gu, Y.H., Wang, Y., Chen, F., Chan, H.L.W., and Chen, W.P. (2010). Nonstoichiometric $\text{BiFe}_{0.9}\text{Ti}_{0.05}\text{O}_3$ multiferroic ceramics with ultrahigh electrical resistivity. **Journal of Applied Physics**. 108: 094112-094112-5.
- Harald, F. (2011). Facilities for Radioactive Materials at Synchrotron Light Sources, Actinide-XAS-2000 (held in **Grenoble, France**).
- Higuchi, T., Sakamoto W., Itoh N., Shimura T., Hattori T., and Yogo T. (2008). Valence state of Mn-doped $\text{BiFeO}_3\text{-BaTiO}_3$ ceramics probed by soft X-ray absorption spectroscopy. **Applied Physics Express**. 1: 011502-1-011502-3.
- Ismailzade, I.H., Ismailov, R.M., Alekberov, A.I., and Salaev, F.M. (1981). Investigation of the magnetoelectric (ME)H effect in solid solutions of systems $\text{BiFeO}_3\text{-BaTiO}_3$ and $\text{BiFeO}_3\text{-PbTiO}_3$. **Physica Status Solidi (A)**. 68, K81-K85.
- Ismailzade, I.H., Ismailov, R.M., Alekperov, A.I., and Salaev, F.M. (1980). Magnetoelectric investigation of the system $\text{BiFeO}_3\text{-Pb}(\text{Fe}_{0.5}\text{Nb}_{0.5})\text{O}_3$. **Physica Status Solidi A**. 57(1): 99-103.
- Itoh, N., Shimura, T., Sakamoto, W., and Yogo, T. (2007). Fabrication and characterization of $\text{BiFeO}_3\text{-BaTiO}_3$ ceramics by solid state reaction. **Ferroelectrics**. 356: 19-23.
- Jae-wan, C., Jang, H.M., and Sang-Koog, K. (2006). A Possible origin of ferromagnetism in epitaxial BiFeO_3 thin films. **Journal of Magnetism**. 11(3):

108-110.

Jaffe, B., Cook (Jr.), W.R., and Jaffe, H. (1971). Piezoelectric ceramics. **Academic Press, New York.**

Julliere, M. (1975). Tunneling between ferromagnetic films. **Physics Letters A.** 54(3): 225-226.

Kadomtseva, A.M., Popov, Yu.F., Pyatakov, A.P., Vorobev, G.P., Zvezdin, A.K., and Viehland, D. (2006). Phase transitions in multiferroic BiFeO₃ crystals, thin-layers, and ceramics: enduring potential for a single phase, room-temperature magnetoelectric 'Holy Grail'. **Phase Transitions.** 79(12): 1019-1042.

Khomskii, D. (2009). Classifying multiferroic: Mechanisms and effects. **Physics.** 2(20), DOI: 10.1103.

Kiselev, S.V., Ozarov, R.P., and Zhdanov, G.S. (1936). Detection of magnetic order in ferroelectric BiFeO₃ by neutron diffraction. **Soviet Physics Doklady.** 7: 742-744.

Kubel, F., and Schmid, H. (1990). Structure of ferroelectric and ferroelastic monodomain crystal of the perovskite BiFeO₃. **Acta Crystallographica Section B.** 46(6): 698-702.

Kumar, M.M., Srinath, S., Kumar, G.S., and Suryanarayana, S.V. (1998). Spontaneous magnetic moment in BiFeO₃-BaTiO₃ solid solutions at low temperatures. **Journal of Magnetism and Magnetic Materials.** 188: 203-212.

Kumar, M.M., Srinivas, A., and Suryanarayana, S.V. (2000). Structure property relations in BiFeO₃-BaTiO₃ solid solutions. **Journal of Applied Physics.** 87(2): 855-862.

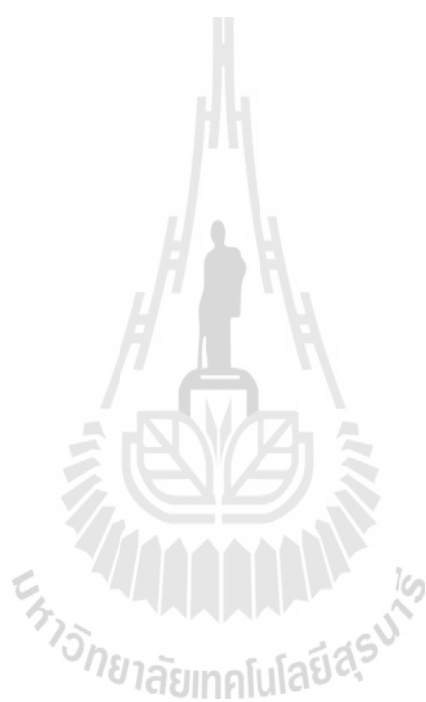
- Lee HJ., Kim CD., Kang SH., Kim WI., Lee JS., Chung GS. (2006). Influence of sintering temperature on conduction behaviors for CoO- and ZnO-doped SnO₂ varistor ceramics. **Journal of the Korean Physical Society**. 49(6): 2423-2427.
- Leontsev, S.O., and Eitel, R.E. (2009). Dielectric and piezoelectric properties in Mn-modified (1-x)BiFeO₃-xBaTiO₃ ceramics. **Journal of the American Ceramic Society**. 92(12): 2957-2961.
- Li YW., Hu ZG., Yue FY., Yang PX., Qian YN., Cheng WJ., Ma XM., and Chu JH. (2008). Oxygen-vacancy-related dielectric relaxation in BiFeO₃ film grown by pulsed laser deposition. **Journal of Physics D: Applied Physics**. 41: 215403.
- Li, J.F., Wang, J.L., Wuttig, M., Ramesh, R., Wang, N., Ruetter, B., Pyatakov, A.P., Zvezdin, A.K., and Viehland, D. (2004). Dramatically enhanced polarization in (001), (101), and (111) BiFeO₃ thin films due to epitaxial-induced transitions. **Applied Physics Letters**. 84(25): 5261-5263.
- Lui XH., Xu Z., Qu SB., Wei XY., Chen JL. (2008). Ferroelectric and ferromagnetic properties of M-doped 0.7BiFeO₃-0.3BaTiO₃ solid solution. **Ceramics International**. 34: 797-801.
- Mastelaro, VR., Mesquita A., Neves PP., Michalowicz A., and Bounif M. (2009). Short-range structure of Pb_{1-x}Ba_xZr_{0.65}Ti_{0.35}O₃ ceramic compounds probed by XAS and Raman scattering techniques. **Journal of Applied Physics**. 105: 033508-1-033508-6.
- Mazumder, R., Sen, A. (2009). Effect of Pb-doping on dielectric properties of BiFeO₃ ceramics. **Journal of Alloys and Compounds**. 475: 577-580.
- Motta, F.V., de Figueiredo, A.T., Longo, V.M., Mastelaro, V.R., Freitas, A.Z.,

- Gomes, L., Vieira Jr., N.D., Longo, E, and Varela, J.A. (2009). Disorder-dependent photo-luminescence in $\text{Ba}_{0.8}\text{Ca}_{0.2}\text{TiO}_3$ at room temperature, **Journal of Luminescence**. 129: 686–690.
- Moulson, A.J., and Herbert, J.M. (2003). *Electroceramics: Materials. Properties. Applications*. 2nd edition. **John Wiley & Sons Ltd. New York**.
- Ozaki, T., and Mori, S. (2009). Dielectric properties and related domain structures in 0.75BiFeO_3 - 0.25BaTiO_3 . **Japanese Journal of Applied Physics**. 48(9): 09KC07-09KC07-4.
- Pabst, G.W., Martin, L.W., Chu, Y.H., and Ramesh, R. (2007). Leakage mechanism in BiFeO_3 thin films. **Applied Physics Letters**. 90: 072902.
- Penner-Hahn, J.E. (2010). *X-ray Absorption Spectroscopy*. The University of Michigan, **Ann Arbor, Michigan, USA**.
- Riedel R., and Chen IW. (2012). *Ceramics Science and Technology: Volume 3: Synthesis and Processing*, 1st Edition, **Wiley-VCH Verlag GmbH & Co. KGaA. Weinheim**.
- Shackelford, J.E. (2005). *Introduction to materials science for engineers*. 6th edition. **New Jersey. Pearson Education**.
- Sosnowska, I., Przenioslo, R., Fischer, P., and Murashov, V.A. (1996). Neutron diffraction studies of the crystal and magnetic structures of BiFeO_3 and $\text{Bi}_{0.93}\text{La}_{0.07}\text{FeO}_3$. **Journal of Magnetism and Magnetic Materials**. 160: 384-385.
- Sunder, V.S., Halliyal, A., and Umarji, A.M. (1995). Investigation of tetragonal distortion in the PbTiO_3 - BiFeO_3 system by high-temperature X-ray diffraction. **Journal of Materials Research**. 10(5): 1301-1306.

- Teague, J.R., Gerson, R., and James, W.J. (1970). Dielectric hysteresis in single crystal BiFeO_3 . **Solid State Communications**. 8(13): 1073-1074.
- Velev, J.P., Jaswal, S.S., and Tsymbal, E.Y. (2011). Multi-ferroic and magnetoelectric materials and interfaces. **Philosophical Transactions of The Royal Society A**. 369: 3069-3097.
- Vopsaroiu, M., Blackburn, J., Muniz-Piniella, A., and Cain, M.G. (2008). Multiferroic magnetic recording read head technology for 1 Tbit/in.² and beyond. **Journal of Applied Physics**. 103(7): 07F506-07F506-3.
- Wada, T., Tokunaga, Y., Kajima, A., Inoue, M., Fujii, T., Jeyadevan, B., and Tohji, K. (1997). Ferromagnetism and ferroelectricity of $\text{Bi}_2\text{O}_3\text{-Fe}_2\text{O}_3\text{-PbTiO}_3$ amorphous oxide films prepared by gel-coating technique. **Applied Surface Science**. 113- 114: 212-216.
- Wang, D.H., Goh, W.C., Ning, M., and Ong, C.K. (2006). Effect of Ba doping on magnetic, ferroelectric, and magnetoelectric properties in multiferroic BiFeO_3 at room temperature. **Applied Physics Letters**. 88(21): 212907-212907-3.
- Wang, J., Neaton, J.B., Zheng, H., Nagarajan, V., Ogale, S.B., Liu, B., Viehland, D., Vaithyanathan, V., Schlom, D.G., Waghmare, U.V., Spaldin, N.A., Rabe, K.M., Wuttig, M., and Ramesh, R. (2003). Epitaxial BiFeO_3 multiferroic thin film heterostructures. **Science**. 299(5613): 1719-1722.
- Wang, K.F., Liu, J.M., and Ren, Z.F. (2009). Multiferroicity: the coupling between magnetic and polarization orders. **Advances in Physics**. 58(4): 321-448.
- Williams, E.M. (2001). Design and analysis of magnetoresistive recording heads. **Wiley, New York**.
- Xiao-Hui, L., Zhuo, X., Shao-Bo, Q., Xiao-Yong, W., and Jiang-Li, C. (2008).

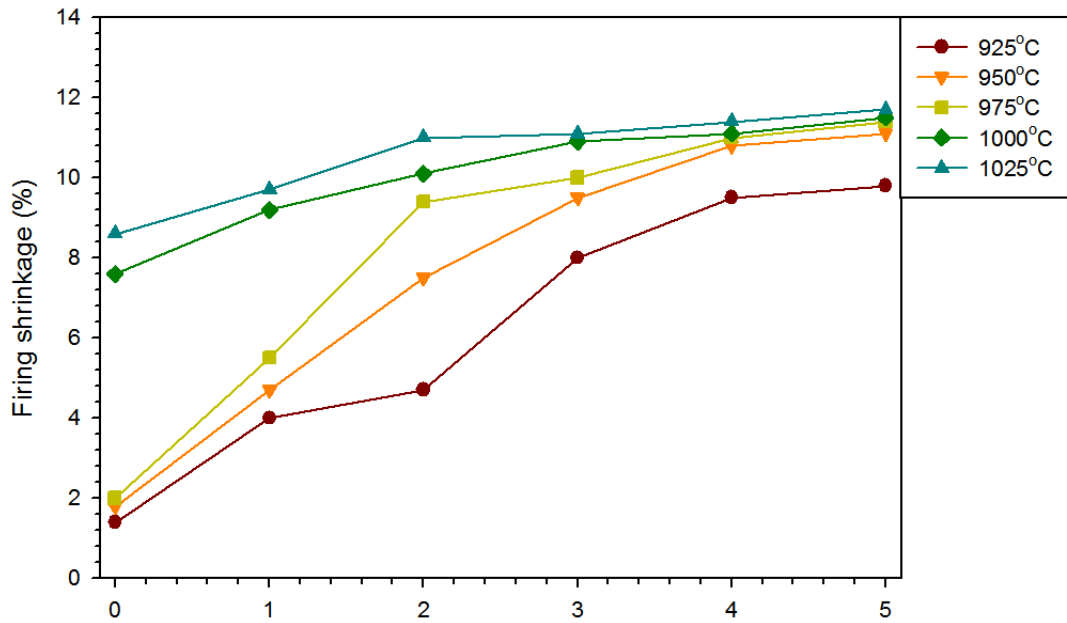
- Ferroelectric and ferromagnetic properties of Mn-doped 0.7BiFeO₃-0.3BaTiO₃ solid solution. **Ceramics International**. 34(4): 797-801.
- Xiao-Hui, L., Zhuo, X., Shao-Bo, Q., Xiao-Yong, W., and Jiang-Li, C. (2007). Microstructure and properties of Ga-modified 0.7BiFeO₃- 0.3BaTiO₃ solid solution. **Chinese Science Bulletin**. 52(20): 2747-2752.
- Xiao-Hui, L., Zhuo, X., Xiao-Yong, W., and Xi, Y. (2008). Ferroelectric and ferromagnetic properties of 0.7BiFe_{1-x}Cr_xO₃-0.3BaTiO₃ solid solutions. **Journal of the American Ceramic Society**. 91(11): 3731-3734.
- Xu, Y. (1991). Ferroelectric Materials and Their Applications. **North-Holland, Amsterdam**.
- Yimnirun, R. (2006). Change in the dielectric properties of normal and relaxor ferroelectric ceramic composites in BT-PZT and PMN-PZT system compressive stress. **Ferroelectrics**. 331(1): 9-18.
- Yimnirun, R., Ananta, S., and Chamunglap, S. (2007). Dielectric properties of (1-x)Pb(Zr_{0.52}Ti_{0.48})P₃-(x)BaTiO₃ ceramics under uniaxial compressive pre-stress. **Materials Chemistry and Physics**. 102(2-3): 165-170.
- Yoneda, Y., Yoshii, K., Kohara, S., Kitagawa, S., and Mori, S. (2008). Local structure of BiFeO₃-BaTiO₃ mixture. **Japanese Journal of Applied Physics**. 47(9): 7590-7594.
- Yun, K.Y., Noda, M., Okuyama, M., Saeki, H., Tabata, H., and Saito, K. (2004). Structural and multiferroic properties of BiFeO₃ thin films at room temperature. **Journal of Applied Physics**. 96(6): 3399-3403.
- Zhang, Y., Li, Z., Deng, C., Ma, J., Lin, Y., and Nan, C.W. (2008). Demonstration of magnetoelectric read head of multiferroic heterostructures. **Applied Physics**

Letters. 92(15): 152510-152510-3.





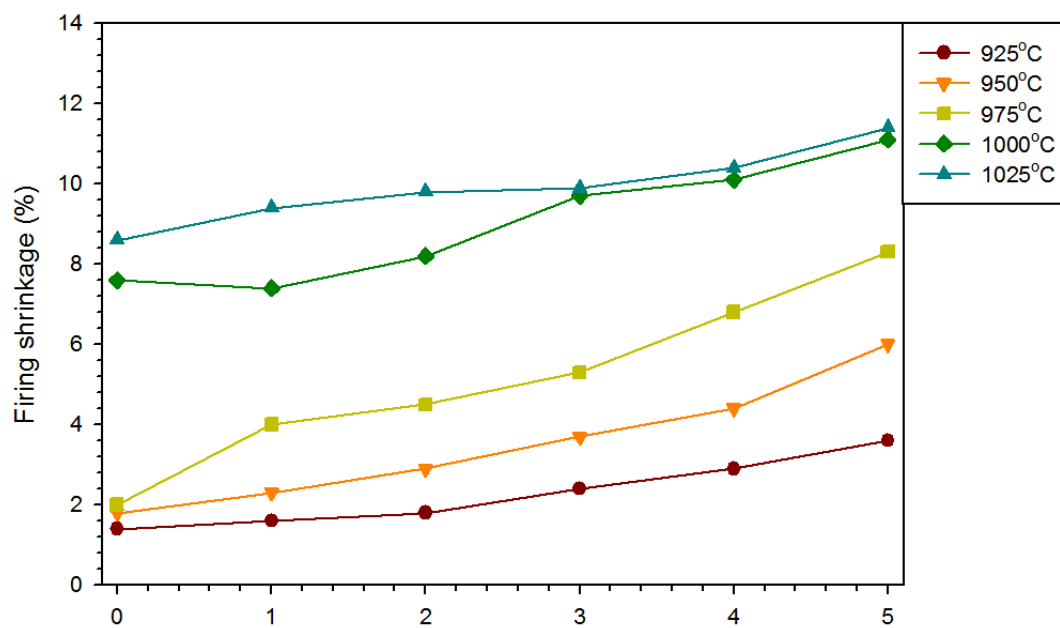
APPENDIX A
FIRING SHRINKAGE



x

(a)

Figure A.1 Firing shrinkage of (a) $\text{Bi}_{0.75}\text{Ba}_{0.25}(\text{Fe},\text{Ti})_{1-x}\text{Cu}_x\text{O}_3$ and (b) $\text{Bi}_{0.75}\text{Ba}_{0.25}(\text{Fe},\text{Ti})_{1-x}\text{Mn}_x\text{O}_3$ ceramics at $x = 0, 1, 2, 3, 4$ and 5 mol% with 2 drops (0.08 grams) aqueous *PVA* per gram of sample powders for pressing process.

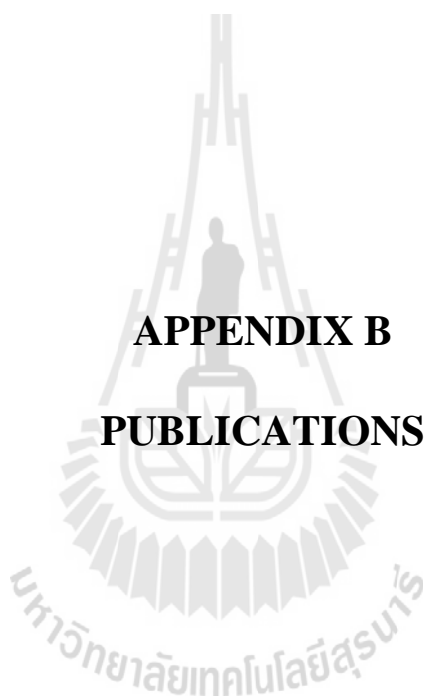


x

(b)

Figure A.1 Firing shrinkage of (a) $\text{Bi}_{0.75}\text{Ba}_{0.25}(\text{Fe},\text{Ti})_{1-x}\text{Cu}_x\text{O}_3$ and (b) $\text{Bi}_{0.75}\text{Ba}_{0.25}(\text{Fe},\text{Ti})_{1-x}\text{Mn}_x\text{O}_3$ ceramics at $x = 0, 1, 2, 3, 4$ and 5 mol% with 2 drops (0.08 grams) aqueous *PVA* per gram of sample powders for pressing process (Continued).

APPENDIX B
PUBLICATIONS



List of publications

- Silawongsawat, C., Chandarak, S., Sareein, T., Ngamjarrojana, A., Meansiri, S., Laoratanakul, P., Ananta, S., and Yimnirun, R. (2008). Effect of calcinations on phase formation and characterization of BiFeO₃ powders synthesized by a solid-state reaction. **Advanced Materials Research**. 55-57: 237-240.
- Chandarak, S., Sareein, T., Ngamjarrojana, A., Meansiri, S., Laoratanakul, P., Ananta, S., and Yimnirun, R. (2008). Effect of calcination conditions on phase formation and characterization of BiFeO₃-BaTiO₃ powders synthesized by a solid-state reaction. **Advanced Materials Research**. 55-57: 241-244.
- Chandarak, S., Unruan, M., Sareein, T., Ngamjarrojana, A., Maensiri, S., Laoratanakul, P., Ananta, S., and Yimnirun, R. (2009). Fabrication and characterization of (1-x)BiFeO₃-xBaTiO₃ ceramics prepared by a solid state reaction method. **Journal of Magnetism**. 14: 120-123.
- Chandarak, S., Ngamjarrojana, A., Srilomsak, S., Rujirawat, S., and Yimnirun, R. (2010). Effects of Mn and Cu doping on electrical properties of 0.75BiFeO₃-0.25BaTiO₃ ceramics. **Integrated Ferroelectrics**. 114: 100-107.
- Chandarak, S., Ngamjarrojana, A., Srilomsak, S., Laoratanakul, P., Rujirawat, S., and Yimnirun, R. (2011). Dielectric properties of BaTiO₃-modified BiFeO₃ ceramics. **Ferroelectrics**. 410: 75–81.
- Wongsaenmai, S., Kanchiang, K., Chandarak, S., Laosiritaworn, Y., Rujirawat, S., and Yimnirun, R. (2012). Crystal structure and ferroelectric properties of Mn-doped ((K_{0.5}Na_{0.5})_{0.935}Li_{0.065})NbO₃ lead-free ceramics. **Current Applied**

Physics. 12: 418-421.

Chandarak, S., Pojprapai, S., Srilomsak, S., Jantaratana, P., Rujirawat, S., and Yimnirun, R. (2011). Magnetolectric properties of Cu- and Mn-Doped $0.75\text{BiFeO}_3\text{-}0.25\text{BaTiO}_3$ multiferroic ceramics. **Ferroelectrics.** 419: 70-75.

Chandarak, S., Jutimoosik, J., Pojprapai, S., Srilomsak, S., Rujirawat, S., and Yimnirun, R. (2011). Synchrotron X-ray absorption study of Cu- and Mn-doped $\text{BiFeO}_3\text{-BaTiO}_3$ multiferroic ceramics. **Ferroelectrics.** 422: 23–29.

Unruan, M., Sareein, S., Chandarak, S., Hunpratub, S., Thongbai, P., Maensiri, S., and Yimnirun, R. (2012). Aging and stress-dependent dielectric properties of multiferroic Bismuth Ferrite ceramics. **Materials Letters.** 70: 185-188.

Chokprasombat, K., Sirisathitkul, C., Harding, P., Chandarak, S., and Yimnirun, R. (2012). Synchrotron X-ray absorption spectroscopy study of self-assembled nanoparticles synthesized from $\text{Fe}(\text{acac})_3$ and $\text{Pt}(\text{acac})_2$. **Journal of Nanomaterials.** 2012: 758429-1-758429-4.



Research Article

Synchrotron X-Ray Absorption Spectroscopy Study of Self-Assembled Nanoparticles Synthesized from Fe(acac)₃ and Pt(acac)₂

K. Chokprasombat,¹ C. Sirisathitkul,¹ P. Harding,¹ S. Chandarak,² and R. Yimnirun³

¹Molecular Technology Research Unit, School of Science, Walailak University, Nakhon Si Thammarat 80161, Thailand

²School of Ceramic Engineering, Institute of Engineering, Suranaree University of Technology, Nakhon Ratchasima 30000, Thailand

³School of Physics, Institute of Science, Suranaree University of Technology and Synchrotron Light Research Institute (Public Organization), Nakhon Ratchasima 30000, Thailand

Correspondence should be addressed to C. Sirisathitkul, schitnar@wu.ac.th

Received 30 May 2011; Accepted 1 July 2011

Academic Editor: Linbao Luo

Copyright © 2012 K. Chokprasombat et al. This is an open access article distributed under the Creative Commons Attribution License, which permits unrestricted use, distribution, and reproduction in any medium, provided the original work is properly cited.

The synchrotron X-ray absorption technique was used to complement electron microscopy in the investigation of nanoparticles synthesized from the coreduction of iron acetylacetonate, Fe(acac)₃ and platinum acetylacetonate, Pt(acac)₂. A much higher Pt composition than Fe leads to an extended X-ray absorption fine structure (EXAFS) spectrum for the sample that differs from that of fcc FePt nanoparticles. Most importantly, X-ray absorption near-edge structure (XANES) spectra clearly indicate the existence of α -Fe₂O₃ and Pt metal. Since these monodisperse nanoparticles have a diameter of around 4 nm and tend to self-assemble into hexagonal arrangements, they can be modeled as Pt-rich cores with an α -Fe₂O₃ shell stabilized by organic surfactants.

1. Introduction

Iron-platinum (FePt) nanoparticles are a prime candidate for the next generation of ultrahigh density recording materials [1]. Whereas other magnetic materials become hysteresis-free superparamagnetic particles when their sizes are below 10 nm, FePt nanoparticles of these sizes still exhibit ferromagnetism which is a requirement for nonvolatile recording [2]. To obtain substantial magnetic anisotropy for recording applications, not only the size but also the composition and local structure have to be controlled. It has been shown that as-synthesized FePt exhibits a chemically disordered fcc phase and is superparamagnetic but can be transformed into the ferromagnetic fct structure after heat treatment. In this fct arrangement, Fe and Pt atoms are in alternate planes with a balanced atomic ratio [3].

The synthesis of FePt nanoparticles conventionally uses the thermal decomposition of iron pentacarbonyl, Fe(CO)₅ [3]. Since this starting material is very toxic, the coreduction

of iron acetylacetonate, Fe(acac)₃ and platinum acetylacetonate, Pt(acac)₂ has been studied as a green alternative [4–7]. Metal acetylacetonates are universally regarded as versatile and nontoxic precursors in the synthesis of transition metal oxide nanoparticles [8]. However, the control of the composition and local structure of the FePt product from these starting materials still remain the subject of study. Commonly, the phase is identified by X-ray diffraction (XRD). The local composition can be obtained by energy dispersive spectroscopy (EDS) whereas the global composition is averaged by inductively coupled plasma-optical emission spectroscopy (ICP-OES).

In the case of the nanoparticles synthesized from the reaction between Fe(acac)₃ and Pt(acac)₂ and stabilized by organic surfactants, several possible core-shell structures may be obtained. The configuration gets more complicated when the ratio between Fe and Pt is highly unbalanced or a significant amount of oxygen is present. As a result, the conclusion about the local structure cannot be reached solely

by using conventional characterization techniques. X-ray absorption spectroscopy offers a unique opportunity to shine light on local structures and complement the information on composition and phase. From X-ray absorption spectra, Shinoda et al. concluded that different synthetic conditions led to nanoparticles of varying structures including a Pt-rich FePt core with an Fe-rich amorphous shell [9]. Huang et al. studied the shift in absorption peaks as a function of thermal treatments [10] and copper additions [11]. In addition to X-ray absorption studies of FePt, Antoniak et al. demonstrated that the technique was also useful in the case of iron oxide [12]. Since we are interested in using X-ray absorption from a synchrotron radiation source to probe such nanoparticles, self-assembled nanoparticles from metal acetylacetonate precursors are used as the case study in this work. Similar studies could then be extended to other related structures including those iron oxide-coated Pt nanoparticles [13].

2. Experimental

2.1. General. $\text{Fe}(\text{acac})_3$ (99.99%), $\text{Pt}(\text{acac})_2$ (97%), oleic acid (90%), oleylamine (70%) were obtained from Fluka Chemical Company and used as received. Benzyl ether was degassed for 15 min before use. Other AR grade organic solvents used for purification (e.g., hexane and absolute ethanol) were used as purchased. All manipulations were performed under dry nitrogen (N_2) using standard Schlenk line techniques.

2.2. Nanoparticles Preparation. A mixture of 0.5 mmol $\text{Pt}(\text{acac})_2$ and 0.5 mmol $\text{Fe}(\text{acac})_3$ was added in a 100 mL Schlenk flask filled with 20 mL benzyl ether. Oxygen was removed from the reaction flask *in vacuo* before being filled with N_2 . Once the solution reached 120°C, 5.0 mmol oleic acid and 5.0 mmol oleylamine as surfactants were added, and the solution was then heated to 210°C and kept at that temperature for 30 min. The black solution was refluxed at 300°C for 30 min then cooled to room temperature under N_2 . The particles were precipitated by addition of ethanol and then isolated by centrifugation. The obtained precipitate was redispersed in ethanol, followed by centrifugation. This washing procedure was repeated three times. Then, the washed particles were dispersed in hexane with a small amount (*ca.* 0.05 mL) of oleic acid and oleylamine, followed by bubbling with N_2 to remove O_2 . The colloid was stored in glass bottles in a refrigerator at 4°C.

2.3. Characterization Methods. For characterization, samples were prepared by depositing the colloid on solid substrates and evaporating the solvent at room temperature. The morphology of the products was examined by transmission electron microscopy (TEM) and the elemental composition was probed by EDS. X-ray absorption spectroscopy was obtained using synchrotron radiation at BL-8, Synchrotron Light Research Institute, Thailand. The X-ray absorption near-edge structure (XANES) and extended X-ray absorption fine structure (EXAFS) measurements of the Fe *K*-edge and Pt *M*₅-edge were performed in the transmission mode with an electron energy of 1.2 GeV. The spectra were collected

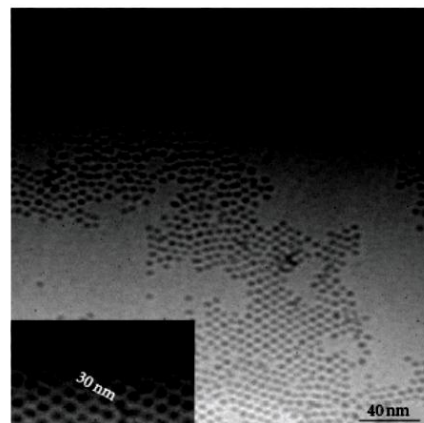


FIGURE 1: TEM images of synthesized nanoparticles.

at ambient temperature with a germanium(111) double crystal monochromator and recorded after performing an energy calibration. To increase the count rate, the ionization chamber was filled with argon gas. The storage ring was running at an energy of 1.22 GeV with electron currents between 140 mA and 80 mA.

3. Results and Discussion

The as-synthesized spherical nanoparticles in Figure 1 show a tendency to self-assemble into a hexagonal pattern. The higher magnification image in the inset reveals that these monodisperse particles have an approximate diameter of 4 nm and interparticle spacing is around 2 nm. This agrees to the observation by Nakaya et al. that such metal core dimensions and surfactants lead to a hexagonal assembly whereas larger nanoparticles (around 6 nm) tend to self-assemble into square patterns [5]. Elemental compositions of the colloid deposits by EDS analysis are 74.93% Pt, 8.24% Fe, and 16.83% O. Even though the molar ratio of Fe:Pt sources is 1:1 and a high boiling point solvent combines with high surfactants: metal ratio, Pt rich nanoparticles are still obtained rather than an ideal 1:1 stoichiometric FePt nanoparticles. This can be understood by the hetero-coagulation model recently proposed by Beck et al. for the reaction between metal acetylacetonates [14]. In contrast to the binary nucleation model in which Fe-rich particles from the decomposition of $\text{Fe}(\text{CO})_5$ occur simultaneously with Pt-rich particles [3], $\text{Fe}(\text{acac})_3$ is harder to reduce than $\text{Pt}(\text{acac})_2$, and this leads to the intermediate products of Pt-rich nuclei with the deposition of iron oxide on their surface. These iron oxides are then reduced to Fe atoms by a CO-spillover process on surface of the Pt nuclei, and the Fe atoms diffuse into the Pt-rich nuclei at high temperatures. It follows that the reduction of iron oxides is more pronounced in the case of smaller Pt nuclei (larger surface area). The composition of nanoparticles from this mechanism is

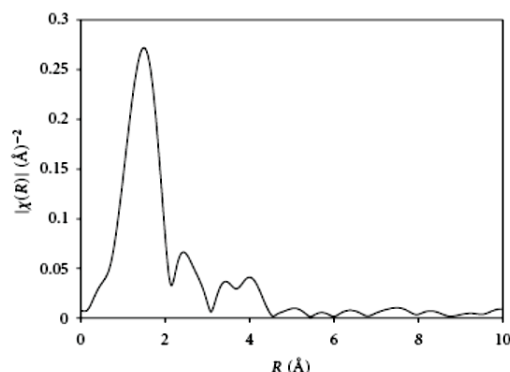


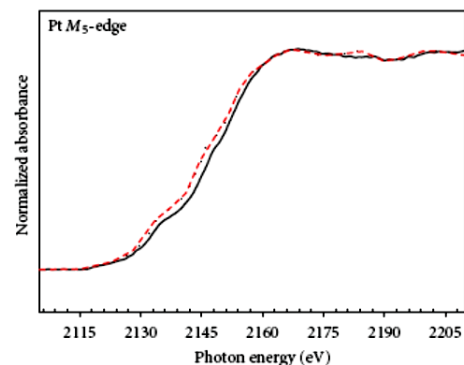
FIGURE 2: Fourier transform of Fe *K*-edge EXAFS spectrum of nanoparticles.

then sensitive to the reflux conditions as well as the amount of surfactants. Excessive amount of surfactants leads to particles of larger size but lowers the effectiveness of the reduction process. Moreover, the excess surfactants may impede the reduction process on the particle surface.

Fourier transformation of the EXAFS spectrum of the Fe *K*-edge is shown in Figure 2. The highest peak between 0.1 and 0.2 nm corresponds to nearest neighboring Fe-O correlation which is different from the Fe-Pt profile shown in work reported by Shinoda et al. [9]. The Fe *K*-edge and Pt *M*₅-edge XANES spectra of the nanoparticles are shown in Figure 3. Between 21002–2200 eV in Figure 3(a), the profile fits well with that of the Pt standard, indicating that the sample contains Pt metal. In contrast, the XANES spectrum between 7000 and 7200 eV of the Fe *K*-edge does not match that of the Fe standard. Instead, as shown in Figure 3(b), it resembles that of hematite (α -Fe₂O₃) which is the most thermodynamically stable iron oxide at ambient conditions. XANES has the advantage of distinguishing the different valence states of Fe as is evident in this case because the different forms of iron oxide nanoparticles are difficult to differentiate by other techniques [12]. The results from X-ray absorption spectroscopy suggest that the sample contains mostly Pt metal and α -Fe₂O₃ with small amount of Fe metal. Since these nanoparticles have rather uniform size distribution and self-assembled arrangement, it is likely that Pt-rich cores with α -Fe₂O₃ shells are formed. This core-shell structure is surrounded by oleic acid and oleylamine. Although these surfactants are not detected by TEM or X-ray absorption spectroscopy, the model is confirmed by the stability of the nanoparticles in hexane without agglomeration and sedimentation over a long period of time.

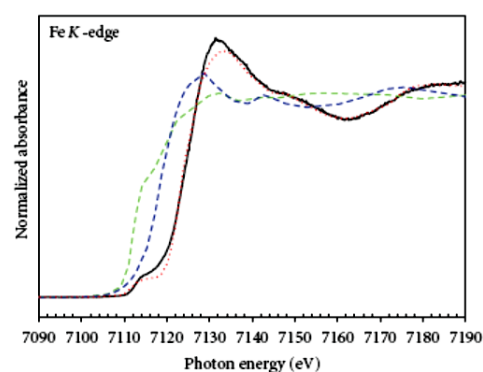
4. Conclusion

Self-assembled monodisperse nanoparticles were synthesized from the coreduction of Fe(acac)₃ and Pt(acac)₂ in the presence of benzyl ether and organic surfactants. With a composition of Fe lower than 10%, X-ray absorption spectra are



--- Pt foil
— Sample_S4

(a)



--- Fe foil
--- FeO
... Fe₂O₃
— Sample_S4

(b)

FIGURE 3: XANES spectra of nanoparticles (Sample_S4) for (a) Pt *M*₅-edge compared to Pt foil and (b) Fe *K*-edge compared to Fe foil, FeO, and Fe₂O₃.

consistent with a Pt-rich core with a α -Fe₂O₃ shell over an Fe-Pt alloy consistent with a heterocoagulation mechanism in a modified polyol process. It was demonstrated that the core shell can be modeled from the study by X-ray absorption spectroscopy and electron microscopy.

Acknowledgments

This project is financially supported by the National Electronics and Computer Technology Center, National Science and Technology Development Agency and Industry/University Cooperative Research Center (I/UCRC) in HDD Component, the Faculty of Engineering, Khon Kaen University. Support from Seagate (Thailand) and the proof-reading by Dr. D. James Harding are gratefully acknowledged.

References

- [1] B. D. Terris and T. Thomson, "Nanofabricated and self-assembled magnetic structures as data storage media," *Journal of Physics D*, vol. 38, no. 12, pp. R199–R222, 2005.
- [2] H. W. Zhang, Y. Liu, and S. H. Sun, "Synthesis and assembly of magnetic nanoparticles for information and energy storage applications," *Frontiers of Physics in China*, vol. 5, no. 4, pp. 347–356, 2010.
- [3] S. Sun, "Recent advances in chemical synthesis, self-assembly, and applications of FePt nanoparticles," *Advanced Materials*, vol. 18, no. 4, pp. 393–403, 2006.
- [4] V. Nandwana, K. E. Elkins, and J. P. Liu, "Magnetic hardening in ultrafine FePt nanoparticle assembled films," *Nanotechnology*, vol. 16, no. 12, pp. 2823–2826, 2005.
- [5] M. Nakaya, M. Kanehara, and T. Teranishi, "One-pot synthesis of large FePt nanoparticles from metal salts and their thermal stability," *Langmuir*, vol. 22, no. 8, pp. 3485–3487, 2006.
- [6] C. Liu, X. Wu, T. Klemmer et al., "Polyol process synthesis of monodispersed FePt nanoparticles," *Journal of Physical Chemistry B*, vol. 108, no. 20, pp. 6121–6123, 2004.
- [7] K. E. Elkins, T. S. Vedantam, J. P. Liu et al., "Ultrafine FePt nanoparticles prepared by the chemical reduction method," *Nano Letters*, vol. 3, no. 12, pp. 1647–1649, 2003.
- [8] A. L. Willis, Z. Y. Chen, J. Q. He, Y. M. Zhu, N. J. Turro, and S. O'Brien, "Metal acetylacetonates as general precursors for the synthesis of early transition metal oxide nanomaterials," *Journal of Nanomaterials*, vol. 2011, Article ID 525967, 5 pages, 2011.
- [9] K. Shinoda, K. Sato, B. Jeyadevan, K. Tohji, and S. Suzuki, "Local structural studies of directly synthesized L10 FePt nanoparticles by using XRD, XAS and SAXS," *Journal of Magnetism and Magnetic Materials*, vol. 310, no. 2, pp. 2387–2389, 2007.
- [10] T. W. Huang, Y. H. Huang, T. H. Tu, and C. H. Lee, "X-ray diffraction and absorption spectroscopy studies of the structure of self-assembled FePt nanoparticles during annealing," *Journal of Magnetism and Magnetic Materials*, vol. 282, no. S1, pp. 127–130, 2004.
- [11] T. W. Huang, T. H. Tu, Y. H. Huang, C. H. Lee, and C. M. Lin, "X-ray scattering and absorption spectroscopy study of the order-disorder transition of $(\text{FePt})_{1-x}\text{Cu}_x$ nanoparticles," *IEEE Transactions on Magnetics*, vol. 41, no. 2, pp. 941–943, 2005.
- [12] C. Antoniak, A. Warland, M. Darbandi et al., "X-ray absorption measurements on nanoparticle systems: self-assembled arrays and dispersions," *Journal of Physics D*, vol. 43, no. 47, Article ID 474007, 8 pages, 2010.
- [13] H. He and C. Gao, "Synthesis of $\text{Fe}_3\text{O}_4/\text{Pt}$ nanoparticles decorated carbon nanotubes and their use as magnetically recyclable catalysts," *Journal of Nanomaterials*, vol. 2011, Article ID 193510, 10 pages, 2011.
- [14] W. Beck Jr., C. G. S. Souza, T. L. Silva, M. Jafelicci Jr., and L. C. Varanda, "Formation mechanism via a heterocoagulation approach of FePt nanoparticles using the modified polyol process," *Journal of Physical Chemistry C*, vol. 115, no. 21, pp. 10475–10482, 2011.

Magnetolectric Properties of Cu- and Mn-Doped $0.75\text{BiFeO}_3\text{-}0.25\text{BaTiO}_3$ Multiferroic Ceramics

S. CHANDARAK,¹ S. POJPRAPAI,¹ S. SRILOMSAK,¹
P. JANTARATANA,² S. RUJIRAWAT,^{3,4} AND R. YIMNIRUN^{4,*}

¹School of Ceramic Engineering, Suranaree University of Technology,
Nakhon Ratchasima 30000, Thailand

²Department of Physics, Kasetsart University, Bangkok 10900, Thailand

³Thailand Center of Excellence in Physics (THEP Center) Commission on
Higher Education, Bangkok 10400, Thailand

⁴School of Physics, Institute of Science, Suranaree University of Technology,
and Synchrotron Light Research Institute, Nakhon Ratchasima 30000, Thailand

In this study, $0.75\text{BiFeO}_3\text{-}0.25\text{BaTiO}_3$ ceramics doped with Mn and Cu (1, 2, 3, 4 and 5 mol%) have been fabricated with an effective solid-state reaction method developed for high purity ceramics. Attention has been focused on relationships between sintering conditions, phase formation, density, and magnetolectric properties of the sintered ceramics. It was found that Cu and Mn doping affected significantly the dielectric, ferroelectric, ferromagnetic and magnetolectric properties of these ceramics. At certain level of addition, both Mn and Cu doping were found to enhance the ferroelectric and ferromagnetic characteristics of the $\text{BiFeO}_3\text{-BaTiO}_3$ multiferroic ceramics. Finally, magnetolectric properties of the ceramics were also determined. The addition of the Cu and Mn ions was found to noticeably improve the magnetolectric properties of the ceramics.

Keywords ME effect; BF-BT; Mn and Cu Doping

Introduction

Magnetolectricity is the production of an electric field when we applied magnetic field and vice versa. Magnetolectric (ME) effect is an induced dielectric polarization by external magnetic field or an induced magnetization by external electric field [1]. The materials that show ME effect are named magnetolectric materials, and considered to be the component of electronic devices [2]. ME effects were first observed in single crystals and a lot of ME materials have been discovered in the last three decades. ME effects of single crystals occur due to the local interaction between the ordered magnetic and ferroelectric sub-lattices [3, 4] Since device applications of the single phase have not been successful, many researchers have mostly studied the magnetolectric composite materials because they are a combination of at least two chemically distinct materials with an interface separating the components; the combination has its own distinctive properties [5–8]. Moreover,

multiferroic materials; i.e. BF, showing simultaneous electrical and magnetic orderings, have gained increasing attention due to their technological and fundamental importance [9]. Due to the magnetoelectricity of these materials, the magnetic order can be controlled by electric fields or vice versa, are being considered to host large number of potential applications in storage media, spintronic devices, sensors and actuators [10]. BF is the most extensively investigated multiferroics exhibiting ME effect at room temperature [11]. In BF, 6s lone pair electrons of Bi contribute to the ferroelectricity while the partially filled d orbital of Fe is responsible for the magnetism [9–11]. BF is a representative material that shows both the ferroelectric (T_C : 1103 K) and antiferromagnetic (T_N : 643 K) characteristics [12–14]. However, BF has low resistivity leading to lower ME effect [5]. On the other hand, ferroelectric BaTiO₃ (BT) material shows high resistivity. Solid solutions of BF-BT are expected to increase the resistivity; hence better applicability can be realized. From our previous study, it was found that when 0.75BF-0.25BT system was doped with Mn and Cu (0.75BF-0.25 is the morphotropic phase boundary (MPB) of this system) higher resistivity, as well as improved dielectric, ferroelectric and ferromagnetic properties, could be obtained [15]. In this study, the ME effect of 0.75BF-0.25BT system doped with Mn and Cu was investigated.

Experimental Procedure

For this study, 0.75BiFeO₃–0.25BaTiO₃ (0.75BF-0.25BT) system doped with Mn and Cu (0, 1, 2, 3, 4 and 5 mol%) were prepared by using the solid-state reaction method. The Mn- and Cu-doped 0.75BF-0.25BT systems were calculated with nominal Bi_{0.75}Ba_{0.25}(Fe,Ti)_(1-x)(Mn)_xO₃ and Bi_{0.75}Ba_{0.25}(Fe,Ti)_(1-x)(Cu)_xO₃ compositions, these system based on the B-site substitution assumption. Starting materials BaCO₃, TiO₂, Bi₂O₃, Fe₂O₃, MnO₂ and CuO powders were mixed by vibro-milling method for 30 min. All mixtures were dried and calcined at 900°C for 5 h with heating/cooling rates of 5°C/min. The calcined powders were pressed as disk under a pressure of 130 MPa and then sintered at 975°C for 2 h in the air with heating/cooling rates of 5°C/min. The room temperature ME effect was then measured on the sintered specimens, as shown in Fig. 1. In this work, the magnetoelectric coefficient in 0.75BF-0.25BT doped Mn and Cu ceramics was determined using dynamic lock-in technique to evidence ME coupling behavior. The measurement was performed at constant frequency of 1 kHz and constant bias ac magnetic field at 10 Oe. The static ME coefficient was measured as a function of dc magnetic field (H_{dc}) up to 4.2 kOe at room temperature. In this study, ME coefficient was calculated by equation (1)

$$\text{ME coefficient} = V \text{ (volt)/thickness (mm)} * H_{dc} \text{ (Oe)} \quad (1)$$

Results and Discussion

The changes in the ME coefficient of Bi_{0.75}Ba_{0.25}(Fe,Ti)_(1-x)(Cu)_xO₃ ceramics (with $x = 0, 1, 2, 3, 4,$ and 5 mol%) with H_{dc} can be divided that into 3 groups as shown in Fig. 2(a). In the first group, 0.75BF-0.25BT (undoped), ME coefficient increases with increasing of H_{dc} . ME coefficient value increases continuously to 0.0008 V/cmOe with H_{dc} 1547 Oe, then ME coefficient value decreases with further increase of H_{dc} . The second group, 1 mol% Cu 0.75BF-0.25BT shows rather stable ME coefficient value with increasing H_{dc} . The third group, with addition of 2–5 mol% Cu into 0.75BF-0.25BT, the ME coefficient

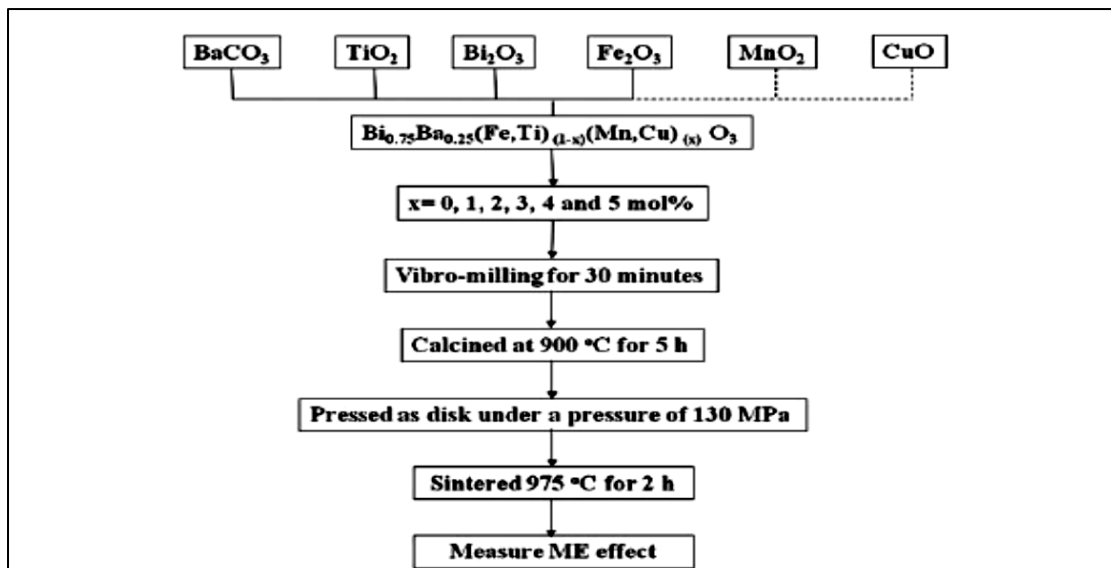
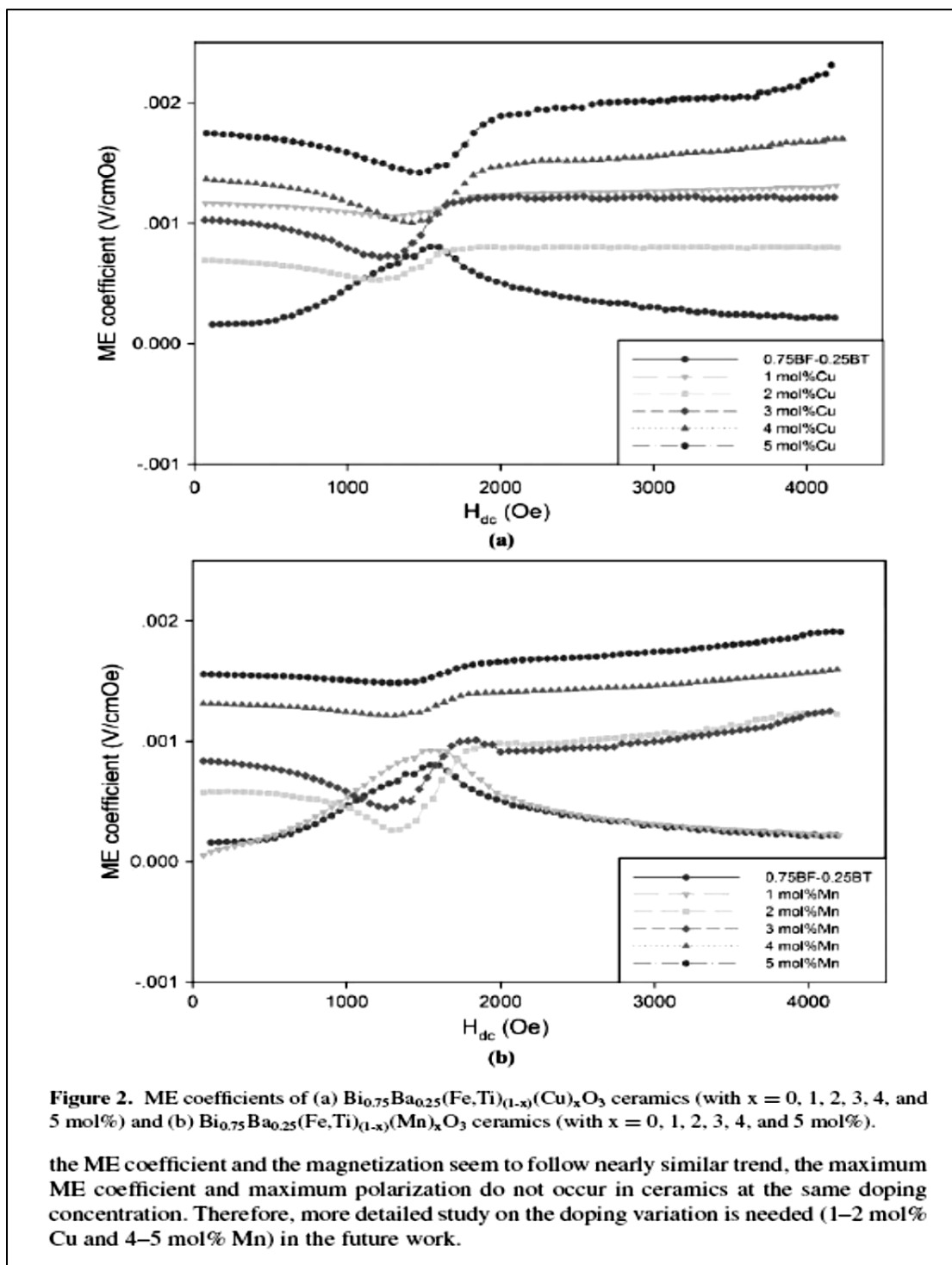


Figure 1. Schematic diagram for preparation of $\text{Bi}_{0.75}\text{Ba}_{0.25}(\text{Fe,Ti})_{1-x}(\text{Mn,Cu})_x\text{O}_3$ and $\text{Bi}_{0.75}\text{Ba}_{0.25}(\text{Fe,Ti})_{1-x}(\text{Cu})_x\text{O}_3$ ($x = 0, 1, 2, 3, 4$ and 5 mol%) ceramics.

values increase with Cu contents. In these compositions, the ME coefficient decreases continuously to 0.0005, 0.0007, 0.0010 and 0.0014, in V/cmOe units, with increasing to H_{dc} 1214, 1323, 1424 and 1471 Oe for 2 to 5 mol% Cu doped 0.75BF-0.25BT ceramics, respectively, and the ME coefficients increase continuously with H_{dc} after the on-set field mentioned above.

Similarly, the changes in the ME coefficient of $\text{Bi}_{0.75}\text{Ba}_{0.25}(\text{Fe,Ti})_{1-x}(\text{Mn})_x\text{O}_3$ ceramics (with $x = 0, 1, 2, 3, 4$, and 5 mol%) with H_{dc} can also be divided that into 3 groups as shown in Fig. 2(b). The first group, undoped and 1 mol% Mn 0.75BF-0.25BT samples shows increasing ME coefficient value, similar to the undoped BF-BT as shown in Fig. 2(a) and the ME coefficient value of 1 mol% Mn-doped 0.75BF-0.25BT sample shows continuous increase to 0.0009 V/cmOe at H_{dc} 1546 Oe, and then decreases with further increase in H_{dc} . In the second group, 4 and 5 mol% Mn-doped 0.75BF-0.25BT ceramics show relatively stable ME coefficient value with increase H_{dc} . While in the third group, 2 and 3 mol% addition of Mn, the ME coefficients decrease with Mn content. It should be mentioned here that the sudden changes in the ME coefficients occur with application of H_{dc} around 1 to 1.5 kOe in all ceramics.

Figure 3 shows the variation in the ME coefficient with Cu and Mn contents, as compared to polarization and magnetization values. It can be seen clearly that the ME coefficient value first increases with addition of 1 mol% Cu or Mn into 0.75BF-0.25BT ceramic, and then drops to minimum with addition of to 2 mol% of Cu and Mn. Further addition of both the Cu and Mn results in a continuous increase in the ME coefficients. As shown in Fig. 3, 0.75BF-0.25BT ceramics with 2 mol% Cu and 5 mol% Mn show the highest and the polarization values of 34 and 11 $\mu\text{C}/\text{cm}^2$, and the magnetization values are 0.3078 and 0.0020 emu/g, respectively. The trend for the polarization and magnetization values differs slightly from the ME coefficient. In light of these results, it is seen that, while



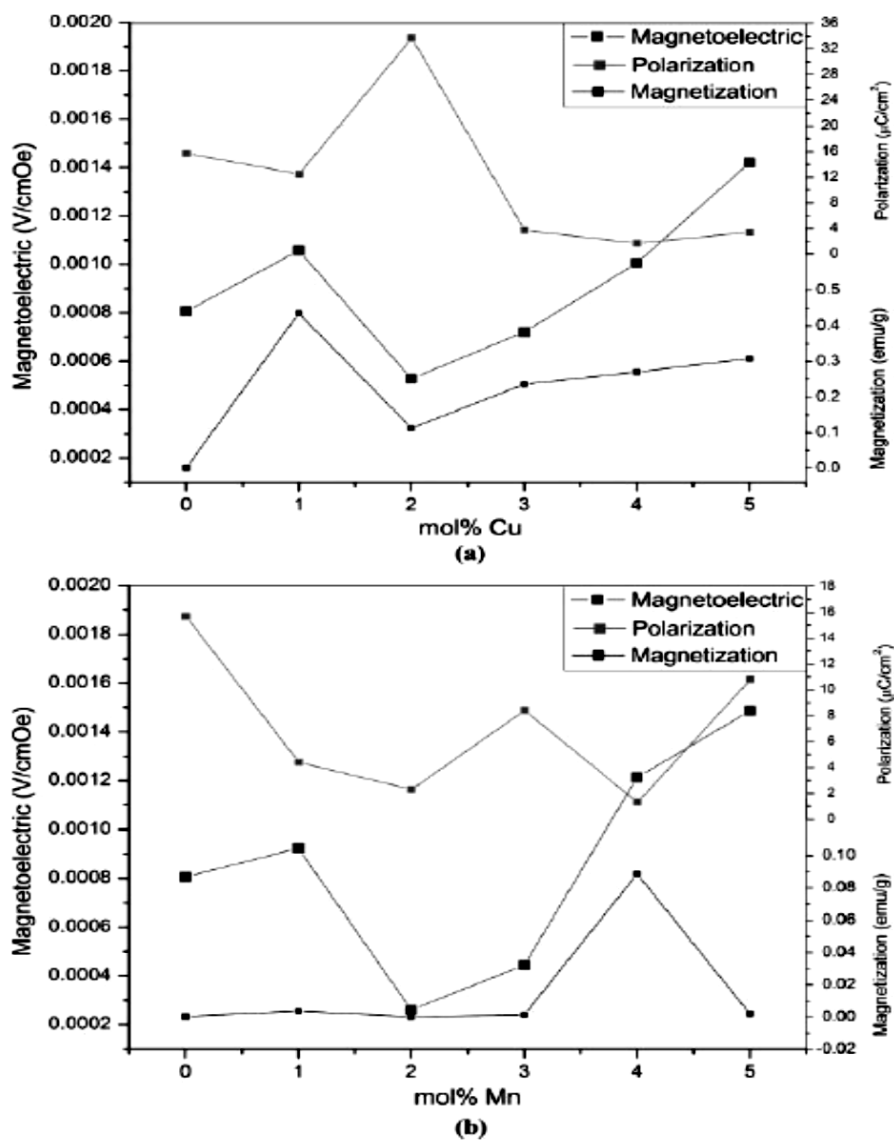


Figure 3. ME coefficient, polarization and magnetization values as a function of of Cu and Mn contents in (a) $\text{Bi}_{0.75}\text{Ba}_{0.25}(\text{Fe,Ti})_{(1-x)}(\text{Cu})_x\text{O}_3$ and (b) $\text{Bi}_{0.75}\text{Ba}_{0.25}(\text{Fe,Ti})_{(1-x)}(\text{Mn})_x\text{O}_3$ ceramics.

Conclusions

In this study, the ME coefficient of $\text{Bi}_{0.75}\text{Ba}_{0.25}(\text{Fe,Ti})_{(1-x)}(\text{Cu})_x\text{O}_3$ and $\text{Bi}_{0.75}\text{Ba}_{0.25}(\text{Fe,Ti})_{(1-x)}(\text{Mn})_x\text{O}_3$ ceramics (with $x = 0, 1, 2, 3, 4,$ and 5 mol%) were determined. The compositions with 5 mol% Cu and Mn addition; i.e., $\text{Bi}_{0.75}\text{Ba}_{0.25}(\text{Fe,Ti})_{(0.95)}(\text{Cu})_{0.05}\text{O}_3$ and $\text{Bi}_{0.75}\text{Ba}_{0.25}(\text{Fe,Ti})_{(0.95)}(\text{Mn})_{0.05}\text{O}_3$, exhibited the highest ME coefficient due to the ion

concentrations of Cu and Mn were found to significantly improve the magnetoelectric properties in these ceramics. Nevertheless, more detailed study on the effect of these dopants on the ferroelectric, ferromagnetic and magnetoelectric properties is still needed to optimize the application of this ceramic system.

Acknowledgments

This work was financially supported by the Industry/University Cooperative Research Center (I/UCRC) in HDD Component, the Faculty of Engineering, Khon Kaen University and National Electronics and Computer Technology Center, National Science and Technology Development Agency (NSTDA). One of the authors (S.C.) is also thankful to the Synchrotron Light Research Institute (Public Organization) for PhD scholarship and to Suranaree University of Technology for additional support. Another author (S.R.) would also like to acknowledge the support by NANOTEC (Grant No.NN-B-22-DI2-20-51-09) and Thailand Research Fund (Grant No. RTA5280009).

References

1. C. W. Nan, Magnetoelectric effect in composite of piezoelectric and piezomagnetic phases. *Phy. Rev. B* **50**, 6082–6088 (1994).
2. Y. H. Tang, X. M. Chen, Y. J. Li, and X. H. Zheng, Dielectric and magnetoelectric characterization of $\text{CoFe}_2\text{O}_4/\text{Ba}_{0.55}\text{Sr}_{0.25}\text{Ca}_{0.2}\text{Nb}_2\text{O}_6$ composites. *Mater. Sci. Eng. B* **116**, 150–115 (2005).
3. J. Ryu, S. Priya, K. Uchino, and H. Kim, Magnetoelectric effect in composites of magnetostrictive and piezoelectric materials. *J. Electroceram.* **8**, 107–120 (2002).
4. S. Mazumder and G. S. Battacharyya, Magnetoelectric behavior in in situ grown piezoelectric and piezomagnetic composite-phase system. *Mater. Res. Bull.* **38**, 303–310 (2003).
5. D. R. Patil, S. A. Lokare, R. S. Devan, S. S. Chougule, Y. D. Kolekar, and B. K. Chougule, Dielectric properties and magnetoelectric effect of $(x)\text{NiFe}_2\text{O}_4 + (1-x)\text{Ba}_{0.8}\text{Sr}_{0.2}\text{TiO}_3$ composites. *J. Phys. Chem. Solids* **68**, 1522–1526 (2007).
6. R. S. Devan, Y. D. Kolekar, and B. K. Chougule, Magnetoelectric effect and electrical properties in $\text{BTO} + \text{Ni}_{0.93}\text{Co}_{0.02}\text{Cu}_{0.05}\text{Fe}_2\text{O}_4$ particulate composites. *J. Alloys Compd.* **461**, 678–683 (2008).
7. D. R. Patil, A. D. Sheikh, C. A. Watve, and B. K. Chougule, Magnetoelectric properties of ME particulate composites. *J. Mater. Sci.* **43**, 2708–2712 (2008).
8. H. Greve, E. Woltermann, H. J. Quenzer, B. Wagner, and E. Quandt, Giant magnetoelectric coefficients in $(\text{Fe}_{90}\text{Co}_{10})_{78}\text{Si}_{12}\text{B}_{10}\text{-AlN}$ thin film composites. *Appl. Phys. Lett.* **96**, 182501 (2010).
9. R. Ramesh and N. A. Spaldin, Multiferroics: progress and prospects in thin films. *Nat. Mater.* **6**, 21 (2007).
10. W. Erenstein, N. D. Mathur, and J. F. Scott, Multiferroic and magnetoelectric materials. *Nature* **442**, 759–65 (2006).
11. S. W. Cheong and M. Mostovoy, Multiferroics: A magnetic twist for ferroelectricity. *Nat. Mater.* **6**, 13–20 (2007).
12. C. Jae-wan, H. M. Jang, and K. Sang-Koog, A possible origin of ferromagnetism in epitaxial BiFeO_3 thin films. *J. Magn.* **11**(3), 108 (2006).
13. S. V. Kiselev, R. P. Ozarov, and G. S. Zhdanov, Detection of magnetic order in ferroelectric BiFeO_3 by neutron diffraction. *Sov. Phys. Dokl.* **7**, 742 (1963).
14. P. Fischer, M. Polomska, I. Sosnowska, and M. Szymanski, Temperature dependence of the crystal and magnetic structure of BiFeO_3 . *J. Phys. C: Solid State Phys.* **13**, 1931 (1980).
15. S. Chandarak, A. Ngamjarujana, S. Srilomsak, S. Rujirawat, and R. Yimnirun, Effects of Mn and Cu doping on electrical properties of $0.75\text{BiFeO}_3\text{-}0.25\text{BaTiO}_3$ ceramics. *Integrated Ferroelectrics* **114**, 100–107 (2010).

Dielectric Properties of BaTiO₃-Modified BiFeO₃ Ceramics

SUJITTRA CHANDARAK,^{1,*} ATHIPONG
NGAMJARUROJANA,² SUTHUM SRILOMSAK,¹
PITAK LAORATANAKUL,³ SAROJ RUJIRAWAT,^{4,5}
AND RATTIKORN YIMNIRUN⁵

¹School of Ceramic Engineering, Suranaree University of Technology, Nakhon Ratchasima 30000, Thailand

²Department of Physics and Materials Science, Chiang Mai University, Chiang Mai 50200, Thailand

³National Metals and Materials Technology Center (MTEC), Pathum Thani 10120, Thailand

⁴Synchrotron Light Research Institute (Public Organization), Nakhon Ratchasima 30000, Thailand

⁵School of Physics, Suranaree University of Technology, Nakhon Ratchasima 30000, Thailand

Multiferroic BiFeO₃ has attracted extensive interest due to its potential in several applications. However, pure-phase BiFeO₃ is very difficult to obtain. Hence, mixing BiFeO₃ with other ferroelectrics, such as BaTiO₃, is another approach to obtain materials with possible multiferroic properties. In this study, the BiFeO₃ was modified with addition of BaTiO₃ via a simple solid state reaction method. Dielectric properties of the BaTiO₃-modified BiFeO₃ ceramics were investigated over wide range of temperature and frequency. The results show that the (1-x)BiFeO₃-xBaTiO₃ ceramics with x = 0.1 and 0.2 exhibited large dielectric properties with giant-dielectric-like behavior. The dielectric properties were seen to improve with increasing BaTiO₃ content, with the highest dielectric constant ($\epsilon_r = 19000$) observed in 0.8BiFeO₃-0.2BaTiO₃ ceramic. The results were explained in terms of the pre-dominantly intrinsic BiFeO₃ giant-dielectric behavior as a result of Fe multivalent states, as well as a better grain packing density with increasing BaTiO₃ content.

Keywords Dielectric properties; BiFeO₃-BaTiO₃

I. Introduction

BiFeO₃ (BF) is the multiferroic material that shows both ferroelectric and (anti)ferromagnetic coexisting in perovskite structure at room temperature in the same phase [1]. BiFeO₃ shows ferroelectric (T_C) at 850°C and antiferromagnetic (T_N) at 370°C [2, 3]. Structure of BiFeO₃ is a rhombohedrally distorted perovskite structure [4]. The spontaneous polarization of BiFeO₃ single crystals has been reported to be 3.5 $\mu\text{C}/\text{cm}^2$ along

the $\langle 100 \rangle$ direction and $6.1 \mu\text{C}/\text{cm}^2$ along the $\langle 111 \rangle$ direction at 77 K [5]. However, the preparation of pure BiFeO_3 in a bulk form without traces of impurities has proven a difficult task.

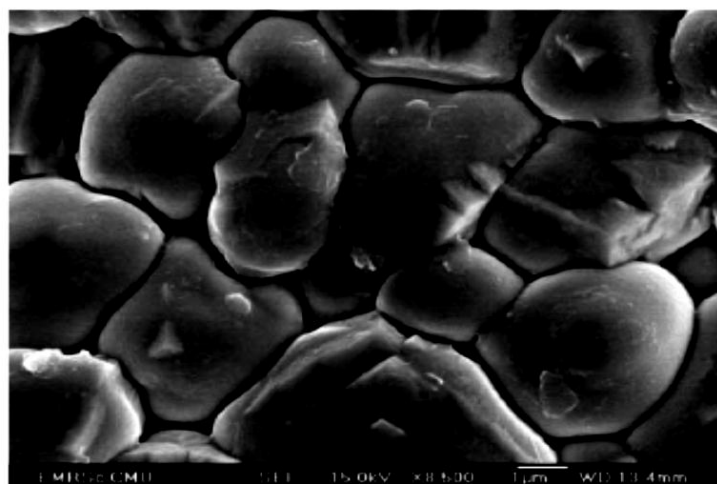
One of the approaches to obtain materials with multiferroic properties is to suitably mix different kinds of ferroic materials. Considering from a structural viewpoint, barium titanate (BaTiO_3 or BT) is one of very interesting and widely studied perovskite-based ferroelectric materials with excellent electrical properties. BaTiO_3 is a prototype ferroelectric material with several excellent ferroelectric properties (T_C : 120°C , P_S : $26 \mu\text{C}/\text{cm}^2$, and $\epsilon_r > 1000$) [6, 7]. Therefore, mixing two excellent prototypic ferroic materials with the same structure (perovskite structure: ABO_3) BaTiO_3 and BiFeO_3 is performed to improve electrical properties and to stabilize the multiferroic BiFeO_3 in the perovskite structure. Previous investigations [8, 9] have clearly emphasized the importance of the matter. In this work, BiFeO_3 - BaTiO_3 ceramics were prepared by the solid-state reaction method. Dielectric properties of BaTiO_3 -modified BiFeO_3 ceramics were investigated over wide range of temperature and frequency.

II. Experimental Procedure

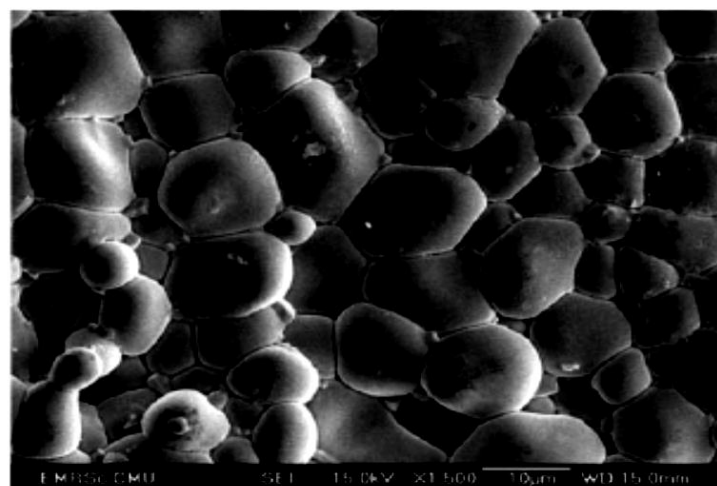
The $(1-x)\text{BiFeO}_3$ - $x\text{BaTiO}_3$ ($x = 0.1$ and 0.2) ceramics were prepared by a solid state reaction by using vibo-milling and firing techniques. The mixed powders were calcined at 900°C for 5 h at a rate of $5^\circ\text{C}/\text{min}$. The calcined samples were ground and pressed into pellets, with polyvinyl alcohol as the binder. The powder compacts were subsequently sintered at 1025°C for 2 h at heating and cooling rates of $5^\circ\text{C}/\text{min}$. XRD patterns showed that the sintered specimens contained the perovskite single phase, without any second phase like pyrochlore. The microstructural development was characterized using a scanning electron microscopy (SEM; JEOL JSM-840A), equipped with an energy dispersive X-ray (EDX) analyzer. The details for the preparation processes and the characterization can be found elsewhere [10, 11]. The low-field dielectric properties were measured by a computer-controlled impedance meter (Hewlett Packard 4194A) equipped with an environmental chamber (DELTA 9023) in frequency ranging from 100 Hz to 1 MHz and temperature ranging from -70 to 200°C . The dielectric constant (ϵ_r) was then calculated from a parallel-plate capacitor equation, e.g. $\epsilon_r = Cd/\epsilon_0A$, where C is the capacitance of the specimens, d and A are the thickness and the area of the electrode, respectively and ϵ_0 is the dielectric permittivity of vacuum (8.854×10^{-12} F/m).

III. Results and Discussion

SEM micrographs of $(1-x)\text{BiFeO}_3$ - $x\text{BaTiO}_3$ ($x = 0.1$ and 0.2) ceramics sintered at 1025°C are compared in Fig. 1. In general, highly dense and homogeneous microstructures are observed for the ceramics. The average grain sizes of 3.06 and $6.70 \mu\text{m}$ are determined for 0.9BiFeO_3 - 0.1BaTiO_3 and 0.8BiFeO_3 - 0.2BaTiO_3 ceramics, respectively. Moreover, a degree of grain close-packing microstructures tends to increase with BT content, likely caused by a noticeable size difference between the grains, as observed in Fig. 1(b). A relatively poor densification observed in 0.9BiFeO_3 - 0.1BaTiO_3 ceramic Fig. 1(a) could be due to sintering conditions which may not be optimized for the ceramic composition. These factors, which are strongly influenced by the sintering conditions, have an important effect on the dielectric properties of the ceramics, which will be discussed in the subsequent paragraphs.



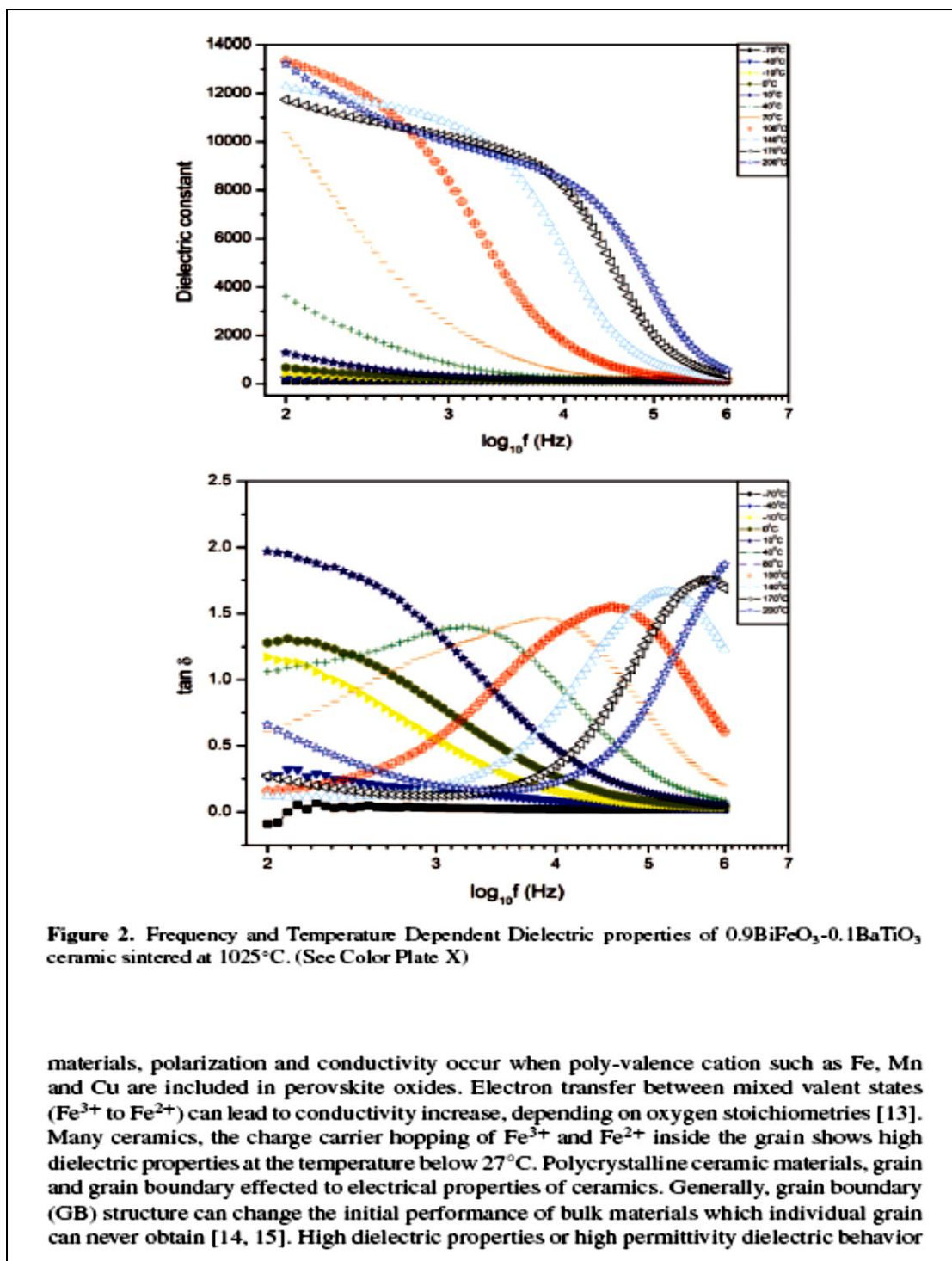
(a)



(b)

Figure 1. SEM micrographs of $(1-x)\text{BiFeO}_3-x\text{BaTiO}_3$ ceramics: (a) $x = 0.1$ and (b) $x = 0.2$ (sintered at 1025°C).

The dielectric properties, e.g. dielectric constant (ϵ_r) and dielectric loss tangent ($\tan\delta$), are measured as functions of both temperature and frequency, as shown in Figs. 2 and 3 for $0.9\text{BiFeO}_3-0.1\text{BaTiO}_3$ and $0.8\text{BiFeO}_3-0.2\text{BaTiO}_3$ ceramics, respectively. It should first be noticed that the dielectric properties patterns, both ϵ_r and $\tan\delta$, are similar for both ceramics. Even more interestingly, these changes of the dielectric properties with temperature and frequency of this binary system of $\text{BiFeO}_3\text{-BaTiO}_3$ ceramics resemble those of the giant-dielectric behavior observed in the pure BiFeO_3 ceramic reported earlier [12]. The observed giant dielectric behavior can be explained as follows. In the perovskite



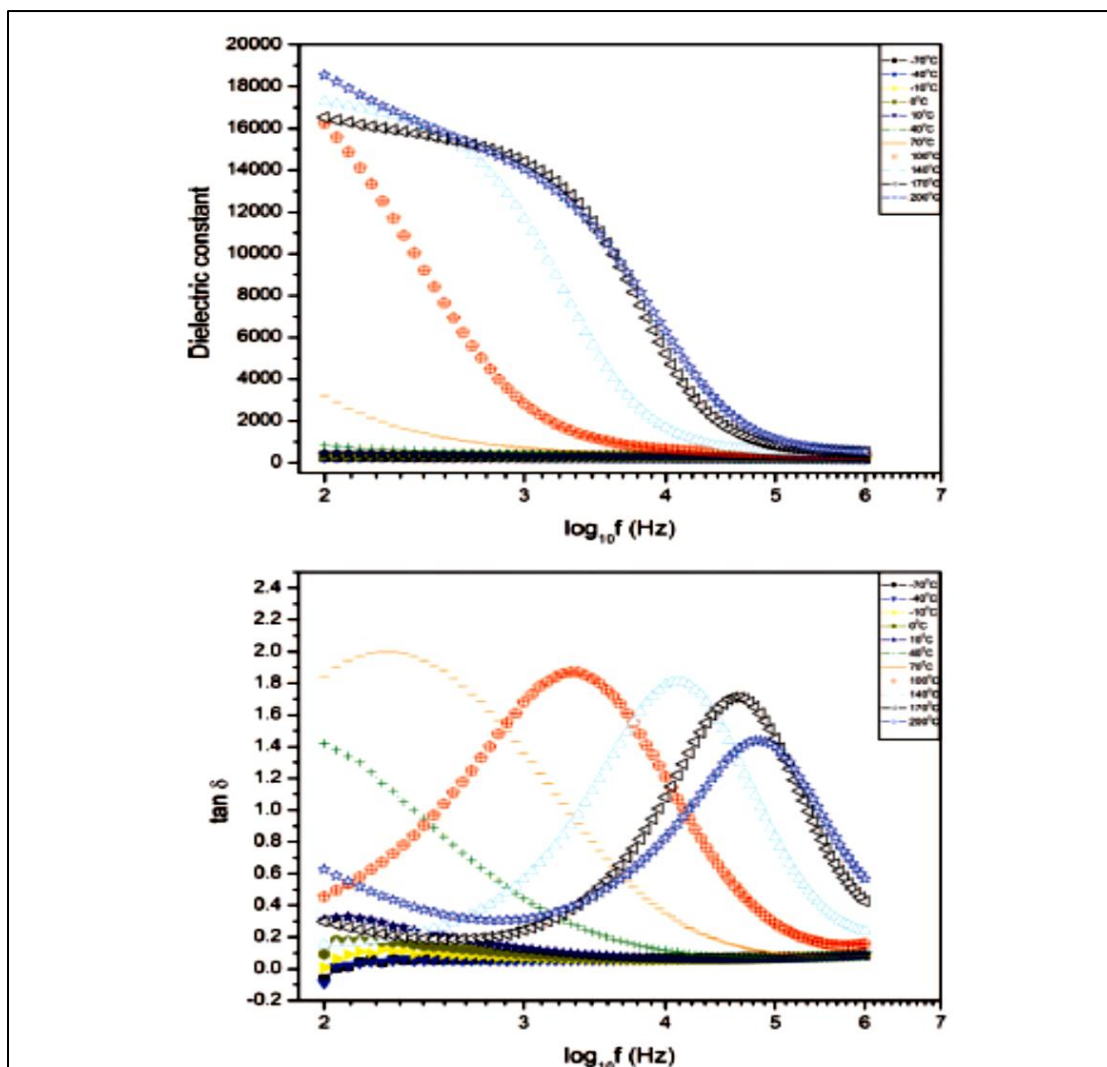


Figure 3. Frequency and Temperature Dependent Dielectric properties of $0.8\text{BiFeO}_3\text{-}0.2\text{BaTiO}_3$ ceramic sintered at 1025°C . (See Color Plate XI)

observe in many perovskite materials can also be greatly affected by the existence of GBs in the microstructure, at which an interfacial polarization could be induced [16–21].

Furthermore, a decrease of the dielectric properties with increasing frequency is caused by the inability of various polarization contributions to follow the change of the applied electric field, leading to lower dielectric constants and loss at higher frequencies. Nevertheless, high dielectric loss tangent ($\tan \delta$) observed in $\text{BiFeO}_3\text{-BaTiO}_3$ ceramics is likely due to high BiFeO_3 content in the ceramics which possesses higher charge carrier hopping of Fe^{3+} and Fe^{2+} inside the ceramic grain. This dominant factor clearly controls the

dielectric characteristics of the ceramics, rather than the highly insulative behavior of the BaTiO₃ constituent. Finally, it should be noted that the dielectric properties, particularly the dielectric constant, are seen to improve with increasing BT content, as displayed in Fig. 2(a) and 3(a). It is seen that the highest dielectric constant of 13500 and 19000 are determined for 0.9BiFeO₃-0.1BaTiO₃ and 0.8BiFeO₃-0.2BaTiO₃ ceramics, respectively. This is believed to be caused by the improved densification in the ceramics with higher BT content as discussed earlier.

IV. Conclusion

The BiFeO₃ was modified with addition of BaTiO₃ via a simple solid state reaction method. Dielectric properties of the BaTiO₃-modified BiFeO₃ ceramics were investigated over wide range of temperature and frequency. The results show that the (1-x)BiFeO₃-xBaTiO₃ ceramics with x = 0.1 and 0.2 exhibited large dielectric properties with giant-dielectric-like behavior. The dielectric properties were seen to improve with increasing BaTiO₃ content, with the highest dielectric constant ($\epsilon_r = 19000$) observed in 0.8BiFeO₃-0.2BaTiO₃ ceramic. The results were explained in terms of the pre-dominantly intrinsic BiFeO₃ giant-dielectric behavior as a result of Fe multivalent states, as well as a better grain packing density with increasing BaTiO₃ content. Most importantly, this study reveals that the binary system of BiFeO₃-BaTiO₃ ceramics exhibits similar giant-dielectric-like behavior as observed in the pure BiFeO₃ ceramics.

Acknowledgment

This work was financially supported by the Industry/University Cooperative Research Center (I/UCRC) in HDD Component, the Faculty of Engineering, Khon Kaen University and National Electronics and Computer Technology Center, National Science and Technology Development Agency (NSTDA). The author (S.C.) is also thankful to the Young Scientist and Technologist Program (YSTP) for the undergraduate scholarship and the Synchrotron Light Research Institute (Public Organization) for PhD scholarship and Suranaree University of Technology for additional support.

References

1. W. Eerenstein, N. D. Mathur, and J. F. Scott, Multiferroic and magnetoelectric materials. *Nature* **442**(7104), 759–765 (2006).
2. S. V. Kiselev, R. P. Ozarov, and G. S. Zhdanov, Detection of magnetic order in ferroelectric BiFeO₃ by neutron diffraction. *Sov. Phys. Dokl.* **7**, 742 (1962).
3. P. Fishetr, M. Polomska, S. Sosnowska, and M. Szymanski, Temperature dependence of the crystal and magnetic structures of BiFeO₃. *J. Phys. C* **13**, 1931–1940 (1980).
4. F. Kubel and H. Schmid, Structure of a ferroelectric and ferroelastic monodomain crystal of the perovskite BiFeO₃. *Acta Crystallogr. Sect. B* **46**, 698–702 (1990).
5. J. R. Teague, R. Gerson, and W. J. James, Dielectric hysteresis in single crystal BiFeO₃. *Solid State Commun.* **8**, 1073–1074 (1970).
6. A. J. Moulson and J. M. Herbert, *Electroceramics*, 2nd edn. New York: John Wiley; 2003.
7. K. Uchino, *Ferroelectric Devices*. New York: Marcel Dekker; 2000.
8. M. M. Kumar, A. Srinivas, and S. V. Suryanarayana, Structure property relations in BiFeO₃/BaTiO₃ solid solutions. *J. Appl. Phys.* **7**, 855 (2000).
9. K. Ueda, H. Tabata, and T. Kawai, Coexistence of ferroelectricity and ferromagnetism in BiFeO₃-BaTiO₃ thin films at room temperature. *Appl. Phys. Lett.* **75**, 555 (1999).

10. S. Chandarak, M. Unruan, T. Sareein, A. Ngamjarrojana, S. Maensiri, P. Laoratanakul, S. Ananta, and R. Yimnirun, Fabrication and characterization of $(1-x)\text{BiFeO}_3-x\text{BaTiO}_3$ ceramics prepared by a solid state reaction method. *J. of Magnetism* **14**(3), 120–123 (2009).
11. S. Chandarak, T. Sareein, A. Ngamjarrojana, S. Maensiri, P. Laoratanakul, S. Ananta, and R. Yimnirun, Effect of calcination conditions on phase formation and characterization of $\text{BiFeO}_3\text{-BaTiO}_3$ powders synthesized by a solid-state reaction. *Adv. Mater. Res.* **55–57**, 241–244 (2008).
12. S. Hunpratub, P. Thongbai, T. Yamwong, R. Yimnirun, and S. Maensiri, Dielectric relaxations and dielectric response in multiferroic BiFeO_3 ceramics. *Appl. Phys. Lett.* **94**, 062904-1-3 (2009).
13. M. Maglione and M. A. Subramanian, Dielectric and polarization experiments in high loss dielectrics: A word of caution. *Appl. Phys. Lett.* **93**, 032902-1-3 (2008).
14. R. Waser and R. Hagenbeck, Grain boundaries in dielectric and mixed-conducting ceramics. *Acta Mater.* **48**, 797–825 (2000).
15. Y. H. Lin, M. Li, C. W. Nan, J. Li, J. Wu, and J. He, Grain and grain boundary effects in high-permittivity dielectric NiO-based ceramics. *Appl. Phys. Lett.* **89**, 032907-1-3 (2006).
16. P. Thongbai, C. Masingboon, S. Maensiri, T. Yamwong, S. Wongsanmai, and R. Yimnirun, Giant dielectric behaviour of $\text{CaCu}_3\text{Ti}_4\text{O}_{12}$ subjected to post-sintering annealing and uniaxial stress. *J. Phys.: Condens. Matter.* **19**, 236208-1-10 (2007).
17. S. Maensiri, P. Thongbai, and Y. Yamwong, Giant dielectric permittivity observed in $\text{CaCu}_3\text{Ti}_4\text{O}_{12}/(\text{Li},\text{Ti})$ -doped NiO composites. *Appl. Phys. Lett.* **90**, 202908-1-3 (2007).
18. C. Masingboon, S. Maensiri, T. Yamwong, P. L. Anderson, and S. Seraphin, Nanocrystalline $\text{CaCu}_3\text{Ti}_4\text{O}_{12}$ powders prepared by egg white solution route: synthesis, characterization and its giant dielectric properties. *Appl. Phys. A* **91**, 87–95 (2008).
19. C. Masingboon, P. Thongbai, S. Maensiri, T. Yamwong, and S. Seraphin, Synthesis and giant dielectric behavior of $\text{CaCu}_3\text{Ti}_4\text{O}_{12}$ ceramics prepared by polymerized complex method. *Mater. Chem. Phys.* **109**, 262–270 (2008).
20. D. C. Sinclair, T. B. Adams, F. D. Morrison, and A. R. West, $\text{CaCu}_3\text{Ti}_4\text{O}_{12}$: One-step internal barrier layer capacitor. *Appl. Phys. Lett.* **80**, 2153-1-3 (2002).
21. M. C. Ferrarelli, T. B. Adams, A. Feteira, D. C. Sinclair, and A. R. West, High intrinsic permittivity in $\text{Na}_{1/2}\text{Bi}_{1/2}\text{Cu}_3\text{Ti}_4\text{O}_{12}$. *Appl. Phys. Lett.* **89**, 212904-1-3 (2006).

BIOGRAPHY

Ms. Sujittra Chandarak was born on July 28, 1986 in Lampang province, Thailand. She received her Bachelor's Degree in Science (Materials Science) from Chiang Mai University in 2008. After graduation, she continued her Doctoral Degree in School of Ceramic Engineering, Institute of Engineering, Suranaree University of Technology. She has published several articles in international journals. Her publications are listed in Appendix B.

